Technical University of Denmark

DTU

Some nonlinear effects on the flutter speed and blade stability

Hansen, Morten Hartvig; Kallesøe, Bjarne Skovmose

Published in:
Research in aeroelasticity EFP-2007

Publication date:
2008

Document Version
Publisher's PDF, also known as Version of record

Link back to DTU Orbit

Citation (APA):
Hansen, M. H., & Kallesøe, B. S. (2008). Some nonlinear effects on the flutter speed and blade stability. In C. Bak (Ed.), Research in aeroelasticity EFP-2007 (Vol. Risø-R-1649(EN), pp. 93-105). Roskilde: Danmarks Tekniske Universitet, Risø Nationallaboratoriet for Bæredygtig Energi. (Denmark. Forskningscenter Risoe. Risoe-R; No. 1649(EN)).

DTU Library
Technical Information Center of Denmark

Research in Aeroelasticity EFP-2007

Edited by Christian Bak

Risø–R–1649(EN)
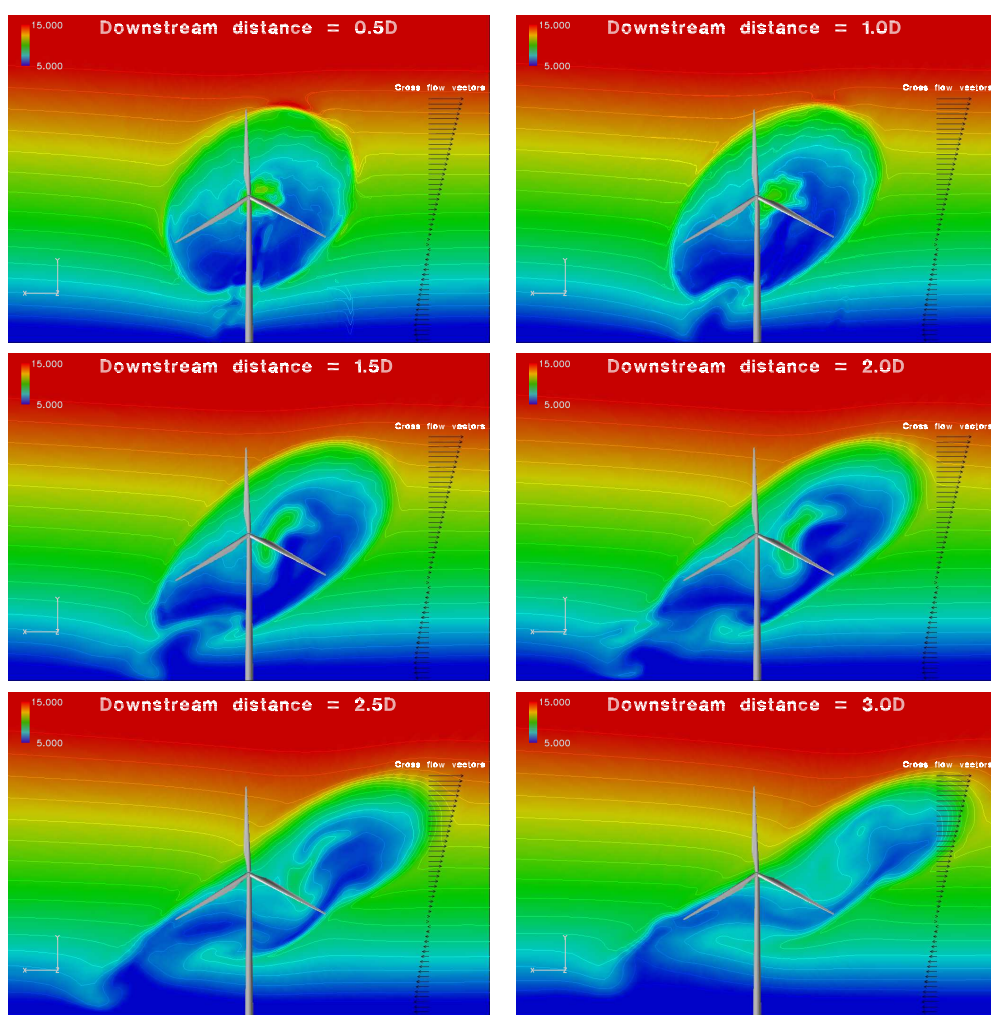
Abstract:

This report contains results from the EFP2007 project "Program for Research in Applied Aeroelasticity". The main results from this project are:

- The rotor aerodynamics were computed using different types of models with focus on the flow around the tip. The results showed similar trend for all models.

- Comparison of 3D CFD computations with and without inflow shear showed that the integrated rotor thrust and power were largely identical in the two situations.

- The influence of tower shadow with and without inflow shear showed significant differences compared to BEM computations, which gives cause for further investigation.

- 3D CFD computations showed that the flow in the region of the nacelle anemometer measured the flow angle in the wake with errors up to as much as $7°$ relative to the freestream flow angle.

- As long as the flow over a blade remains attached there is little difference between 2-D and 3-D flow. However, at separation an increased lift is observed close to the rotational axis.

- A correlation based transition model has been implemented in the incompressible EllipSys2D/3D Navier-Stokes solver. Computations on airfoils and rotors showed good agreement and distinct improvement in the drag predictions compared to using fully turbulent computations.

- Comparing the method of Dynamic Wake Meandering (DWM) and IEC, the IEC model seems conservative regarding fatigue and extreme loads for the yaw, driving torque and flapwise bending, whereas the loads on tower and blade torsion are non-conservative.

- An experimental method for measuring transition point and energy spectra in airfoil boundary layers using microphones has been developed.

- A robust and automatic method for detecting transition based on microphone measurement on airfoil surfaces has been developed.

- Transition points and the corresponding instabilities have clearly been observed in airfoil boundary layers.

- Predictions of the transition points on airfoils using the e^n method were in good agreement with measurements.

- The Risø-DTU airfoil design methodology was verified and showed that airfoils can be designed with very high lift-drag ratio, insensitivity of $c_{l,max}$ to leading edge roughness and differences in turbulence intensity, relatively high stiffness and high compatibility.

Contents

Preface

The Energy Research Project "Program for Research in Applied Aeroelasticity, EFP-2007" was carried out in cooperation between the two institutes at Technical University of Denmark (DTU), Risø National Laboratory of Sustainable Energy (Risø DTU) and the Department of Mechanical Engineering (DTU MEK), from 1 April 2007 to 31 March 2008. From the onset of the project, six milestones were defined which represent the main part of the research activity. Apart from the work focused on the milestones, also analyzes of current problems and further development of the existing models were carried out.

Several researchers at DTU MEK and Risø DTU have been involved in the project work and have contributed to the research presented in this report. To enable reference to the different parts of the report, the names of the authors are indicated for each chapter. It should, however, be emphasized that the report is not a detailed report of the complete activity within the project. Thus, not all of the contributors to the project appear as authors to the different chapters. For a detailed description of the results from the project, please see Chapter 9 in which a complete list of publications in the project can be found.

At the DTU MEK, the following researchers from the Fluid Mechanics Section of the Department of Mechanical Engineering have been involved in the project:

Kurt S. Hansen
Martin O.L. Hansen
Gabriel Hernandez
Robert Mikkelsen
Wen Zhong Shen
Jens Nørkr Sørensen
Niels Troldborg
Stig Øye

At Risø DTU, primarily the researchers from the Aeroelastic Design Group have contributed to the project:

Peter B. Andersen
Christian Bak
Andreas Bechmann
Franck Bertagnolio
Thomas Buhl
Mads Døssing
Mac Gaunaa
Anders M. Hansen
Morten H. Hansen
Jeppe Johansen
Bjarne S. Kallesøe
Gunner C. Larsen
Torben J. Larsen
Helge A. Madsen
Helen Markau
Flemming Rasmussen
Niels N. Sørensen
Frederik Zahle

1 Summary

This report contains the results from the Energy Research Project "Program for Research in Applied Aeroelasticity, EFP-2007" covering the period from 1. April 2007 to 31. March 2008. The partners in the project are the two institutes at Technical University of Denmark (DTU), Risø National Laboratory of Sustainable Energy (Risø DTU) and the Department of Mechanical Engineering (DTU MEK). The overall objectives of the project are to ensure the development of an aeroelastic design complex, which can create the basis for the next generation of wind turbines and make new design concepts possible. The project forms a strategic cooperation between Risø DTU and DTU MEK and the wind turbine industry with emphasis on obtaining a suitable balance between long-term strategic research, applied research and technological development. To obtain synergy between the different subjects and to ensure an optimal, dynamic cooperation with the industry, while maintaining the continuity of the research, the project is organized as a research program within applied aeroelasticity with a combination of research activities with specific short-term targets within one year and general continuous long-term research activities. This research project has been the tenth in a row of one-year projects, which has ensured a continuous development since 1997, where the activity in this row of projects is described in [1], [2], [3], [4], [5], [6], [7], [8] and [9].

1.1 Main results from the project

The main emphasis of the activity in the project was put on the milestones which were defined in the project proposal. Furthermore, there has been activity on the further development of tools and models in "the aeroelastic design complex" which consists of 3D Navier-Stokes models, aeroacoustic models, airfoil- and blade design, aeroelastic codes and loads, aeroelastic stability, control and new concepts. Also, there have been investigations of subjects of fundamental character, which often constitute long-term research. A summary of the main results for each milestone from the project is given in the following.

1.1.1 Validation and further development of aerodynamic induction modeling

The distribution of axial induction near the tip of a Betz optimal loaded actuator disc has been investigated using five different computational tools. The loading is in itself singular at the edge of the actuator disc and the corresponding computed inductions shows comparable behavior near the tip. All the considered methods captures the trend in increased induction towards the tip, and slightly lower induction inboard resulting in averaged level for the whole disc close to axial momentum theory, $a=1/3$. The streamfunction-vorticity model and the distributed vortex sheet model compare very closely to each other for the Betz optimal loading. Loadings with a more smooth transition to zero at the tip, reduced the observed peak for the constant loading considerably although the inboard induction remains virtually unaffected.

The tip part of wind turbine rotors were investigated e.g. to compare different computational methods.

1.1.2 Modeling of flow interaction between rotor, tower and nacelle

In the work package "Modeling of flow interaction between rotor, tower and nacelle" a number of CFD simulations have been carried out on the Siemens 3.6MW wind turbine for various flow situations. The influence of shear on the rotor loads was investigated, and it was found that the azimuthal variation of the load gave rise to some hysteresis in the axial and tangential forces. The integrated rotor thrust and power were largely identical to simulations carried out with uniform inflow. The influence of tower shadow has been investigated for two flow cases, one with and another without inflow shear. Generally, the CFD results predicted the tower shadow by as much as 50% different compared to BEM computations, which gives cause for further investigation. Even though the nacelle was not included in the simulations the flow in the

3D CFD computations were carried out to investigate shear, tower shadow and nacelle flow

region of the nacelle anemometer was investigated, and it was found that the measured flow angle in the wake differed by as much as $7°$ relative to the freestream flow angle. As such, for the flow case where the turbine operated in $10°$ yaw error, the flow angle in the wake of the turbine measured on average $0°$, giving a possible explanation to the apparently consistent yaw error observed in the Høvsøre experiment. Investigation of the wake development downstream of a turbine operating in shear inflow showed that a rotation in the wake gave rise to significant mixing of the low velocity flow from the bottom half of the wake into the top half. Additionally, for the flow with large wind direction changes with height, the wake was largely dissolved only three diameters downstream of the turbine.

1.1.3 Mapping of 3D effects and modeling of laminar-turbulent transition in boundary layers on rotating blades

As long as the flow remains attached there is little difference between 2-D and 3-D flow

A series of computations were made using the commercial CFD code FLUENT on a rotating blade in order to investigate 3-D effects originating mainly from Coriolis and centrifugal forces. The blade was confined between two concentric cylinders, where a slip boundary condition was applied that allowed a tangential velocity but no normal velocity. This is basically a wall boundary condition for an inviscid flow. Further, the inlet boundary condition was specified so that the geometrical angle of attack was the same along the entire blade. The main conclusion is that as long as the flow remains attached there is little difference between 2-D and 3-D flow. However, at separation an increased lift is observed close to the rotational axis. For a ratio between radius and chord, r/c, of 3.2 the computed lift coefficient as a function of the angle attack is compared to a 2-D calculation and the same 2-D data corrected for 3-D effects using empirical models. It appears that for this position the 3-D correction underestimates the 3-D effects. The work is still in progress, however a tool has been developed that can be used to investigate some of the assumptions made in quasi 3-D codes and to compare and tune existing stall delay models.

CFD computations using a new transition model show good agreement and distinct improvement in the drag predictions compared to fully turbulent computations

Apart from investigating the 3D effects also modeling of laminar-turbulent transition in boundary layers on rotating blades has been investigated. A correlation based transition model has been implemented in the incompressible EllipSys2D/3D Navier-Stokes solver. Based on a series of zero pressure gradient flat plate boundary layers, expressions for the two missing correlation functions have been determined. Next, the model has been used to predict the lift and drag for two wind turbine airfoils, the S809 and NACA63-415 respectively. Both computations show good agreement and distinct improvement in the drag predictions compared to using fully turbulent computations. The model was used to successfully predict transition on a 6:1 prolate spheroid at zero degrees incidence for four different Reynolds numbers, while the model due to lack of cross-flow by-pass transition capability was not able to predict the correct location of transition for the spheroid at 30 degrees incidence. The model was finally applied to the well known NREL Phase-VI rotor, corresponding the the upwind cases from the original blind comparison. It was shown how the transition model, through variation of the intensity of the inflow turbulence could improve the prediction around stall, while the low wind speed and high wind speed regions were nearly unaffected by the transition model. Generally, one must expect that the transition process can be very important for predicting the correct aerodynamics of rotors depending on rotor design and airfoil shape, and that the present model can be a valuable tool.

1.1.4 Modeling and optimization of structural couplings in aeroelastic computations

A VABS model has been developed for implementation in the aeroelastic code HAWC2

The work made under this milestone is not reported this year, but the work is continued in the new EFP-2007-II project. During the project, the necessary building blocks have been collected in order to implement the anisotropic beam element, VABS, into the aeroelastic code, HAWC2, and the actual implementation should now be straight forward. Further, emphasis have been put on understanding how the structural behaviour of the blades should be changed in order to

improve the aeroelastic response of the wind turbine. When those two tasks have been finalised, conclusions will be made and reported as part of the EFP-2007-II project.

1.1.5 Comparisons of design methods for wind turbines in wake

A new implementation of the Dynamic Wake Meandering (DWM) model has been demonstrated, where all wake sources from the neighboring turbines are included. Production cases have only been considered and ambient turbulence corresponding to a terrain class IC (high wind, low turbulence) has been applied. A comparison of loads between turbines with a row distance of 3 and 8 diameters (3D and 8D), respectively has been investigated with the DWM model and the method according to the IEC 61400-1 ed 3. standard. The simulations performed for very low wind speeds (<8m/s) were however excluded in the analysis due to convergence problems when negative wind speed occurred on the downstream rotor, which is considered to be of minor importance to the results.

When comparing the loads between the 3D and 8D configuration, the turbine at the 3D configuration never experiences any free flow situation. Another interesting observation is that the tower loads seem more affected at longer downstream positions than when turbines are close to each other. This effect is addressed to the meandering effect causing higher states of full, half and no wake situation when the meandering has had time to develop.

In the direct comparison between the DWM and the IEC model for the 3D case, the IEC model seems conservative regarding fatigue and extreme loads for the yaw, driving torque and flapwise bending, whereas the loads on tower and blade torsion are non-conservative. The maximum tower bending is 20% higher for the DWM model and 55% higher for the blade torsion moment.

Comparing DWM and IEC, the IEC model seems conservative regarding fatigue and extreme loads for the yaw, driving torque and flapwise bending, whereas the loads on tower and blade torsion are non-conservative.

For the 8D case, the comparison shows a generally good agreement between the two models regarding yaw, driving torque and flapwise blade bending with deviances in the order of 10%. However, for the tower loads and blade torsion a significantly higher load level is seen with the DWM model. Regarding tower loads the fatigue level is 25% higher with the DWM model and the maximum bending moment is 60% higher than for the IEC model. A similar difference is also seen for the blade torsion.

1.1.6 Aero-servo-elastic pitch dynamics for blades with large deflections

The modal dynamic of a beam with a large static deflection are analyzed with three different structural beam models. The coupling between bending and torsion, caused by the deflection and predicted by the three different models are seen to agree qualitatively, except of the edgewise bending component in the torsional mode.

The effects of large bending deflections under steady state operation of the wind turbine blade on its stability limits, especially with regards to the flutter limit, are analyzed. The investigation shows no significant change of the flutter limit on the rotor speed due to the blade deflection, whereas the first edgewise bending mode becomes negatively damped due to the coupling with blade torsion which causes a change of the effective direction of blade vibration. These observations are confirmed by nonlinear aeroelastic simulations using HAWC2.

Assuming large deflections shows no significant change of the flutter limit on the rotor speed, whereas the first edgewise bending mode becomes negatively damped due to the coupling with blade torsion.

Next, the effect of a free-play in the pitch system is analyzed. A linear pitch bearing stiffness with a free-play is imposed on a 2D wing-section model. The pitch system model and the wing-section model are combined and simulated in time to determine the relative inflow speed where flutter onsets. It is found that this flutter speed decrease when a free-play is introduced.

The flutter speed decreases when a free-play in the pitch bearing is introduced.

1.1.7 Wind tunnel tests of new airfoil series

Three airfoils
were tested and
microphones
were surface
mounted and
measured transition.

Three airfoils were tested in the LM Glasfiber wind tunnel to investigate 1) transition from laminar to turbulent flow in the airfoil boundary layer, 2) the Risø DTU airfoil design methodology and 3) the inflow characteristics at small turbulent length scales and the influence on airfoil performance. A technique using surface mounted microphones were developed and used where frequencies between 30Hz and 20kHz were measured. Together with the microphones the airfoil models had pressure taps to measure the aerodynamic characteristics in terms of the pressure distributions that were integrated to lift, drag and moment. Also, the drag was measured using a wake rake. To investigate the influence of inflow turbulence on airfoil performance two different grids were mounted upstream of the airfoil.

A large amount of microphone data has been processed with reference to transition detection and selected results are presented. All results show expected values and the method for transition detection is well established. The only drawback in the method is uncertainty with respect to the accuracy of the detected values near the leading edge. In all cases transition is clearly observed and also the onset of instability as well as the distance over which transition develops.

The Risø-C2-18
airfoil was tested
and showed to
be in agreement
with the design
objectives which
were e.g. high
maximum lift,
high lift-drag
ratio and a high
degree of roughness insensitivity

The design of the Risø-C2-18 airfoil was verified in the wind tunnel and showed that the design criteria were fulfilled. Thus, the airfoil with clean surface showed the characteristics as predicted with the flow simulation tools, however with a slightly lower maximum lift. For example the fast movement of the transition point at around $c_l = 1.7$ showed to be predicted well by the e^n model in the flow simulation tool XFOIL. Also, an unavoidable but acceptable loss in maximum lift was seen which was at its highest up to $\Delta c_l = 0.15$. Furthermore, it was as expected seen that the drag was not resistant to leading edge roughness and an increase in both maximum lift and drag were seen. Testing the airfoils with different turbulence intensity showed an increase in drag and an increase in maximum lift compared to the tests at lower turbulence intensity.

References

[1] H.A. (Ed.) Madsen. Forskning i aeroelasticitet. rapport for efp-97 (in danish). Risø-r-1066(da), Risø National Laboratory for Sustainable Energy, August 1998.

[2] H.A. (Ed.) Madsen. Forskning i aeroelasticitet - efp-98 (in danish). Risø-r-1129(da), Risø National Laboratory for Sustainable Energy, August 1999.

[3] H.A. (Ed.) Madsen. Forskning i aeroelasticitet - efp-99 (in danish). Risø-r-1196(da), Risø National Laboratory for Sustainable Energy, November 2000.

[4] H.A. (Ed.) Madsen. Forskning i aeroelasticitet - efp-2000 (in danish). Risø-r-1272(da), Risø National Laboratory for Sustainable Energy, July 2001.

[5] H.A. (Ed.) Madsen. Forskning i aeroelasticitet efp-2001 (in danish). Risø-r-1349(da), Risø National Laboratory for Sustainable Energy, December 2002.

[6] C. (Ed.) Bak. Forskning i aeroelasticitet efp-2002 (in danish). Risø-r-1434(da), Risø National Laboratory for Sustainable Energy, Februar 2004.

[7] C. (Ed.) Bak. Forskning i aeroelasticitet efp-2004 (in danish). Risø-r-1509(da), Risø National Laboratory for Sustainable Energy, May 2005.

[8] C. (Ed.) Bak. Research in aeroelasticity efp-2005. Risø-r-1559(da), Risø National Laboratory for Sustainable Energy, May 2006.

[9] C. (Ed.) Bak. Research in aeroelasticity efp-2006. Risø-r-1611(da), Risø National Laboratory for Sustainable Energy, July 2007.

2 Analysis of induction near tip

Author: Robert Mikkelsen, Helge A. Madsen, Martin Hansen, Wen Z. Shen, Stig Øye

This section seeks to analyze the behavior of the induction near the tip of a Betz optimal loaded actuator disc. Several axi-symmetric methods are applied in analyzing the variation of the axially induced velocities towards the edge of the actuator disc. The purpose of the analysis is to quantify the difference between models and compare to simple axial momentum theory, which forms the foundation of BEM methods.

2.1 Rotor aerodynamic modeling

Accurate prediction of the induced velocities along the turbine blades, is a key factor in approaching optimally aerodynamically loaded turbines. Both for extracting the maximum energy of the incoming wind and in general to be able to perform accurate predictions of turbine performance. Aerodynamic modeling using BEM-methods assumes radially independency of the annular stream tubes passing through the turbine rotor. Thus, assuming a loading of constant level results in a corresponding constant level of induction. However, due to the expanding streamlines near the rotor the axial induction increases towards the tip region whereas near the root section the higher swirl component in the wake tends to reduce the axial component of induction, see [1]. These effects may be investigated with more advanced aerodynamic models like CFD or vortex models. In order to limit the investigation, the present work is focused on the detailed behavior of the flow field around an axi-symmetric actuator disc loaded with constant normal loading at Betz optimal condition, C_T=0.89. The study is aimed at describing and quantifying these effects which could lead to simple corrections for improving BEM methods. In order to broaden the picture of the investigation, the capabilities of five different tools presently in use for research, are presented in the following with the aim of comparing the features of the Betz optimally loaded actuator disc. The methods are:

Five different tools have been used for comparison of the predicted rotor aerodynamics.

- Streamfunction-Vorticity, (CFD type)
- EllipSys2D Axi-symmetric, (CFD type)
- FIDAP, (CFD type)
- Vortex sheet, Inviscid, (singular element type)
- Vortex lines, 3D inviscid (singular element type)

A short description of the listed methods are given in the following.

2.1.1 CFD modeling of the wake

The three considered CFD models solve the axi-symmetric Navier-Stokes equations in the meridional plane by inserting an actuator disc represented by a line. The computational grids are in all cases simple rectangular/Cartesian type grid with most computational cells concentrated around the disc, with cells stretching towards the far field boundaries. The three methods handles the solution of the problem in hand differently, but from a mathematically point of view there should be a unique solution to this problem, however, in the numerically representation deviations are unavoidable. With the Streamfunction-Vorticity formulation [2] [3] mass conservation is ensured identically whereas EllipSys2D and FIDAP are based on primitive variables. The EllipSys2D was extended by W. Shen to cope with axi-symmetry conditions and FIDAP is a commercial software package. The present investigation seeks to make an inviscid analysis of the problem, however, due to numerical diffusion and in order to stabilize the solution process,

viscous diffusion is added. An effective Reynolds number Re=RV/ν of 10.000-50.000 ensures almost independent solution of the viscosity.

2.1.2 Vortex sheet modeling of the wake

A distribution of vortex rings is used to form a vortex sheet of the wake, shed from the actuator disc, elegantly solving the inviscid flow field around a constant loaded actuator disc, see Øye[4]. Figure 1 depicts a sketch of a single ring vortex element and the vortex sheet modeled by a distribution of vortex rings. An analytical inviscid solution to the single vortex ring element
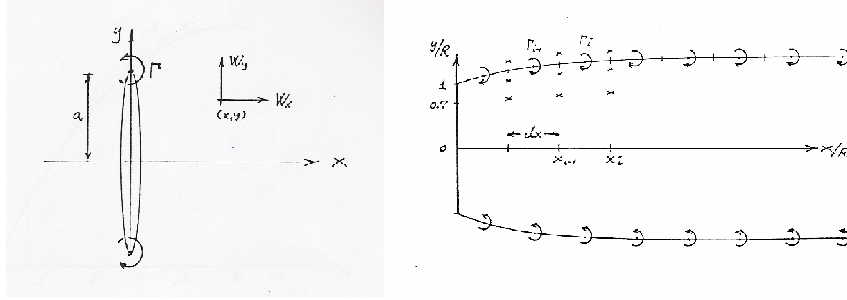

Figure 1. Vortex ring element (left) and an actuator disc wake of distributed of vortex ring elements (right).

exists, where the induced velocities (W_x, W_y) are given by

$$W_x = \frac{\Gamma}{2\pi} \frac{1}{\sqrt{x^2 + (y+a)^2}} \left(\frac{a^2 - x^2 - y^2}{x^2 + (y-a)^2} E(k) + K(k) \right) \tag{1}$$

$$W_y = \frac{\Gamma}{2\pi} \frac{x}{y\sqrt{x^2 + (y+a)^2}} \left(\frac{a^2 + x^2 + y^2}{x^2 + (y-a)^2} E(k) - K(k) \right) \tag{2}$$

and where $E(k)$ and $K(k)$ are given by the elliptic integrals

$$k = \sqrt{\frac{4ay}{x^2 + (y+a)^2}}, \quad y \geq 0 \tag{3}$$

$$E(k) = \int_0^{\frac{\pi}{2}} \frac{d\theta}{\sqrt{1 - k^2 \sin^2 \theta}}, \quad K(k) = \int_0^{\frac{\pi}{2}} \sqrt{1 - k^2 \sin^2 \theta} d\theta \tag{4}$$

Thus, the wake is discritisized by a distribution of ring vortex elements where the strength Γ_i of each element depends on the thrust C_T as

$$\gamma_i = C_T \frac{U^2}{2V_{a,i}}, \quad \Gamma_i = (\gamma_{i-1} + \gamma_i) dx, \quad V_{a,i} = U + \frac{1}{2} \left(W_x^{r+dr} + W_x^{r-dr} \right), \quad dr \simeq 0.1R \tag{5}$$

and the expansion of the wake is given by

$$r_i = R\sqrt{\frac{V_{r=0.7R}^{x=0}}{V_{r=0.7r_i}^{x_i}}} \quad or \quad r_i = R\sqrt{\frac{\overline{V}^{x=0}}{\overline{V}^{x_i}}} \tag{6}$$

where the first term is an approximation or a best guess of a representative velocity ensuring mass conservation at all axial section. The correct way to compute the expansion involves computing the average velocity given by the second term, however, this is far more time consuming in the iterative solution process of relaxing the wake. Numerically, the wake length L is resolved by elements about 10-20R downstream. A far wake correction given by

$$W_x^{farwake} = \left(1 + \frac{L/r}{\sqrt{1 + L/r}} \right) \frac{\gamma_n}{2} \tag{7}$$

ensures that the wake stretches to infinity.

2.1.3 Vortex line modeling

Using vortex lines elements, the trailing vortices from the turbine blades are resolved by vortex elements either as a prescribed wake or as a free wake, the later being far more computational demanding. A prescribed wake modeling is used in the following for resolving the trailed tip and root vortices and the bound blade vortices of the three turbine blades. It should be noted that the wake is relaxed as with the ring vortex method, thus, the expansion is a part of the solution. Figure 2 outlines the wake geometry. Computing induced velocities is based on the
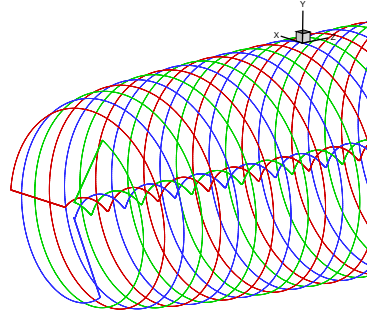

Figure 2. Vortex line representation of three blades turbine wake. The expansion of the prescribed wake is based on a representative azimuthal average velocity at $r = 0.7r_i$ and the lines are loaded to C_T =0.89. Tip speed ratios $\lambda = 3, 6, 9$ are analyzed.

Biot-Savart law given by

$$\mathbf{W} = \frac{\Gamma}{4\pi} \oint \frac{d\mathbf{s} \times \mathbf{r}}{|\mathbf{r}|^3} \tag{8}$$

where the strength approximately may be computed as

$$\Gamma = C_T \pi R U (1-a)/\lambda, \quad \lambda = R\Omega/U \tag{9}$$

with a representing the axial interference factor. Some deviation is to be expected since, as compared to the other models, this is a genuine 3D approach.

2.2 Changed induction towards the tip

Figure 3 depicts the computed flow field represented by streamlines in the axi-symmetric plane around an actuator disc, C_T =0.89 using the streamfunction vorticity method. Near the edge of the actuator disc the streamlines are curved or bend resulting in changed induction compared to the inboard region. The behavior of this effect is captured by all the considered methods. The axial induction on non-dimensional form referred to as axial interference a, is displayed in figure 4. The well known result from axial momentum theory predicts a value of a=1/3 for this loading, which compares well with average values for the depicted distribution i.e. the slightly lower inboard level is compensated for by the higher level outboard. The computed level agree inboard nicely within few percents, but in the tip region deviation are larger. All methods predict significant increased axial interference in the tip region with max levels around 0.4, although FIDAP predicts a somewhat higher maximum value. The close up shown outboard comparing streamfunction-vorticity with vortex rings modeling reveal a spot on comparison for this case showing that two very different methods computes nearly the exact same distribution of induced velocities. The values inserted near the tip, refer to the numerical resolution of the disc i.e. 160 equidistant cells for the streamfunction-vorticity computations and 80 points using the ring vortex method to compute the average velocity across each axial plane. Looking at the radial velocity component in figure 5, the velocity increases gradually from the root to a peak value around V_r/V_o=0.4-0.6 at the tip. The comparison with EllipSys2D is generally good and only at the very tip significant difference are apparent. The singular behavior inherent in the solutions at the tip for the constant loading, appear more clear for the radial velocity

The predicted induced velocities compared well between the different models on the inner part of the rotor, but close to the tip the deviations between the models are large.
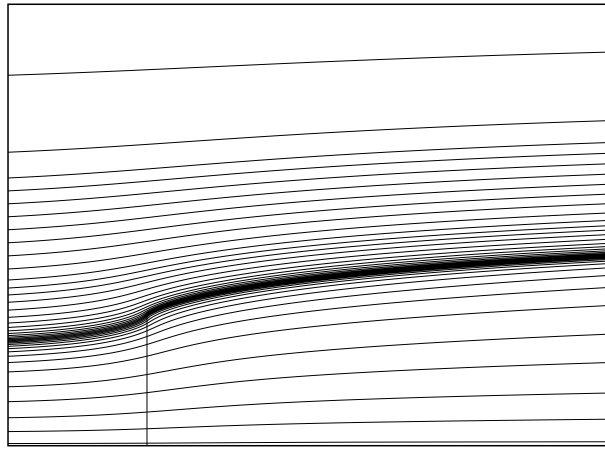
Figure 3. Axi-symmetric view of expanding streamlines through and around a constant loaded actuator disc, C_T =0.89. The symmetry line is at the bottom.
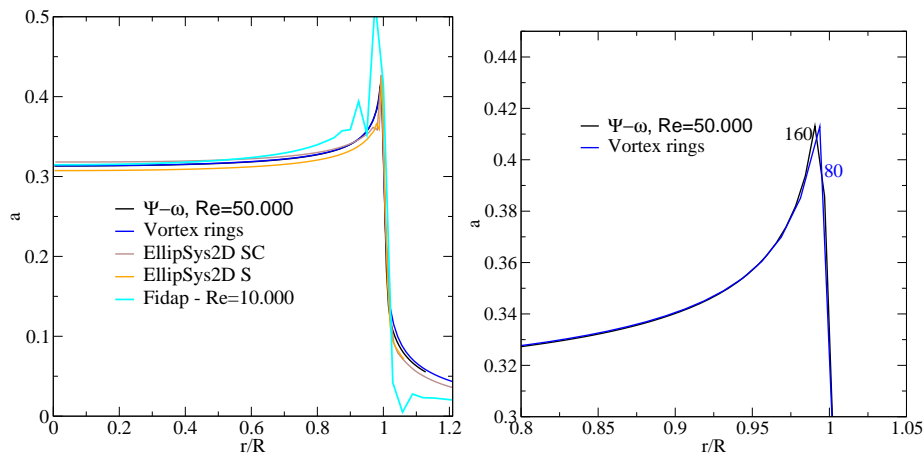
Figure 4. Axial interference computed with Streamfunction-Vorticity, EllipSys2D using the SIM-PLE and SIMPLE-C coupling, FIDAP and the ring vortex model.
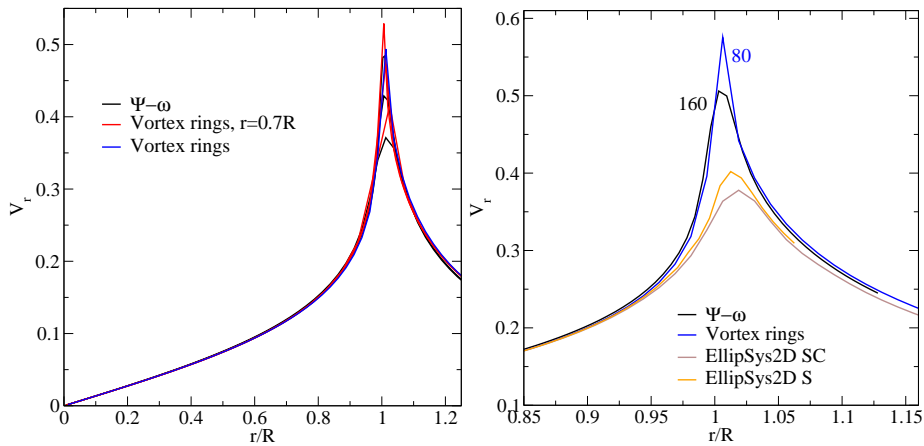
Figure 5. Radially induced velocity due to expansion of the streamlines.

although the same behavior is present for the axial interference. The expansion of the wake is presented in figure 6 showing the limiting streamline passing through the edge of the disc. The predictions at an axial position of 10R downstream vary roughly between 1.33-1.38R. The
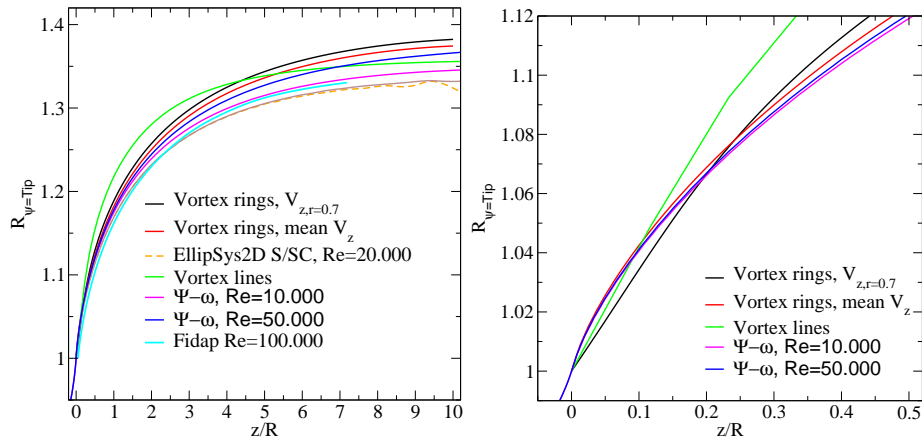
Figure 6. Wake expansion, limiting streamline through edge of actuator disc.

trend among the different computation appears to be the same apart from the vortex line model, which follow a different path with a higher rate near the disc, leveling off comparable to the other methods. A difference in behavior was expected as noted previously regarding the vortex line model compared to the other models. The comparison of the expansion rate in itself should be considered of limited importance, as an actual turbine wake generally not will be preserved as long as 10R downstream. It is although, a good indicator in a code to code comparison. Figure 7 presents the expansion and axial interference computed with the vortex line method. The trend is comparable to the actuator disc results with an increased induction towards the
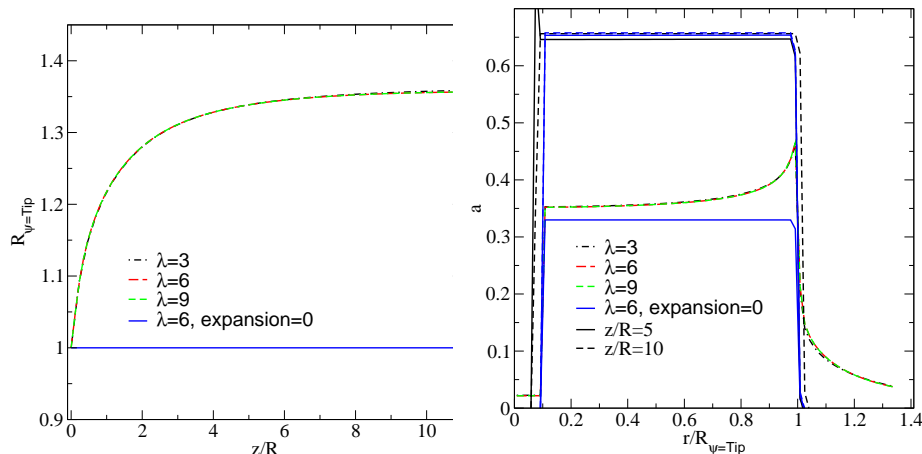
Figure 7. Vortex line modeling of the wake. Expansion (left) and axial interference at the disc and in the wake (right).

tip, however, the averaged level at the rotor plane is around a=0.36 or 10% above 1/3, although in the far wake levels at z=10R downstream, settles close to a=2/3 in good accordance with axial momentum theory. In the view of the idealized optimal loading of Betz, one should keep in mind that actual loadings do not have the singular type behavior, but tend to have a more or less smooth transition to a zero loading near the tip. The effect of increased induction may, however, still be present when applying a smooth de-loading at the tip. Figure 8 presents an artificial type loading which decreases smoothly towards zero using a simple polynomial. The two considered loadings compared to the Betz optimum, clearly reduces the induction at the tip, however, inboard the induction appears unaffected.

Inspecting the expansion of the wake is a good indicator in a code to code comparison of the predicted flow fields.

Figure 8. Effects of smooth load reduction towards the tip (left) and corresponding induction near the tip (right).

2.3 Summary

All the considered methods for prediction of rotor aerodynamics captures the trend in increased induction towards the tip, and slightly lower induction inboard.

The distribution of axial induction near the tip of a Betz optimal loaded actuator disc has been investigated using five different computational tools. The loading is in itself singular at the edge of the actuator disc and the corresponding compute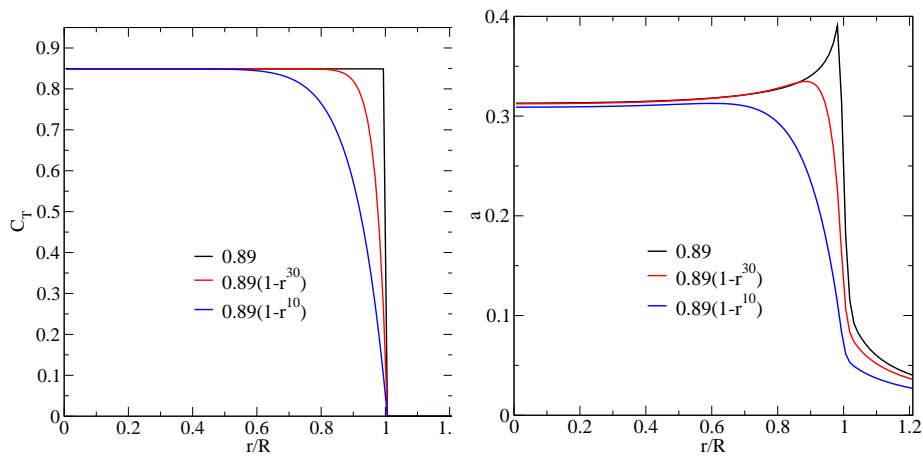d inductions shows comparable behavior near the tip. All the considered methods captures the trend in increased induction towards the tip, and slightly lower induction inboard resulting in averaged level for the whole disc close to axial momentum theory, $a=1/3$. The streamfunction-vorticity model and the distributed vortex sheet model compare very closely to each other for the Betz optimal loading. Considering the loadings with a more smooth transition to zero at the tip, reduced the observed peak for the constant loading considerably although the inboard induction remains virtually unaffected.

References

[1] Øye S. Bak C. Johansen J. Madsen H.A., Mikkelsen R. A detailed investigation of the blade element momentum (bem) model based on analytical and numerical results and proposal for modification of the bem model. *Proc. of the 2ed. Conf. on "The science of making torque from wind"*, 75, 2007.

[2] Shen W.Z. Mikkelsen R., Sørensen J.N. Modelling and analysis of the flow field around coned rotors. *Wind Energy*, 4:121–135, 2001.

[3] Mikkelsen R. *Actuator disc methods applied to wind turbines*. PhD thesis, Tech. Univ. of Denmark, Dept. Mech. Eng. Fluid Mechanics section, Nov 2003.

[4] Øye S. A simple vortex model. *Proc. of the 3ed IEA Symposium on the Aerodynamics of Wind Turbines, Harwell Laboratory, McAnulty KF(ed.), ETSU, UK*, 1990.

3 The Influence of Wind Shear and Tower Presence on Rotor and Wake Aerodynamics Using CFD

Author: Frederik Zahle, Niels N Sørensen and Helge Aagaard Madsen

This chapter describes a number of flow simulations on a modern wind turbine, where aspects such as the influence of wind shear, interaction between the rotor and tower and the nacelle and wake aerodynamics are investigated. In the simulations the actual geometry of the rotor and tower are resolved together with a fixed ground boundary. The simulations show that the azimuthal variation of the forces on the rotor operating in shear flow gives rise to some hysteresis effects that are very dependent on the nature of the shear. The power production is largely equal for simulations with and without shear. The simulations furthermore show that the effect of tower shadow is generally underpredicted compared to the BEM methods by as much as 100%. The nature of the flow in the nacelle region is highly unsteady with flow angles fluctuating by approximately $\pm20°$. The rotation in the wake gives rise to a bias in the prediction of the flow angle in this case of about $10°$. The wake development is strongly dependent on the freestream conditions, and for a case with strong shear and directional change in the vertical direction the wake is largely disintegrated three rotor diameters downstream.

3.1 Introduction

In Research in Aeroelasticity EFP-2006 [2] an investigation was carried out into the influence of wind shear on rotor aerodynamics using Computational Fluid Dynamics (CFD) and Blade Element Momentum (BEM) models. The study showed that the modelling of this flow case is not straightforward, and a comparison of the advanced flow models with various BEM implementations did not give any conclusive answers to the correct method to be used. In this year's Research in Aeroelasticity EFP-2007, this work has been continued and another computational approach has been taken that allows to include the ground boundary more directly in the computations, while still modelling the actual geometry of the rotor.

CFD simulations are used to investigate the effect of shear, tower shadow and nacelle and wake aerodynamics

Another topic that is also relevant to address with complex flow models is that of tower shadow, since little validation with CFD has been carried out previously. Although tower shadow usually only gives rise to fluctuations in the power of less than five percent, it is still important in order to capture the aeroelastic charactistics of the turbine correctly.

A third issue that is relevant is the aerodynamics in the nacelle region where instruments are placed to measure rotor yaw and flow speed. This problem has previously been addressed computationally and experimentally, and has primarily been focused around the estimation of the wind speed and less so on the estimation of the flow angle. As such, further work is needed to improve the understanding of the flow characteristics in this region.

This chapter will thus focus both on the continued investigation into the influence of the velocity shear on the turbine aerodynamics, as well as on of this year's mile stones, namely that of the interaction between rotor, tower and nacelle. In 2007, measurements on a Siemens 3.6MW turbine were carried out at Høvsøre Test Station in northern Jutland, where a Pitot tube was mounted at 36 m radius measurering all three velocity components. This turbine was therefore used in the present work since the experimental data was of high quality and could be used for validation of numerical flow solvers. Details of the experiment can be found in [1].

Three computations have been carried out for this work: one where the inflow is uniform, and two where a given velocity shear is prescribed. Both shears are equivalent to shear profiles that occur at night time, that can have very high vertical velocity gradients and where the ambient turbulence level is very low due to stratification. The first shear is defined from a power law

and has no directional change in the vertical direction. The second shear is extracted from the measurements at Høvsøre, and has a strong turning of the flow up through the boundary layer. Although very severe, these types of shears are quite common and therefore represent an important flow case in wind turbine aerodynamics.

Simulations of the type presented in this chapter are quite new in the field of wind turbine aerodynamics. In traditional Computational Fluid Dynamics (CFD) computations on wind turbine rotors non-uniform inflow conditions are rarely included due to the high computational cost. Also, including the tower and ground boundary is not normally done due to the added complexity needed in the code. Flow over isolated wind turbine rotors has been investigated extensively using CFD [see for example 3–7, 16–18]. More recently, Sørensen and Johansen [15] computed the flow over the rotor designed in connection with the UPWIND project operating in strongly sheared inflow, and showed that considerable hysteresis effects are present due to the non-uniform loading of the rotor. In the in-house Navier-Stokes flow solver Ellip-Sys3D [9, 10, 13] it has so far only been possible to compute the flow around an isolated rotor. Recently, Zahle [19] extended the code such that this relative movement could be modelled directly providing the basis for simulating the unsteady flow in a domain where the rotor is allowed to move relative to a stationary ground boundary.

This chapter is divided into six sections: firstly, the computational methods are described; secondly, the computational domains used in the simulations are discussed; thirdly, the results regarding the influence of shear, tower shadow modeling and nacelle aerodynamics are presented; and finally a discussion and conclusion summarises the findings.

3.2   Computational Methods

3.2.1   Base Solver

For all computations the EllipSys3D pressure based incompressible Reynolds averaged Navier-Stokes flow solver written by Michelsen [9, 10] and Sørensen [13] is used. The code uses the finite volume method, solving for the primitive variables u, v, w, and p, in general curvilinear coordinates. The variables are stored in a collocated grid arrangement, and odd/even pressure decoupling is avoided using the Rhie-Chow interpolation [11]. The iterative SIMPLE or PISO algorithm is used to advance the solution in time using a second-order accurate scheme. The convective terms are discretised using the Quadratic Upstream Interpolation for Convective Kinematics Scheme, QUICK, and the viscous terms are discretised using the central difference scheme. The momentum equations are solved decoupled from each other using a red/black Gauss-Seidel point solver. To accelerate the convergence of the pressure-correction equation a multigrid solution strategy is implemented combined with the additive Schwarz method, where each sub-domain is solved for simultaneously.

The code is fully parallelised using the MPI library with a multiblock decomposition of the solution domain. The block-block communication is done through one layer of ghost cells around each block. The cell vertices are required to coincide on interfaces such that conservation can be maintained.

For computations of flow over aerofoils and wind turbine blades the EllipSys3D code uses the $k - \omega$ SST model by Menter [8], because of its good performance in wall bounded adverse pressure gradient flows.

3.2.2   The Overset Grid Method

The overset grid method, also known as chimera or composite grid method, addresses many of the limitations of traditional structured grid methods, while at the same time maintaining their advantages such as solution strategies and parallelisation. The method allows for the decomposition of the problem into a number of simpler grids, which overlap each other arbitrarily. If

dealing with a multibody problem, appropriate body-fitted grids can be generated around each component, making it possible to model virtually any configuration. Since each body grid is independent of the other grids, problems involving relative movement of bodies are naturally handled.

Important flow features can be resolved by refined meshes, which together with the body fitted meshes can be embedded in background meshes that are successively coarsened towards the farfield where there is no need for high resolution of flow features. To accommodate the solid bodies and refined grids, cells are removed from the background grids where necessary.

In the present implementation by Zahle [19] each group of simply connected blocks is solved using boundary conditions on the overlapping interfaces based on interpolated values of velocity from neighbouring grids using trilinear interpolation. Since this interpolation is non-conservative, the lack of mass conservation must be addressed. An explicit correction of the conservation error is implemented, since a divergence free field is required to solve the pressure-correction equation. The correction is placed in internal cells along the overset boundaries and is distributed proportionally to the local mass flux. As stated above, only velocities are interpolated, since interpolation of velocities and pressure would lead to an ill-posed problem. The solution of the pressure is thus obtained on the basis of the mass fluxes calculated from the momentum equations.

The additional cost associated with the overset grid method is caused by the need for determining the connectivity between each block group and communication of boundary conditions between these groups. In EllipSys3D the connectivity routines are fully parallelised and apply a stencil jumping technique to locate cells. Likewise, the communication of flow field data must be carried out in a parallel manner. To minimize communication latency, non-blocking MPI calls are used to transfer information between individual processors.

The $k - \omega$ SST model has not yet been implemented for use on overset grids, since it requires the specification of two zonal functions that are computationally heavy to evaluate on moving overset grids. As such, only the original $k - \omega$ model can be used.

3.3   Computational Setup

The model of the Siemens 3.6MW turbine used in the present simulation is simplified compared to actual geometry. Firstly, the model does not include the nacelle since this would complicate the grid generation, and as the first step would be too time consuming to set up. Secondly, the rotor has no coning or tilt due to the fact that the overset version of the code at present can only handle rotation around the z-axis. Finally, the turbine is assumed to be completely rigid, since the flow solver is not capable of handling multibody dynamics. As such an approximate tower clearance was estimated from aeroelastic simulations using HAWC2. Figure 9 shows the turbine configuration and lists the overall dimensions of the turbine.

In the experiment a pitot tube was placed at a radius of 36 m on one of the blades. Likewise, a probe was placed in the computational domain at the same position. Additional probes were placed along the blade and three probes were placed in the approximate position where the nacelle anemometer is placed. Figure 10 shows the location of all nine probes.

In contrast to the standard patched multiblock approach that uses O-O grids commonly used for rotor computations, the overset grid method can handle the relative movement between the rotor, tower and ground boundary . In this work a topology with five overlapping mesh groups is used; one curvilinear on the rotor, another curvilinear grid around the tower, a Cartesian grid resolving the tower wake, a semi-cylindrical domain resolving the near-wake, and another semi-cylindrical domain for the farfield. This layout results in an efficient use of grid cells, and ensures good compatibility along the overset boundaries. The mesh for the three blades on the rotor contain 256×128×64 cells in the chordwise, spanwise, and normal directions, respectively, with a 64×64 cells 'tip' cap. To achieve y^+ values of less than 2 the height of

Figure 9. Main dimensions and axis definitions of the Siemens 3.6MW turbine.

Siemens 3.6MW Dimensions	
Rotor Diameter	107 m
Hub Height	90 m
Tower Diameter top	3.0 m
Tower Diameter bottom	4.5 m
Tower Clearance	9.0 m
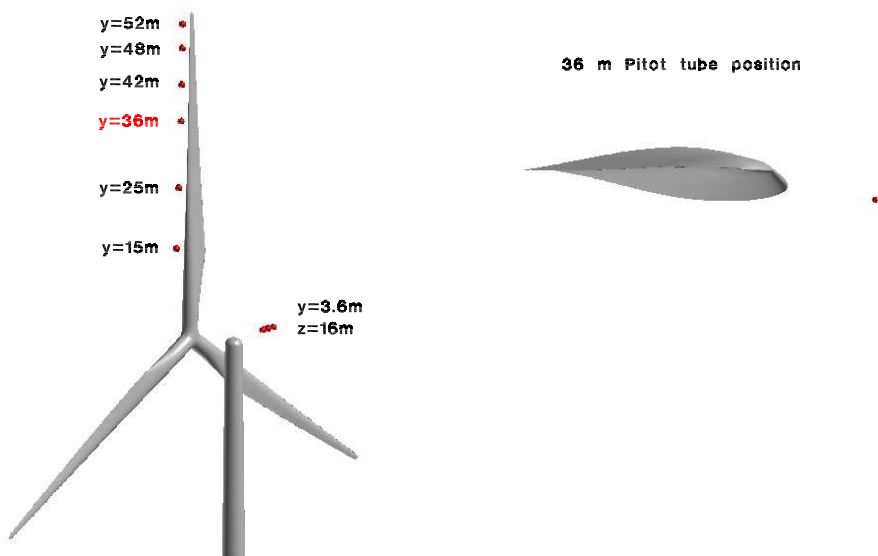
Figure 10. Positions of the velocity probes in the simulations.

the first cell in the boundary layer was 5×10^{-6} m. The tower grid contained 96 cells along the height of the tower, 256 cells in the cicumferential direction, with a 64×64 tip cap. The tower-wake grid was well-resolved approximately 5 tower diameters downstream and the near-wake grid was well-resolved approximately one rotor diameter downstream. The volume grids around the blades and the tower were generated using HypGrid [14]. The total number of cells in the grid was 17.4×10^6.

Rotor-tower mesh contains 17.4×10^6 grid cells.

Figure 11. Domain outline.

Figure 11 shows the domain layout for the modern MW turbine. The inflow boundaries are coloured in blue and the outlet is coloured in red. On the bottom boundary a symmetry (slip-wall) boundary condition was applied. Side and rear views of the mesh are shown in Figure 12.
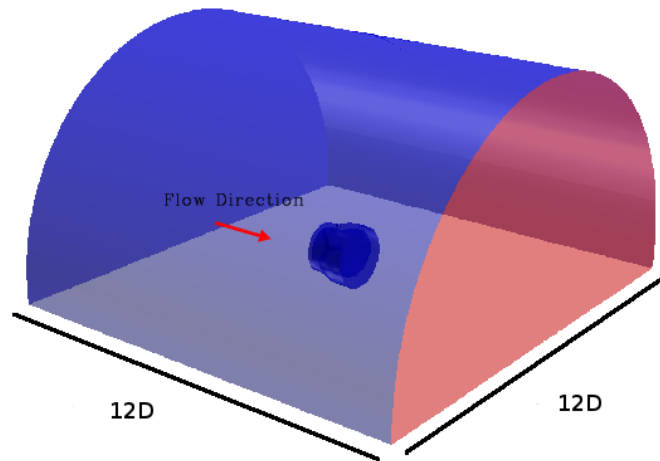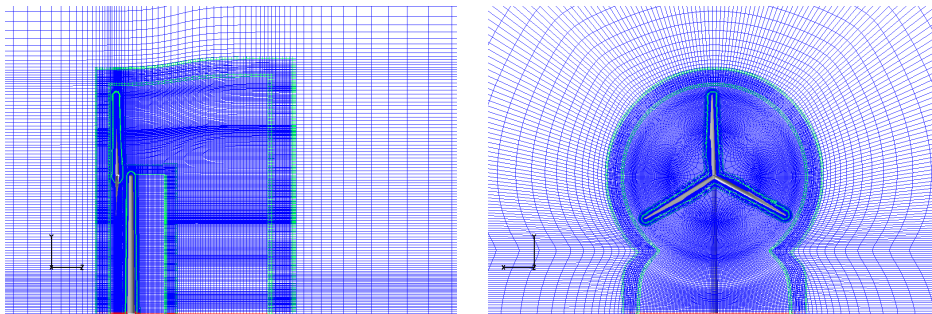

Figure 12. Side and rear view of the mesh.

Table 1 summarises the computational parameters used in the simulations presented in this chapter.

Computational Parameters	
Time integration	PISO
Convective terms	QUICK
Turbulence model	$k - \omega$
Time step	0.002 seconds
Subiterations	6
Grid Size	17.4×10^6 cells

Table 1. Summary of the computational parameters for the simulations.

In the present method it is possible to prescribe any inflow condition to the simulation without having to control it in the interior of the domain. This is because there is no actual wall condition at the ground boundary, since, as shown in Figure 11, the ground boundary is represented by a slip wall. When enforcing a no-slip wall boundary condition, a boundary layer will build up

Figure 13. Detailed view of the mesh showing the individual overlapping grids in the region around the tower.

that is dictated by the Reynolds number of the flow. In the present case, this would result in a turbulent eddy viscosity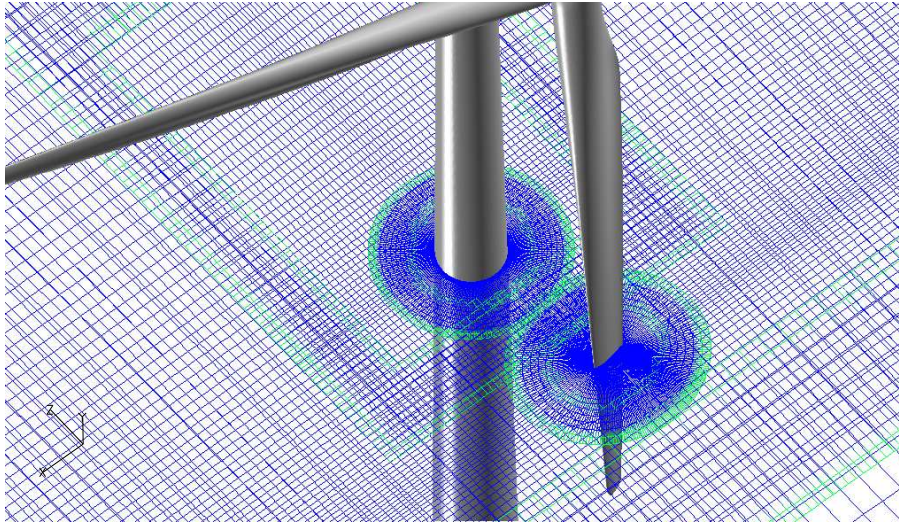 that would be many orders of magnitude higher than the molecular viscosity, reducing the effective Reynolds number seen by the rotor. The use of a slip wall at the ground may not be the best solution since the speedup below the rotor might be too high. However, it allows for an easy implementation of arbitrary shear flows, while no other alternative is easily available.

3.4 Effect of Inflow Shear

During night time, turbines have been observed to operate in shears where the velocity can vary as much as 6 m/s over the rotor disc, suggesting that dynamic effects can play an important role in such conditions. Two different inflow shears are used in the present computations. In the first one, the velocity shear profile is modelled as a power law as follows

$$U(z) = U_{hub} \left(z/z_{hub}\right)^{\alpha} \tag{10}$$

where z is the height above ground, U_{hub} is the inflow velocity at hub height, and α is the power coefficient, here set to 0.55, with no directional change in the vertical direction. In the second one the shear gradient is very similar with a slightly higher hub height velocity. The main difference between the two shears is that in the second one, the turning of the flow up through the atmospheric boundary layer is also included. The two shear profiles are shown in Figure 14. Both profiles represent typical night time velocity profiles, with very high shear combined with, in the second case, a strong turning of the flow up through the boundary layer. In the present computations the inflow is assumed to be laminar, which is justifiable since the strong stratification that is usually present at night causes the real flow conditions to be essentially laminar.

Severe shear profiles are common at night. Inflow is essentially laminar.

Looking firstly at the simulation carried out with the power law shear profile, Figure 15 shows the axial and tangential force along the blade plotted for four azimuthal positions normalised with the force distribution at an azimuth angle of 0 degrees. The axial force reduces quite uniformly along the blade during the rotational cycle, whereas the tangential force is reduced considerably more on the outer part of the blade at the 180 degree azimuth position. The difference between the load at the 90 degree and 270 degree azimuth positions is rather modest, indicating only little hysteresis during the cycle. The hysteresis effects are, as might be expected, clearly stronger on the inner part of the blade where the incidence is larger and the reduced frequency based on the rotational frequency is higher.

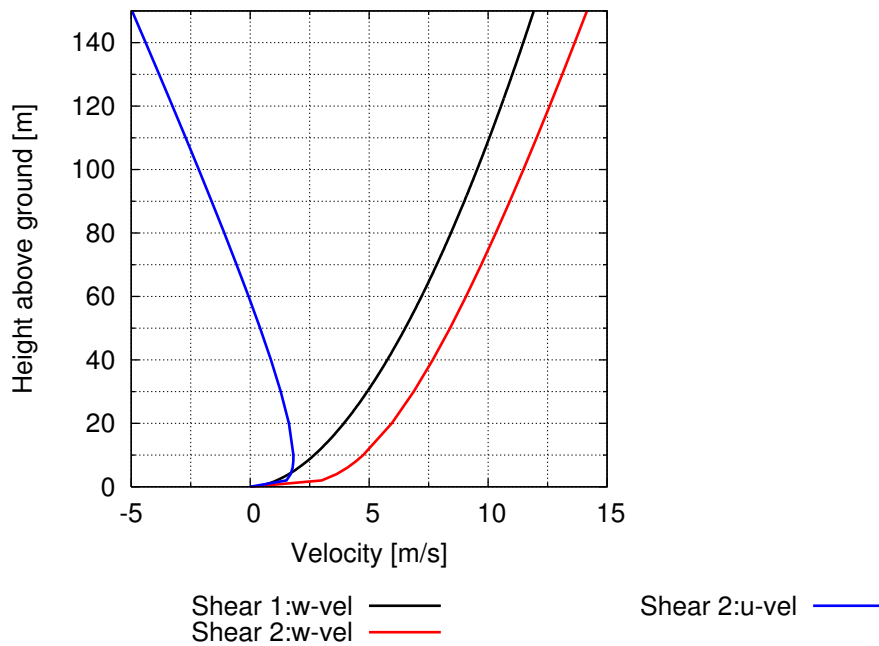Hystersis effects are strongest towards the root of the blade.

Figure 14. The shear profiles used in the shear computations. This profiles represent severe, yet typical, night time situation seen at Høvsøre test station.
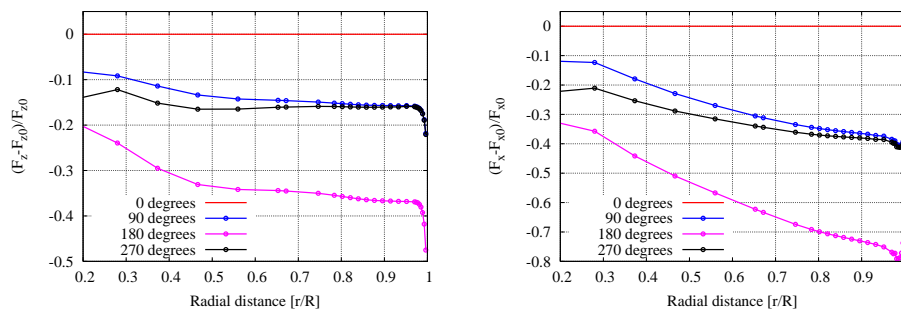

Figure 15. Normalised blade normal and tangential force at four azimuthal positions for the power law shear profile computation.

The power production of the turbine operating in shear was compared to an identical setup where the inflow velocity was uniform and equal to the velocity at hub height in the shear computation. The results for the two computations agree well with the findings of Sørensen and Johansen [15] in that the power and thrust are largely identical only differing by less than 1%. It should be noted that the shear profile used in the present simulations is identical to the one used in Sørensen and Johansen [15], and as is noted in this paper, this behaviour might be dependent on the actual shape of the shear profile.

In Figure 16 the normalised axial velocity in the vertical symmetry plane at r/R=0.79 is shown for the shear computation compared to the uniform inflow computation. The flow blockage is clearly comparable for the two types of inflow, and at this wind speed the rotor does not have any effect on the incoming flow beyond two diameters upstream of the rotor.

Figure 17 shows the axial velocity shear profile at various positions upstream and downstream of the rotor. It is evident that the rotor does not have a large effect on the flow upstream. The flow is accelerated considerably below the rotor, due to the presence of the ground, whereas the unconstrained flow on the upper part of the rotor is not accelerated as much. The wake expands considerably more downward than upward, with a subsequent upward shift and contraction of the wake around two diameters downstream.

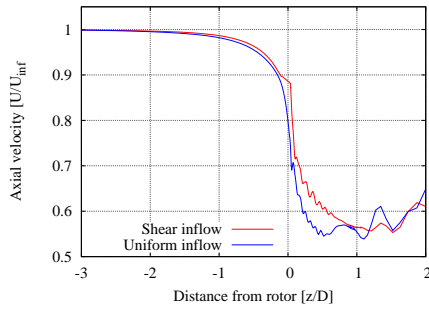Flow is accelerated below the rotor due to the ground proximity.

Figure 16. Normalised axial velocity along a line through the rotor plane at r/R=0.79 for the modern MW turbine.
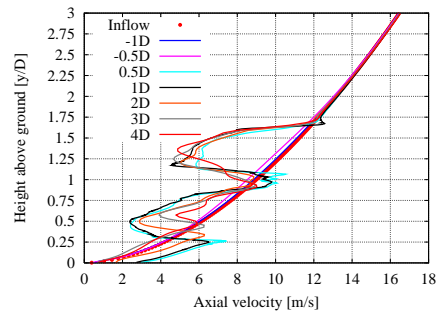
Figure 17. Velocity shear profile upstream and downstream of the MW turbine rotor.

Secondly, results from the computation carried out with the Høvsøre shear profile that also includes a directional change of the flow up through the atmospheric boundary layer is presented. Figure 18 shows the normalised blade normal and tangential force. Compared to Figure 15, the forces are roughly equivalent at the 180 degree azimuth position, with a large reduction in the forces on the blades. At the 90 and 270 degree azimuth positions the forces differ slightly; however, not in a manner consistent with the first case, where there was a lag of the forces at the 270 degree position. Here there is a reduced load on the inner part of the blade and an increased load on the outer part.

Hysteresis effects are again strongest towards the root.
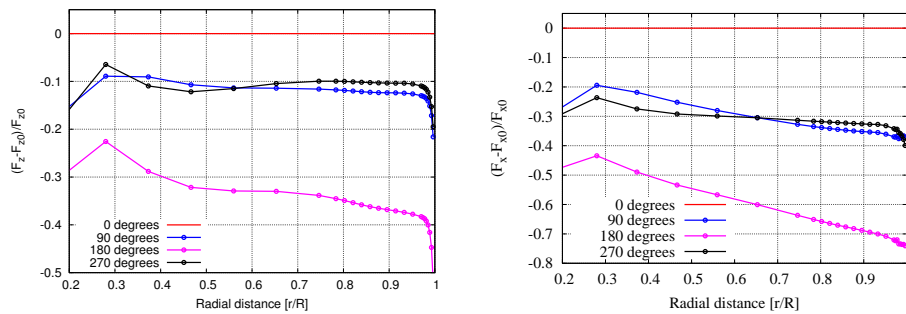
Figure 18. Normalised blade normal and tangential force at four azimuthal positions for the Høvsøre shear profile computation.

3.5 Rotor-Tower Interaction

In the following two sections the results for the two computations where both rotor and tower is included will be presented where the focus is on the rotor-tower interaction.

3.5.1 Turbine in Uniform Inflow

The simulation with uniform inflow was carried out to examine the tower shadow effects in an isolated manner, and to make a basic comparison to the results obtained with the BEM code implemented in HAWC2.

Figure 19 shows a comparison of the rotor thrust and torque over one revolution computed using CFD and BEM, respectively. BEM appears to consistently overpredict the tower shadow compared to the CFD results by as much as 100% on both the thrust and the torque. EllipSys3D predicts approximately 1% reduction of the thrust during tower passages, and an approximate 2% reduction on the torque. BEM predicts these to be 2% and 4%, respectively. Both CFD and BEM show a slight lag in the tower shadow. Note that the absolute values of thrust and torque

differed by approximately 10% which can be attributed to the turbulence model used in the CFD computations.

Figure 19. Normalised thrust and torque for the turbine operating in uniform inflow conditions.

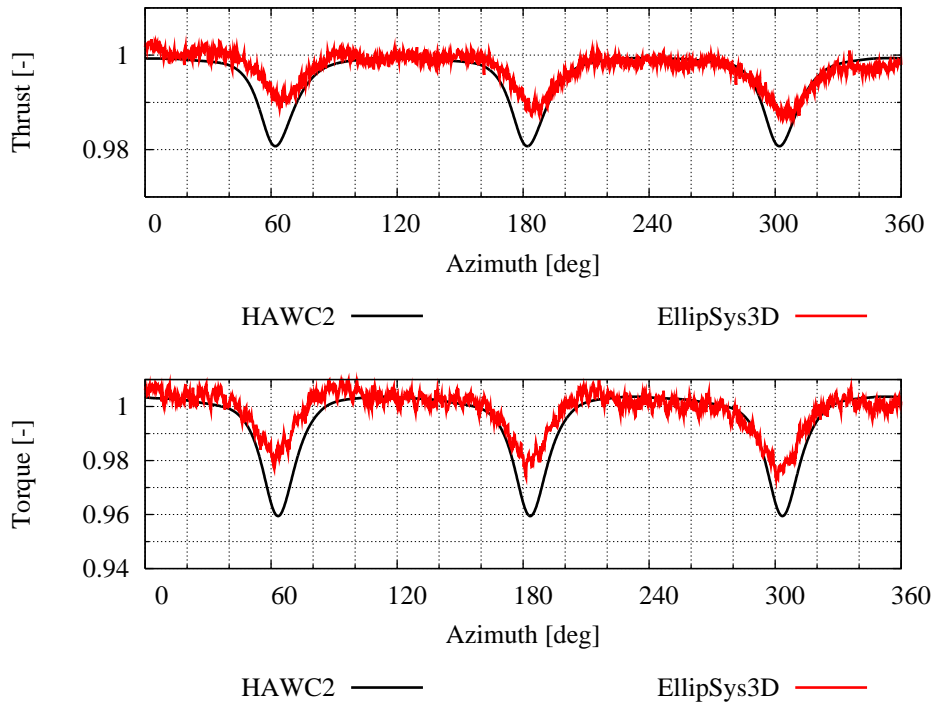Figure 20 shows the normalised tower bottom tilt and roll moments over one revolution only including forces on the tower. During free flow conditions the tilt moment is rather constant, whereas the blade passages induce a large suction on the front of the tower causing the moment to approach zero. The roll moment is likewise dominated by the blade passages, with little influence of the periodic forces caused by tower vortex shedding.

The tower bottom tilt moment for the entire turbine, Figure 21, shows an approximate 1.5% reduction during blade passages that span over approximately 40° azimuth. The tower shadow is not exactly symmetric in that the recovery is slightly slower than the entry reduction in moment.

The local flow angle and relative flow speed were extracted at r/R=0.68 and compared to BEM computations, Figure 22 . Note that both the BEM computed LFA and flow speed were shifted to match that obtained using CFD.

The CFD results show an increasing LFA as the blade travels from an azimuth of zero towards 180° azimuth. This is thought to be due to the slip wall condition that gives rise to a slight flow acceleration below the rotor disc, which is not included in the BEM model.

Looking closer at the tower vortex shedding, Figure 23 shows the non-dimensionalised sectional side force on the tower at three vertical positions, one inside the rotor disc (h/H=0.55), and two below (h/H=0.27 and h/H=0.16). The side force inside the rotor disc is clearly dictated by the blade passage frequency with high spikes during a blade passage. However, it is evident that the vortex shedding below the rotor disc is also in phase with the blade passage frequency, resulting in a Strouhal number ($St = \frac{fD}{U}$) equal to 0.25. This is quite close to the natural frequency of a circular cylinder, which is typically 0.2, which suggests that a type of lock-in phenomena could be at play. The simulation has, however, not run for very long, and it is well known that vortex shedding can take a long while before it builds up. As such the shedding frequency could shift if a longer simulation time was allowed.
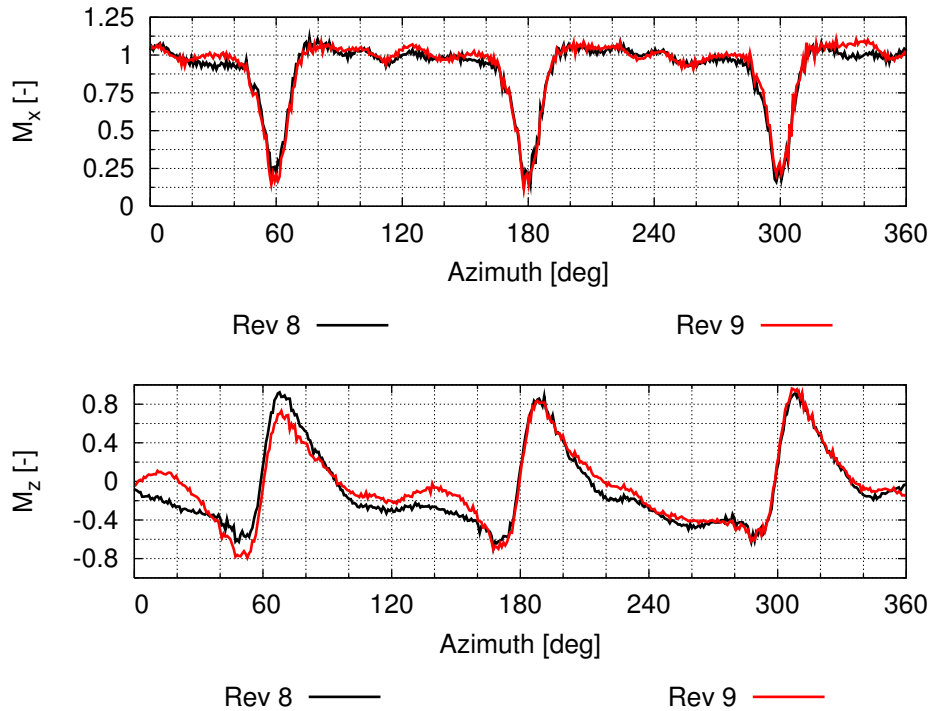
Figure 20. Normalised tower bottom tilt and roll moment on the tower for the turbine operating in uniform inflow conditions.
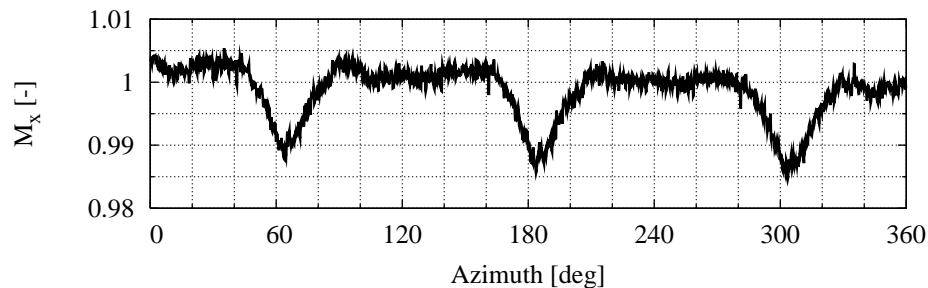
Figure 21. Normalised tower bottom tilt moment for the turbine (rotor+tower) operating in uniform inflow conditions.

3.5.2 Turbine in Shear Inflow

Figure 14 shows the shear profile prescribed at the inlet for the present simulation.

Figure 24 shows the thrust and torque for the CFD and BEM computations. As in the uniform inflow case, the tower passage gives rise to the largest variation in both quantities, approximately 1.5% in thrust and 2% in torque in the CFD computations. The thrust exhibits a fairly unsteady behaviour reaching a maximum when blades are at approximately $40°$ azimuth ($160°$ and $280°$ azimuth for blade 2 and 3). A similar behaviour is predicted by the BEM computations, although the maximum seems to be reached slightly earlier than for the CFD computations. The tower shadow is, as opposed to the uniform inflow case predicted quite well for the thrust, whereas there is still a discrepancy on the torque.

Figure 25 shows the tower root tilt and roll moment, that behave largely as seen for the uniform

Good qualitative agreement between CFD and BEM.
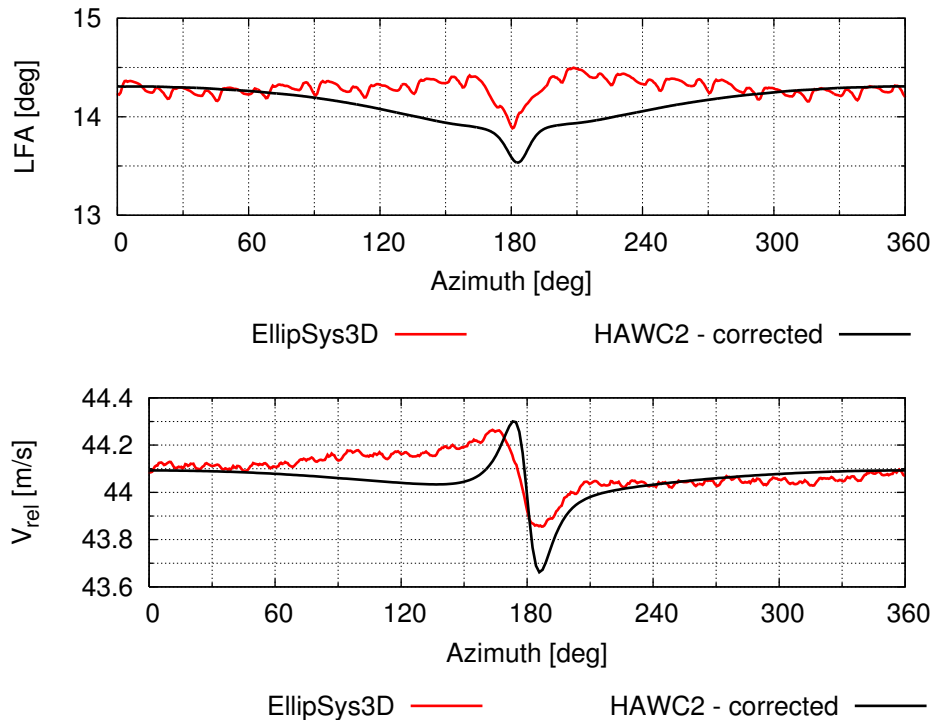
Figure 22. Local flow angle and relative speed at r/R=0.68 for the turbine operating in uniform inflow conditions.

Figure 23. Tower side force coefficient at three heights for the uniform inflow case. Note that the plots for h/H=0.16 and h/H=0.27 have been multiplied by two for clarity.

inflow case, with a slightly larger variation between two consecutive passages. The blade passages give rise to a large reduction in the tilt moment and a large oscillation of the roll moment. However, the roll moment has a large degree of variation in between blade passages possibly caused by vortex shedding.

Looking at the total tower bottom tilt moment for the rotor and tower, Figure 26, there is again a slightly larger variation than for the uniform inflow case, and a similar reduction of approximately 2.5% during a blade passage.

Tower shadow gives rise to 2.5% reduction if tilt moment.

As shown in Figure 27 the local flow angle and relative wind speed were as in the uniform inflow case extracted at r/R=0.68 and compared to HAWC2 computations and the experimental results. In the CFD computations these quantities were extracted at a position approximately equivalent to that of the Pitot tube in the experiment, see Figure 10. The curves have been shifted to match the EllipSys3D curve at an azimuth angle of zero.
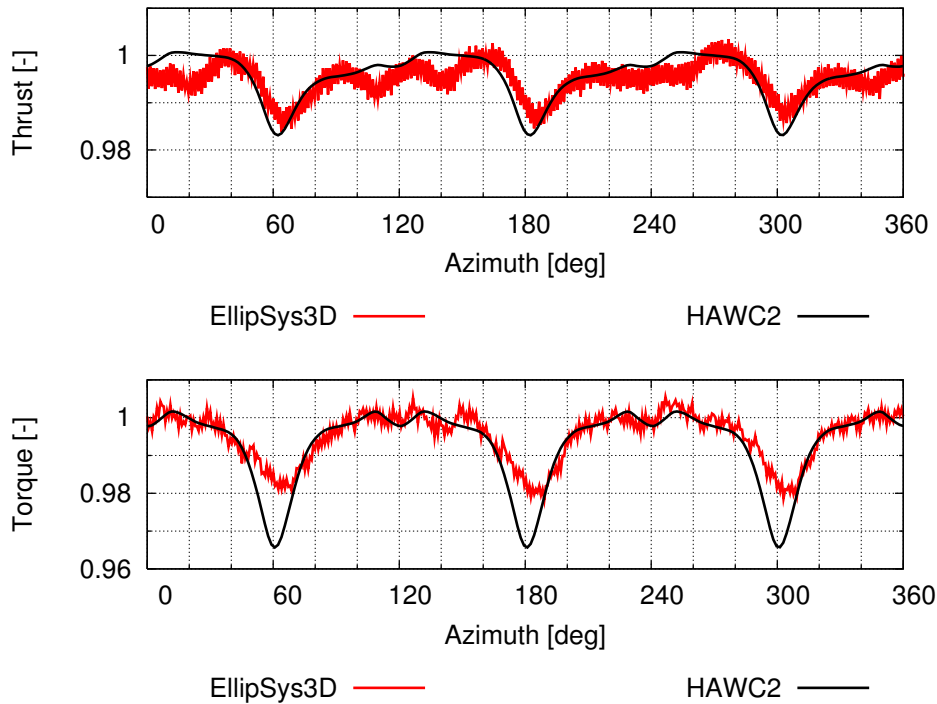
Figure 24. Normalised thrust and torque for the turbine operating in uniform inflow conditions.
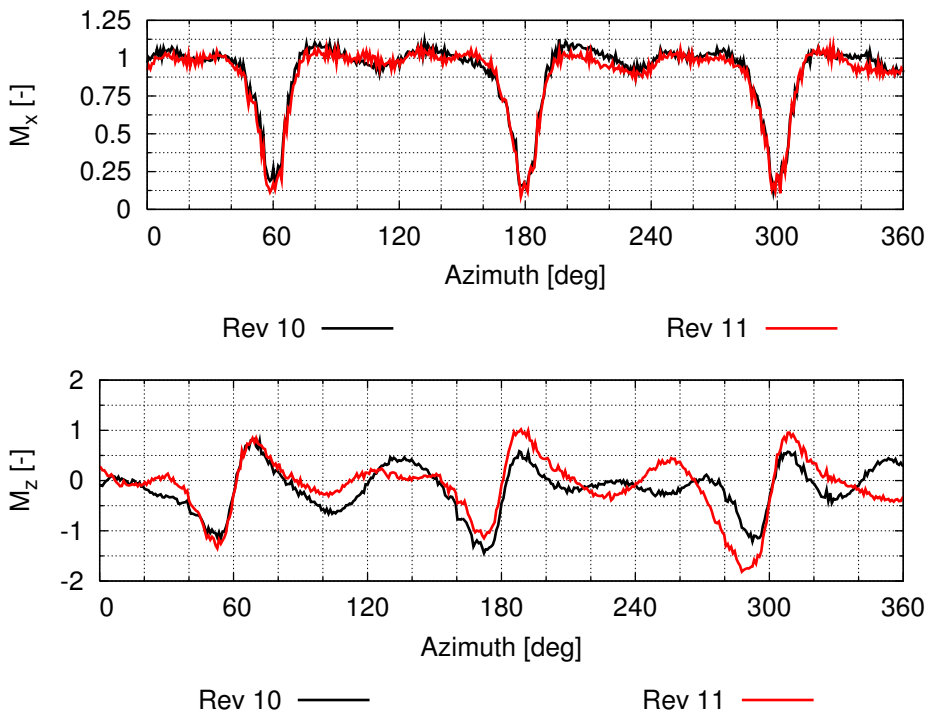
Figure 25. Normalised tilt amd roll moment on the tower for the turbine operating in shear inflow conditions.

The fact that the computations did not include any coning of the rotor, as well as having assumed the blade to be rigid, is another possible cause for the relatively poor agreement. Another possible cause for the discrepancy is that the u-component of the shear profile was assumed to
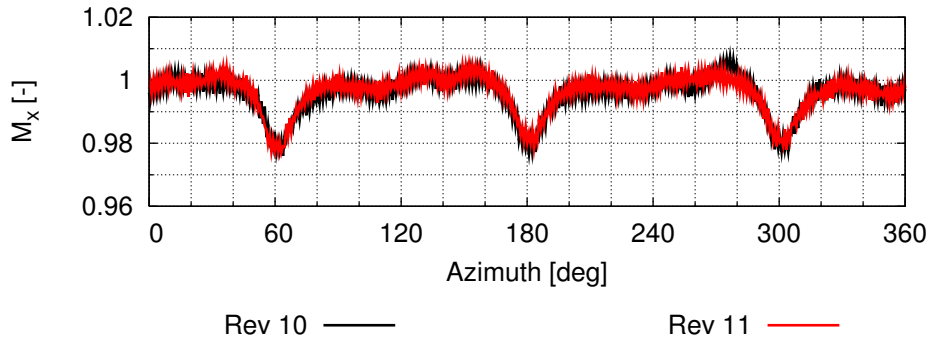
Figure 26. Normalised tilt moment for the turbine (rotor+tower) operating in shear inflow conditions.
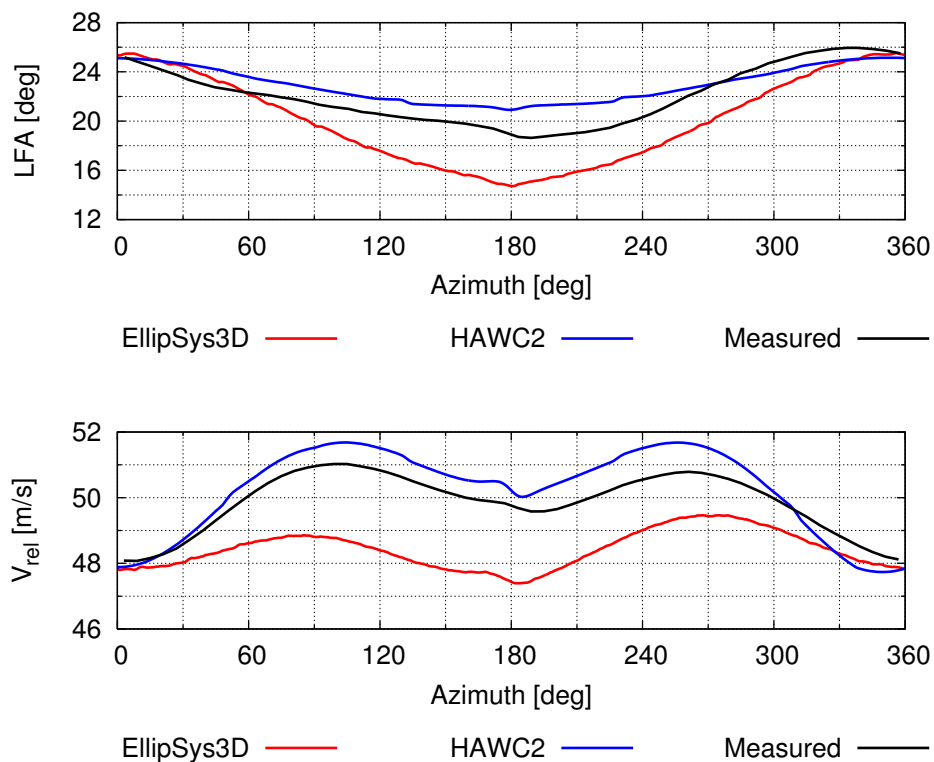
Figure 27. Local flow angle and relative flow speed at r/R=0.68 for the turbine operating in shear inflow conditions.

be linearly decreasing towards the ground, resulting in a large positive u-component below the rotor disc. In retrospect, this is perhaps not so realistic, however, due to time constraints, new simulations could not be done.

Similar to the uniform inflow case, Figure 28 shows that the sectional tower side force is dominated by the blade passage frequency inside the rotor disc. Below the rotor disc, the BPF is still visible in the response, however, the vortex shedding is clearly not in phase with the BPF. This suggests that there is no clear lock-in phenomena taking place most likely due to the fact that the natural frequency of the vortex shedding is different along the span of the tower due to the strong velocity shear.
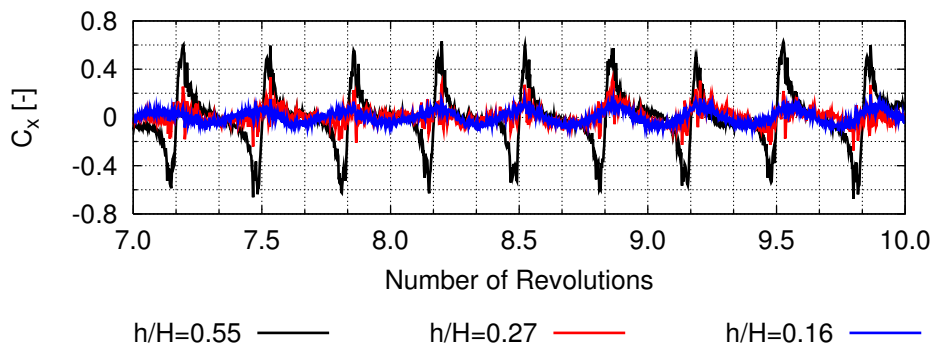
No lock-in observed.
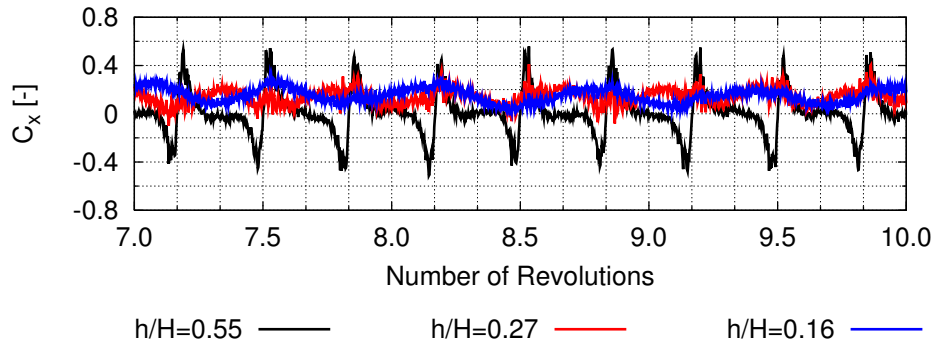
Figure 28. Tower side force coefficient at three heights. Note that the plots for h/H=0.16 and h/H=0.27 have been multiplied by two for clarity.

3.6 Rotor- "Nacelle" Interaction

In the literature earlier works have addressed the issue of nacelle aerodynamics using computational methods [12]. These works, focused mainly on predicting the flow velocity and less on the flow angle, and used an actuator disc model in place of an actual representation of the rotor. In turn, these works had a very detailed representation of the nacelle. Although the present computation did not include the nacelle, some observations can be made regarding the probable nature of the flow in the nacelle region since the flow is thought to be dominated by the rotating blades and less so by the exact shape of the nacelle. In the following the computation including shear and turning of the flow in the vertical direction is used. Three velocity probes were placed at the approximate location where the anemometer is placed, as shown in Figure 10 which is also indicated in Figure 29. The figure shows the axial velocity and vorticity magnitude from two different perspectives.

As is evident, the flow is highly unsteady in this area, with influence from the vortices shed from the cylindrical region on the blades, as well as the root vortices.
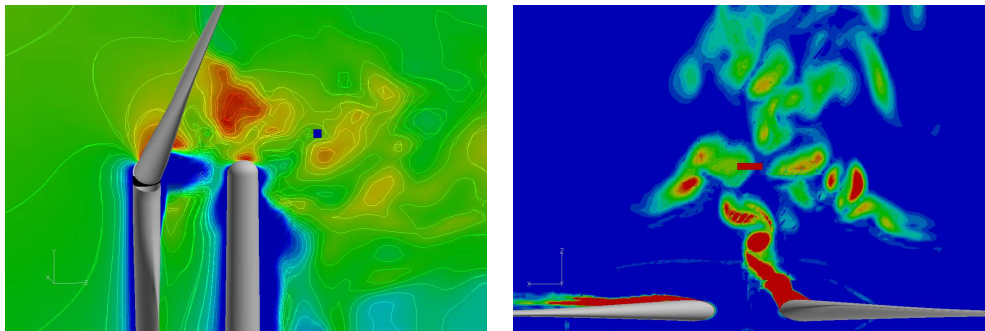
Figure 29. (left) Side view showing axial velocity and (right) top view showing vorticity magnitude in the nacelle region for the turbine operating in shear inflow conditions.

Figure 30 shows the computed flow speed and yaw angle at the three probes for the computation. The averaged flow speeds measured over 14 revolutions at the three probes was predicted to being 11.62 m/s, 11.56 m/s, and 11.09 m/s, respectively. Compared to the freestream velocity of 11.29 m/s, the deviation is crearly very small. For this shear inflow case, the turbine operates at approximately $9°$ yaw measured at hub height. The probes measure a large variation of the flow angle of up to $\pm 20°$. Taking an average of the measured flow angles, predicts a yaw angle of $-3.40°$, $-2.43°$ and $-1.89°$, respectively, for the three probes. A likely cause of this is the wake rotation, that gives rise to a counter-clockwise angular velocity, which for this flow case appears to balance with the inflow cross-flow velocity, resulting in a greatly reduced yaw angle measurement.

Good estimation of flow speed. Large discrepancy in flow angle.
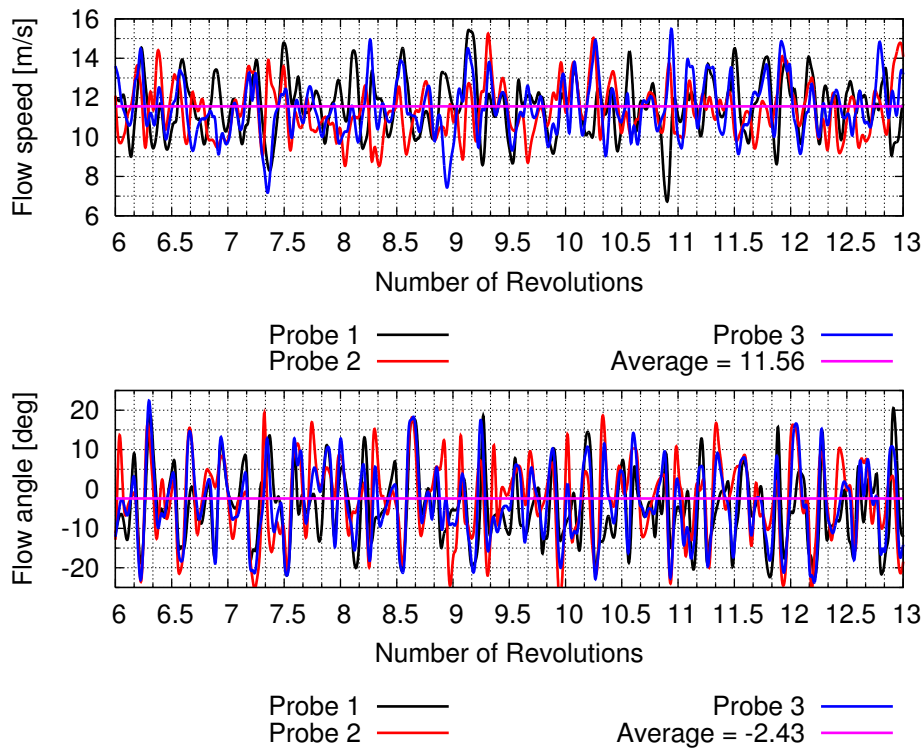
Figure 30. Probe flow speed and yaw angle at hub height for the shear inflow computation.

If indeed these findings are consistent with observations on modern wind turbines, further investigation might give insight into a possible correction of the yaw error.

3.6.1 Wake Development

The final aspect of this work is an investigation of the development of the wake. In this section, the focus will solely be placed on the two shear inflow computations. Looking firstly on the case without directional change of the inflow in the vertical direction, Figure 31 shows the axial velocity at various distances downstream of the turbine. The deficit immediately downstream of the rotor is asymmetric as a result of the combination of variation of the load across the rotor disc and rotation of the wake. Further downstream the asymmetry becomes more pronounced with an entrainment of low velocity flow that surges upwards as the wake develops.

Turning to the flow case where the flow direction changes in the veirtical direction, it is evident from Figure 32 that the wake develops in a highly three-dimensional manner, caused by the combination of the azimuthal variation of the rotor loading, the wake rotation and the free stream transport velocity. Due to the strong cross flow component the wake is skewed strongly, resulting in the wake being largely disintegrated three diameters downstream. The wake rotation causes the low velocity flow from the bottom of the wake to be ejected upwards as the wake travels downstream, as well as seemingly ejecting the tower wake upwards.

Wake rotation is important for development of wakes in shear flow.

Combination of shear and flow turning causes wake to disintegrate quickly.

3.7 Conclusions

In the present work a number of CFD simulations have been carried out on the Siemens 3.6MW wind turbine for various flow situations. The influence of shear on the rotor loads was investigated, and it was found that the azimuthal variation of the load gave rise to some hysteresis in the axial and tangential forces. The integrated rotor thrust and power were largely identical to simulations carried out with uniform inflow. However, this might well be dependent on the
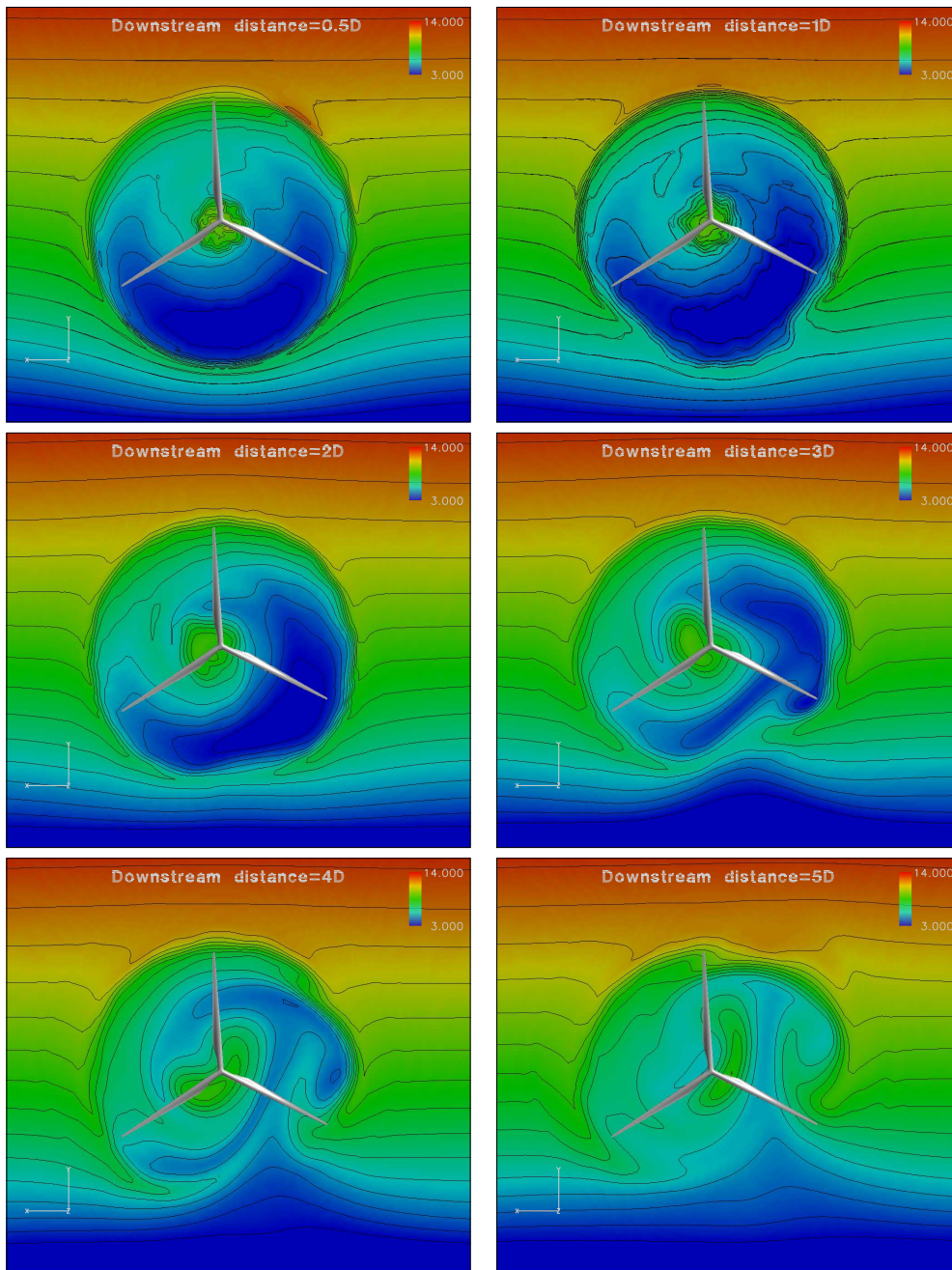
Figure 31. Contour plots of axial velocity downstream of the turbine operating in a shear without a directional change in the vertical direction.

shape of the shear and not a general trend. The influence of tower shadow has been investigated for two flow cases, one with and another without inflow shear. Generally, the CFD results underpredicted the tower shadow by as much as 100% compared to BEM computations, which gives cause for further investigation. Although the nacelle was not included in the simulations the flow in the region of the nacelle anemometer was investigated, and it was found that the measured flow angle in the wake differed by as much as 7° relative to the freestream flow angle. As such, for the flow case where the turbine operated in 10° yaw error, the flow angle in the wake of the turbine measured on average -0.08°, giving a possible explanation to the apparently consistent yaw error observed in the Høvsøre experiment. The investigation of the wake development downstream of a turbine operating in a shear flow showed that a rotation in the wake gave rise to significant mixing of the low velocity flow from the bottom half of the wake into the top half. Additionally, for the flow with large turning of the shear in the vertical
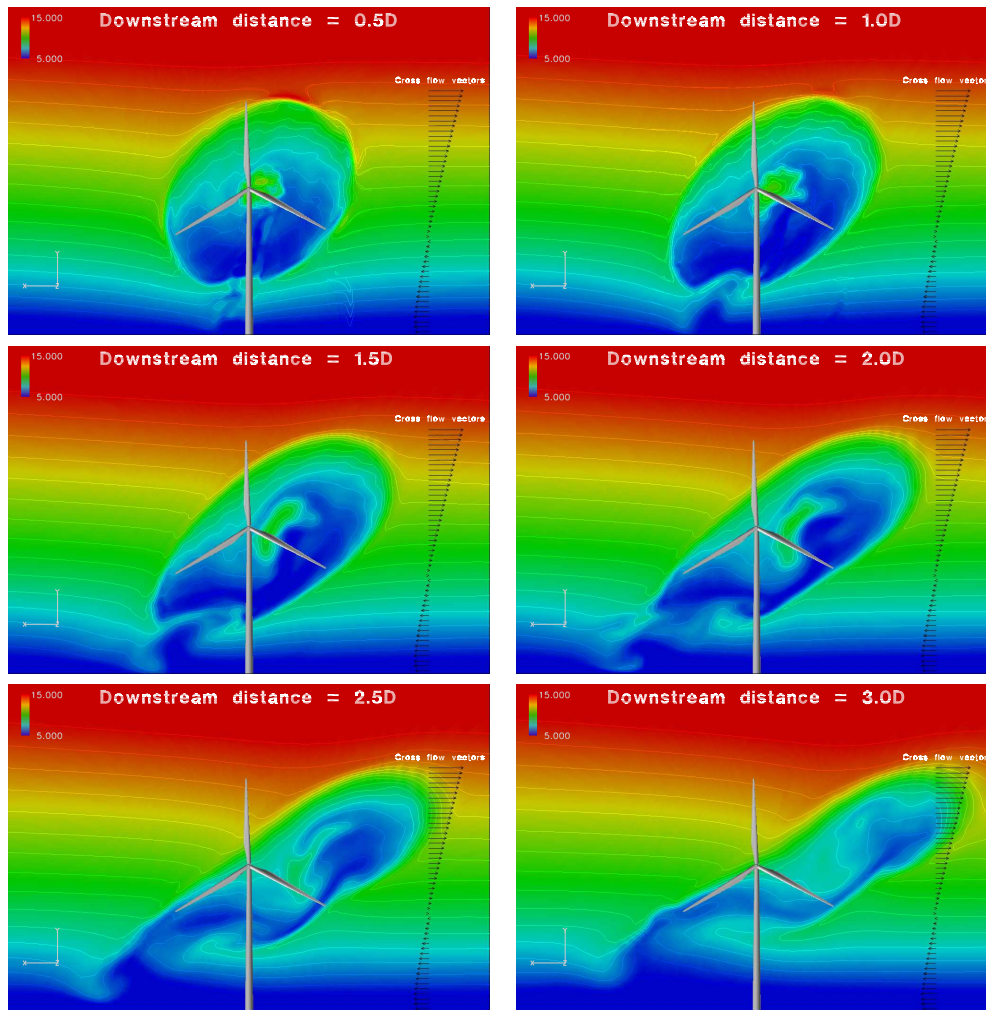
Figure 32. Contour plots of axial velocity downstream of the turbine operating in a shear with a directional change in the vertical direction.

direction, the wake was largely disintegrated only three diameters downstream of the turbine.

References

[1] H. Aagaard Madsen, C. Bak, U. Schmidt Paulsen, M. Gaunaa, J. Johansen, P. Fuglsang, P. Enevoldsen, J. Laursen, J. Romblad, and L. Jensen. The DAN-AERO MW experiments. In *To appear in Proceedings of the 2009 AIAA Aerospace Conference and Exhibit, Orlando, USA*, 2009.

[2] E. by Christian Bak. Research in aeroelasticity efp-2006. Technical Report Risø-R-1611(EN), Risø National Laboratory DTU, July 2007.

[3] E. P. N. Duque, C. P. van Dam, and S. C. Hughes. Navier-Stokes simulations of the NREL combined experiment Phase II rotor. *AIAA paper 99-0037*, 1999.

[4] E. P. N. Duque, M. D. Burklund, and W. Johnson. Navier-Stokes and comprehensive analysis performance predictions of the NREL Phase VI experiment. *Solar Energy Engineering*, 125:457–467, 2003.

[5] J. Johansen, N. N. Sørensen, J. Michelsen, and S. Schreck. Detached-eddy simulation of flow around the NREL Phase-VI rotor. *Wind Energy*, 5(2-3):185–197, 16-19 June 2003.

[6] A. Le Pape and J. Lecanu. 3D Navier-Stokes computations of a stall-regulated wind tur-

bine. In *The Science of Making Torque from Wind*, pages 78–88, Delft, The Netherlands, April 2004. EWEA.

[7] H. A. Madsen, N. N. Sørensen, and S. Schreck. Yaw aerodynamics analyzed with three codes in comparison with experiment. In *Proceedings of 2003 ASME Wind Energy Symposium*, number AIAA-2003-0518, 2003.

[8] F. R. Menter. Zonal two-equation $k - \omega$ models for aerodynamic flows. *AIAA paper 93-2906*, 1993.

[9] J. A. Michelsen. Basis3D—a platform for development of multiblock PDE solvers. Technical Report AFM 92-05, Technical University of Denmark, 1992.

[10] J. A. Michelsen. Block structured multigrid solution of 2D and 3D elliptic PDEs. Technical Report AFM 94-06, Technical University of Denmark, 1994.

[11] C. M. Rhie and W. L. Chow. Numerical study of the turbulent flow past an aerofoil with trailing edge separation. *AIAA journal*, 21:1525–1532, 1983.

[12] A. Smaili and C. Masson. On the rotor effects upon nacelle anemometry for wind turbines. *Wind Engineering*, 28(6):695–714, 2004.

[13] N. N. Sørensen. General purpose flow solver applied to flow over hills. Technical Report Risø-R-827(EN), Risoe National Laboratory, 1995.

[14] N. N. Sørensen. HypGrid2D—a 2-D mesh generator. Technical report, Risø-R-1035(EN), Risoe National Laboratory, 1998.

[15] N. N. Sørensen and J. Johansen. UPWIND, aerodynamics and aero-elasticity: Rotor aerodynamics in atmospheric shear flow. In *Proceedings of the 2007 EWEC Conference*, Milan, Italy, 2007.

[16] N. N. Sørensen, J. A. Michelsen, and S. Schreck. Navier-Stokes predictions of the NREL Phase VI rotor in the NASA Ames 80ft $\times$ 120 ft wind tunnel. *Wind Energy*, 5:151–169, 2002. doi: 10.1002/we.64.

[17] G. Xu and L. N. Sankar. Effects of transition, turbulence and yaw on the performance of horizontal axis wind turbines. *AIAA Paper 2000-0048*, 2000.

[18] G. Xu and L. N. Sankar. Computational study of horizontal axis wind turbines. *AIAA Paper 99-0042*, 1999.

[19] F. Zahle. *Wind Turbine Aerodynamics Using an Incompressible Overset Grid Method*. PhD thesis, Imperial College, London, 2006.

4 Analysis of Rotational Effects in the Boundary Layer of a Wind Turbine Blade

Author: Jens N. Sørensen and Carlos E. Carcangiu

It is well-known that the boundary layer properties of wind turbine blades are affected by rotational and 3–D flow effects. In spite of this, the industrial design approach is based on employing the blade–element momentum (BEM) theory with lift and drag forces determined from 2–D measurements. The results obtained are quite accurate in the proximity of the design point, but in stalled conditions the BEM is known to underpredict the blade loading, as shown e.g. in [1]. A likely explanation for the underprediction is that the flow is not adequately modelled by static 2D airfoil data in the stalled regime. From experiments and CFD computations it has been shown that radial flow exists in the bottom of separated boundary layers on rotating wings and it is likely that this alters the lift and drag characteristics of the individual airfoil sections. The physics behind this is that the outflow induces a Coriolis force in the chordwise direction which acts as a favorable pressure gradient that tends to delay boundary layer separation [2]. Further, the centrifugal force produces a spanwise pumping effect, which results in a thinning of the boundary layer.

The present work aims at analysing rotational effects in the boundary layer of a wind turbine blade using input from computer simulations. However, before going into the details of the analysis, we here give a brief introduction to former work.

4.1 Former works

Three-dimensional effects in the boundary layer of rotor blades was firstly described by Himmelskamp [3] who measured the performance of a propeller and found lift coefficients as high as 3 near the hub (see Figure 33). Later experimental studies have confirmed these early results, indicating both a delay in the stall characteristics and enhanced lift coefficients. Measurements on wind turbine blades have been performed by Ronsten [4], showing the differences between rotating and non–rotating pressure coefficients and aerodynamic loads, and by Tangler and Kocurek [5], who combined results from measurements with the classical BEM method to compute lift and drag coefficients and the rotor power in stalled conditions. Recently, the NREL Unsteady Aerodynamic Experiment in the NASA-Ames wind tunnel (see Schreck [6]) has considerably increased the knowledge of rotational effects on rotor blades. In this experiment a 10 m diameter test turbine developed at NREL was placed in the 24.4 m by 36.6 m (80 ft. x 120 ft.) NASA-Ames wind tunnel. Most emphasis was put on pressure distributions over the blade and a considerable amount of data has been collected. The data were the starting point for an international cooperation project, the IEA Annex XX: "HAWT Aerodynamics and Models from Wind Tunnel Measurements" aiming at analyzing the NREL data to understand flow physics and to enhance aerodynamic subcomponent models. A similar European project was recently undertaken under the acronym "MEXICO" (Model Rotor Experiments under Controlled Conditions). In this project, a three bladed rotor model of 4.5 m diameter was tested in the DNW wind tunnel, with one of the blades instrumented with pressure sensors at 5 radial locations. The data from this experiment are now being analysed and will form the basis of an extension of the aforementioned IEA Annex.

A pioneering work on explaining rotational effects on rotating blades was carried out by Sears [7], who derived a set of equations for the potential flow field around a cylindrical blade of infinite span in pure rotation. He demonstrated that the spanwise velocity component only depends on the 2-dimensional potential flow and that it is independent of the span (this is sometimes referred to as the *independence principle*). Later, Fogarty and Sears [8] extended the analysis to the potential flow around a rotating and advancing blade. They confirmed that, for a cylindrical

Investigations of the rotational effects on the aerodynamics of rotors have been ongoing for decades.
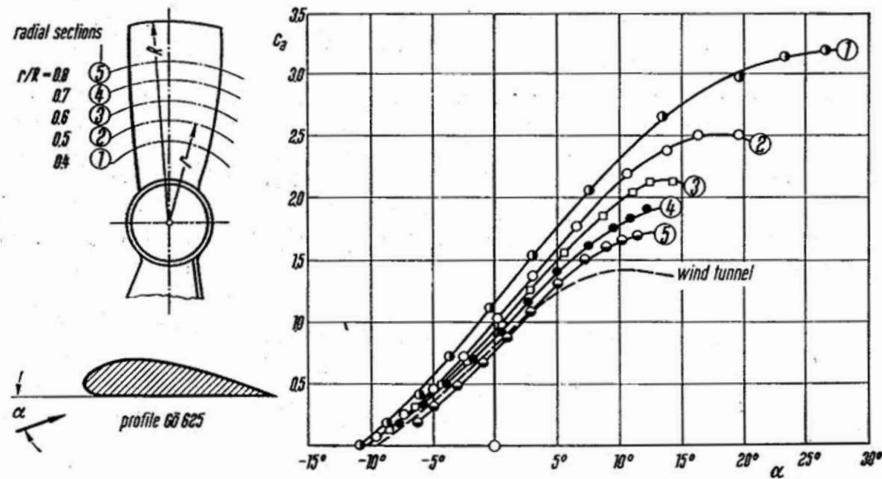
Figure 33. Lift coefficients at various radial sections on a rotating propeller, measured by Himmelskamp in 1945 [20]

Experiments and also analytical and numerical analysis have been carried out by several researchers to investigate the rotational effects on rotating blades.

blade advancing like a propeller, the tangential and axial velocity components are the same as in a 2–D motion with the same local relative speed and incidence. A more comprehensive work was later carried out by Fogarty [9], dealing with numerical computations of laminar boundary layers on a rotor blade. Here it was shown that the separation line is unaffected by rotation and that the spanwise velocity component in the boundary layer is small, as compared to the chordwise component. A theoretical analysis by Banks and Gadd [10] focussed on demonstrating how rotation delays laminar separation. They found that the separation point is postponed due to rotation, and that the boundary layer close to the hub is completely stabilized against separation. McCroskey and Dwyer [11] studied secondary effects in laminar incompressible boundary layers of helicopter rotor blades, combining numerical and analytical approaches. They showed that the Coriolis force in the crossflow direction becomes more important when approaching the rotational axis. On the other hand, they also found that the centrifugal pumping effect is weaker than expected. Its contribution, however, increases as the magnitude of the adverse pressure gradient increases.

In the last two decades computational fluid dynamics (CFD) has developed tremendously, and the study of boundary layers on rotating blades has often been carried on through a numerical approach. Twenty years ago, Sørensen [12] numerically solved the 3–D the boundary layer equations on a rotating wing, using a viscous–inviscid interaction model. In his results the position of the separation line still appears the same as for 2–D predictions, but near the separation line the difference between 2–D and 3–D lift coefficients becomes more pronounced. A quasi 3–D approach, based on viscous–inviscid interaction was introduced by Snel *et al.* [1]. Further, they proposed a semi–empirical correction of the 2–D lift curve, identifying the local chord to radius ratio (c/r) of the blade section as the main parameter. This result has been confirmed by Shen and Sørensen [13] and by Chaviaropoulos and Hansen [14], who performed airfoil computations applying a quasi 3–D assumption of the Navier–Stokes equations. Du and Selig [15] approached the problem by solving the 3–D incompressible steady boundary layer equations. Their analysis stated that the stall delay mainly depends on the acceleration of the boundary layer, *i.e.* on the Coriolis forces. Full 3-D Navier-Stokes solutions have been carried out by N.N. Sørensen et al. [16] who successfully compared RANS computations with measurements from the NREL experiment.

Besides the corrections by Snel *et al.* [1] and Chaviaropoulos and Hansen [14], 3–D corrections of 2–D airfoils characteristics have been made by Lindenburg [18], taking the local tip speed ratio into account and introducing a drag force correction, and by Bak *et al.* [19], using the different pressure distributions of rotating and non-rotating airfoils. In both cases the corrections were compared with experimental data.

4.2 Mathematical and Numerical Modelling

In the present work the CFD code Fluent has been utilized for computing the viscous incompressible 3–D flow field around a rotating blade, considering a non–inertial reference system moving with the rotor. 3–D and 2–D turbulent flow simulations were performed, with different angles of attack. The rotational speed is constant for all the computations. A constant–chord, non–twisted and zero–pitched blade was used and a non–uniform incoming flow was considered (see Figure 34). The geometric angle of attack is kept constant along the span by specifying the axial flow component as $(\Omega z)/V(z) = const$, where z is the radial coordinate and Ω the rotational speed. The idea is to build a database of different flow conditions, varying angle of attack, Reynolds number and radial position. In order to analyse the output data, an ad-hoc post-processing tool has been developed to eveluate the dominant terms in the boundary layer equations.
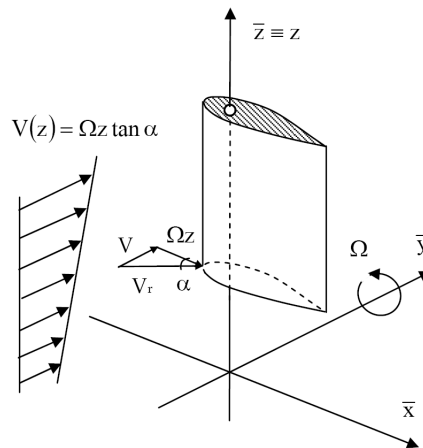
Figure 34. Incoming wind velocity profile.
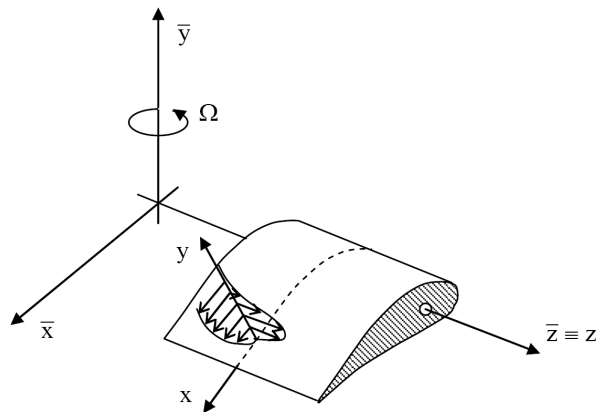
Figure 35. Reference systems of coordinates, global $(\bar{x}, \bar{y}, \bar{z})$ and local (x, y, z).

4.2.1 Mathematical model

Consider a blade section performing a steadily rotating motion, two different reference systems are introduced. One is a global reference system attached to the blade and moving with it. The other one is a local reference system, still fixed with the blade, but aligned point by point with the local tangential and normal directions of the blade surface (see Figure 35). In the first

system the steady incompressible time–averaged Navier–Stokes equations (see *e.g.* [21]) in a rotating frame of reference are written as

$$\nabla \cdot \vec{V}_r = 0 \tag{11}$$

$$\nabla \cdot (\vec{V}_r \vec{V}_r) + 2\vec{\Omega} \times \vec{V}_r + \vec{\Omega} \times \vec{\Omega} \times \vec{r} = -\frac{1}{\rho} \nabla p + \nabla \cdot \bar{\bar{\tau}} \tag{12}$$

where $\vec{V}_r$ is the relative velocity vector, $\vec{\Omega}$ is the the rotational speed, and ρ is the density of the fluid. The stress tensor τ is defined as

$$\bar{\bar{\tau}} = \nu \left(\nabla \vec{V} + \nabla \vec{V}^T \right) \tag{13}$$

where ν defines the viscosity. The Coriolis force is given by the term $2\vec{\Omega} \times \vec{V}_r$ and the centrifugal force by $\vec{\Omega} \times \vec{\Omega} \times \vec{r}$.

The second reference system refers to the boundary layer equations, which will be described later.

4.2.2   Numerical model and mesh topology

A blade with constant chord and constant twist consisting of the NACA0018 airfoil is investigated using the CFD code Fluent.

All the computations have been performed using the finite–volume code Fluent 6.3 with a steady–RANS approach. An untwisted blade, consisting of a symmetric NACA 0018 airfoil with constant chord, has been modelled by applying periodicity corresponding to a three–bladed rotor. The blade geometry was scaled using a constant chord length, $C = 1$ m. The radius is $2\,C$ and $20\,C$ at the root and at the tip of the blade, respectively. A computational domain enclosed by two cylinders has been chosen, with the blade starting at the inner cylinder and ending at the outer cylinder (Figure 36). The full axial extension of the domain is 2 times the rotor diameter and is centred on the blade. These dimensions are the result of a proper balance between computational efforts and boundary independency.

Figure 36. Computational domain (C = chord length).

The grid has been generated modularly with Gambit. It consists of a C–shaped region around the blade (Figure 37) blended with a cylindrical external block, as shown in Figure 38.

The grid consists of about 80 mesh points in the direction normal to the blade, with 35 cells going from the airfoil at a normal distance of approximately half–chord (with a first cell height of 10^{-5} chord length), 120 cells for each side of the profile and 45 cells in the spanwise direction. The boundary layer has been solved directly, with y^+ taking values between 1 and 3. The κ–ω SST turbulence model by Menter was used for turbulent computations. A low-Re correction was implemented to damp the turbulent viscosity as the Reynolds number gets low.

Dirichlet boundary conditions was used for the velocity at the inlet, whereas Neumann conditions was imposed for the pressure at the outlet. The inner and outer cylindrical surfaces
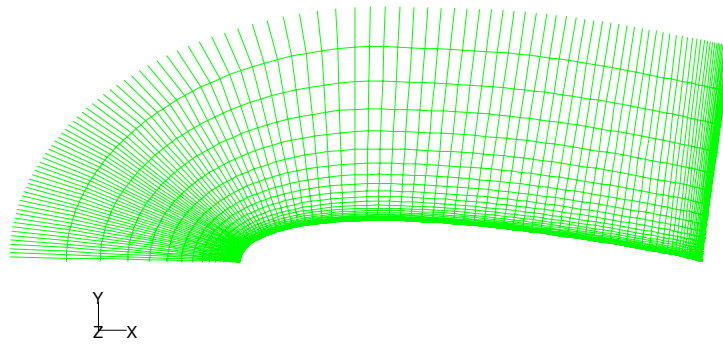
Figure 37. C-mesh around NACA 0018 airfoil (120*x*35)
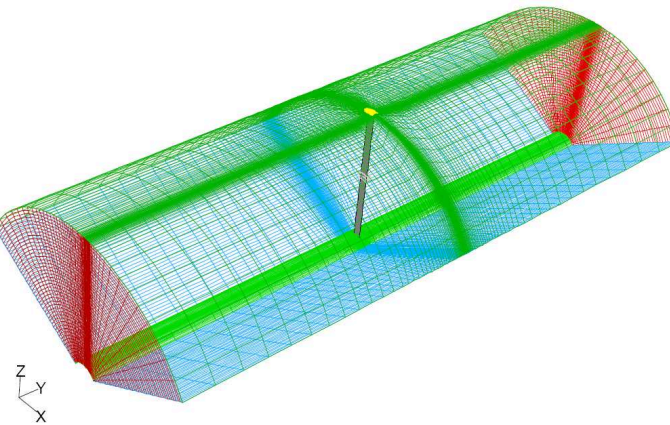
Figure 38. Computational grid $(0.9 \cdot 10^6 \text{ volumes})$

were regarded as Euler–slip walls. In the 3–D case the standard grid consists of about one million mesh points. A refinement study was performed with two millions mesh points. To show differences and analogies the same set-up was used for both 2–D and 3–D computations.

4.2.3   Determination of 3–D angle of attack

Rotational effects can be studied and identified by comparing 3–D rotating blade computations with corresponding 2–D computations. However, the flow conditions in the two cases must be chosen in a consistent manner. In order to compare the various computations, it is required that the actual angle of attack is the same. Angle of attack, however, is a 2–D concept, defined as the geometrical angle between the relative flow direction and the chord of the airfoil. Consequently, finding an equivalent local angle of attack for 3–D flows is not trivial. For a rotating blade the flow passing by a blade section is influenced by the bound circulation on the blade. Moreover, a further complication arises from the 3–D effects from tip and root vortices, which we for the sake of simplicity neglect in our model. To determine the local angle of attack from the computed 3–D flow field two different techniques were considered. The first technique is the averaging technique suggested in [22] and then, slightly modified, employed in [23]. The sec-
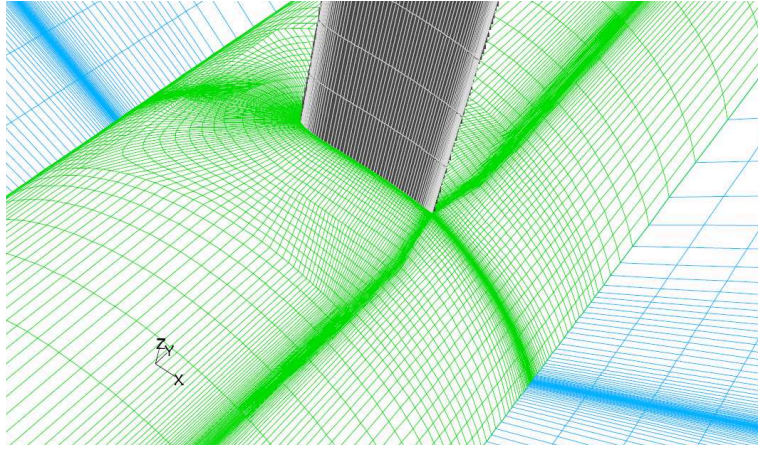
Figure 39. Computational grid, detail of the blade root

ond technique, which was recently proposed by Shen *et al.* [24] as a method suitable for more general flow conditions, is based on the determination of the local induced velocities created by the bound vortices. After verifying the agreement between output from the two strategies, the latter was finally chosen for all further investigations.

4.2.4   The boundary layer equations and postprocessing

In order to analyse the output data from the N–S computations, an analysis code has been developed in Matlab to evaluate the relative importance of the various terms in the boundary layer equations with respect to rotational effects.

Based on the CFD computations the different terms in the equations are postprocessed and evaluated to find their significance.

The 3–D incompressible boundary layer equations for a steady rotating flow, based on Prandtl's boundary layer equations (see [20]), read

$$\frac{\partial u}{\partial x} + \frac{\partial v}{\partial y} + \frac{\partial w}{\partial z} = 0 \tag{14}$$

$$u\frac{\partial u}{\partial x} + v\frac{\partial u}{\partial y} + w\frac{\partial u}{\partial z} = -\frac{1}{\rho}\frac{\partial p}{\partial x} + 2\Omega w\cos\theta + \Omega^2\bar{x}\cos\theta + \frac{\partial}{\partial y}\left(\nu\frac{\partial u}{\partial y} - \overline{u'v'}\right) \tag{15}$$

$$u\frac{\partial w}{\partial x} + v\frac{\partial w}{\partial y} + w\frac{\partial w}{\partial z} = -\frac{1}{\rho}\frac{\partial p}{\partial z} + 2\Omega u\cos\theta + \Omega^2\bar{z} + \frac{\partial}{\partial y}\left(\nu\frac{\partial w}{\partial y} - \overline{v'w'}\right) \tag{16}$$

where (u,v,w) are the velocity components in directions (x,y,z), *i.e.* the axes of the local system of coordinates, with θ defining the angle between the tangent to the airfoil and the $x-z$ plane.

The desired output variables are computed in some proper surfaces of constant radius, extended to a distance of a half chord length from the blade surface (Figure 40). The variables of interest are sorted in a new order, according to the boundary layer tangential and normal directions (see the local system of coordinates in Figure 35 and Figure 41).

The derivatives are estimated using 2nd order CDS polynomial fitting of the output data for non–uniform spaced grids.

The boundary layer thickness is determined by checking either the vorticity magnitude or the velocity gradient along the normal direction. The last technique was suggested by Stock and Haase [25].

Figure 40. Postprocessing sections of the computational domain
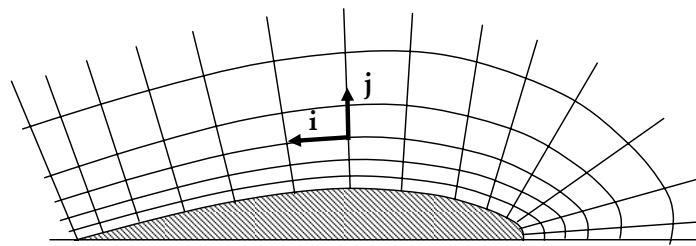
Figure 41. Grid around the airfoil and new nodes indices

4.3 Results

We here present the outcome of the simulations, focusing on general features in the flow field around rotating blades and the effects of rotation on pressure coefficient distributions and integral boundary layer characteristics. A number of different flow conditions have been simulated and analysed, with geometric angles of attack ranging from 0 to 16 degrees. The effective values of the local angle of attack, however, may exceed 20 degrees at inboard locations, and a large portion of the blade is dominated by separation phenomena (see Figure 42). As expected, in the attached part of the blade, the limiting pathlines are aligned with the main stream direction, so that they can be regarded as in a 2D-alike condition. This is true mainly for the outboard part of the blade, whose behaviour resembles that of an ideal wing of infinite span. On the other hand, where separation dominates, the flow pattern shows evidence of strong radial flow components in the inboard part of the blade.

In the turbulent flow computations the Reynolds number along the blade varies between $1 \cdot 10^6$ and $6 \cdot 10^6$ from root to tip. The radial stations chosen for the analysis are located at $r/R = 0.16$, 0.54 and 0.75. A pure rotating blade, without inflow and with zero pitch angle, is presented as a reference case for a laminar flow regime. The laminar velocity profiles, shown in Figure 43, look physically correct and the crossflow is seen to dominate after separation, which in this case occurs at a position of about 80% of the chord length.

In Figure 44 in–plane streamlines around a rotating blade section and the corresponding 2–D airfoil are compared in a situation of deep stall. It is clearly seen that rotation stabilizes vortex shedding and limits the growth of the separated region. Moreover, the stagnation point moves
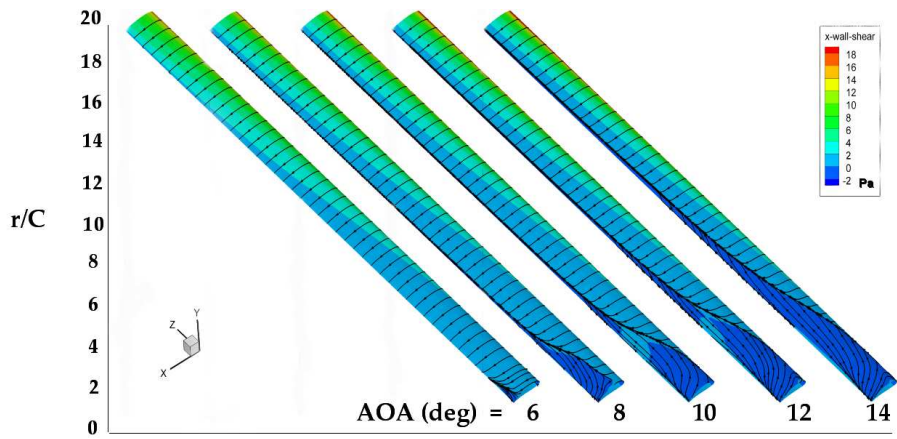
Figure 42. Limiting streamlines on blade suction side for different geometric flow incidences.
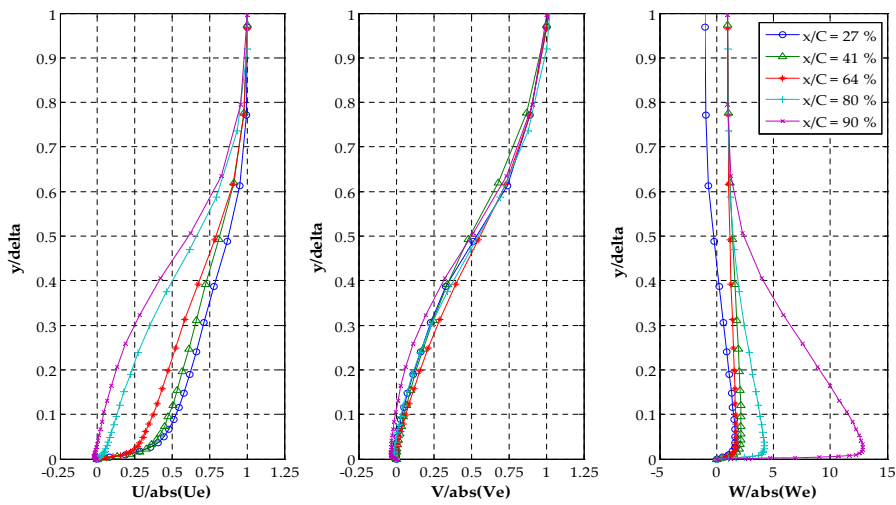
Figure 43. Velocity profiles in the local coordinate system for different chordwise positions x/C, plotted against the non-dimensional boundary layer thickness y/δ and non-dimensionalised with the values at boundary layer edge (3–D, $r/R = 0.16$, AOA = 13.4 deg, Re = 10^2)

The computations revealed differences in e.g. velocity profiles at different chordwise stations and differences in separated areas.

downstream, and separation tends to approach the leading edge.
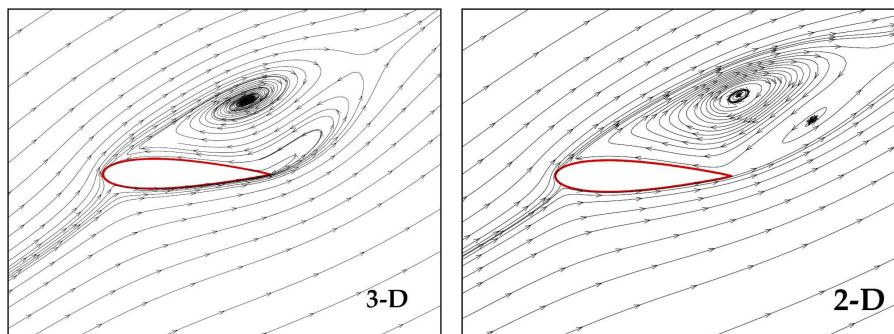
Figure 44. Streamlines around the 3–D rotating blade section at $r/R = 0.16$ and the corresponding 2–D case with local incidence of 26.9 degrees and Reynolds number about 10^6

This is confirmed by Figure 45, where 2–D and 3–D pressure coefficients are compared. It is seen that the pressure at the suction side is less flat in the 3–D case, which then modifies the

overall distribution of the pressure on both the pressure and the suction side of the airfoil.

r/R = 16%; AOA = 26.9 deg; Re = 1.1·10^6
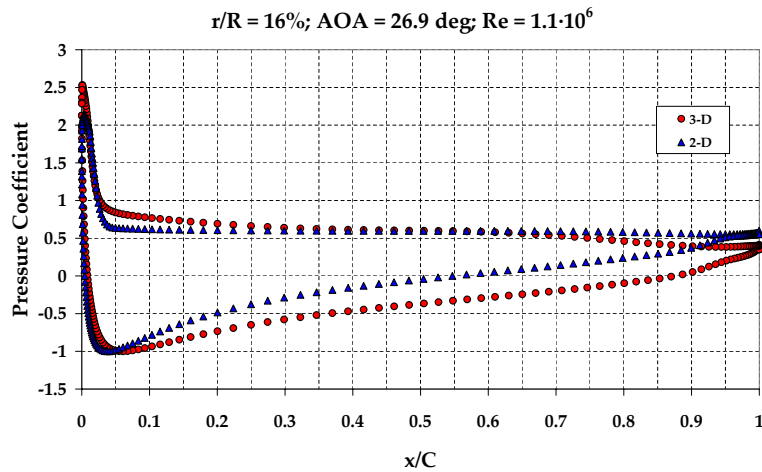
Figure 45. Pressure coefficient distribution of the 3–D rotating blade section at r/R = 0.16 compared to the 2–D case (angle of attack = 26.9 degrees, Reynolds number = 10^6)

Isoplots of static pressure and vorticity are shown in Figure 46 and Figure 47, respectively. Different radially spaced slices of the domain around the blade are considered. These planes are curved surfaces of constant radius (the value is indicated on the labels) covering a normal distance of 1 chord all around the blade surface. The same colormap has been used for all sections. Since the pressure scales with radius the pressure is most pronounced at larger distances from the rotational axis. The outward sections operate at lower angles of attack, leading to attached flow with lift coefficients resembling the 2D ones.
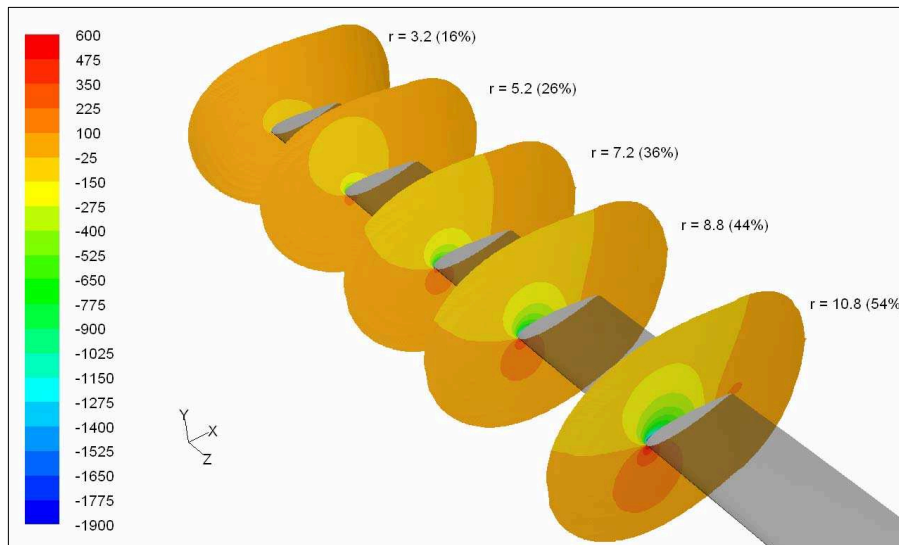
Figure 46. Contours of static pressure p [Pa], radial slices along the cylindrical blade, (U=10 m/s)

The vorticity field is depicted in Figure 47. The blue colour that fills almost entirely each slice is the potential field past the blade, where vorticity is zero. The boundary layer is clearly visible as a thin red-oriented belt around the airfoil sections. The boundary layer, gets thicker and thicker while approaching the trailing edge. This is most evident at the suction side, where strong adverse pressure gradients exist. However, the slices provide a vivid description of the different behaviour an airfoil boundary layer flow can experience. The most outboard section

shows an almost symmetric behaviour on the two sides of the airfoil, the angle of attack is small and no separation is seen, so that the two boundary layers leave smoothly the trailing edge and combines into a common wake structure. Going inward the flow incidences increase, trailing edge separation occurs on the suction side. At a certain point two separation bubbles occur, one located just after the leading edge and the other at trailing edge. In between the separation bubbles the flow is dominated by complex and unsteady flow structures (see also Figure 44).
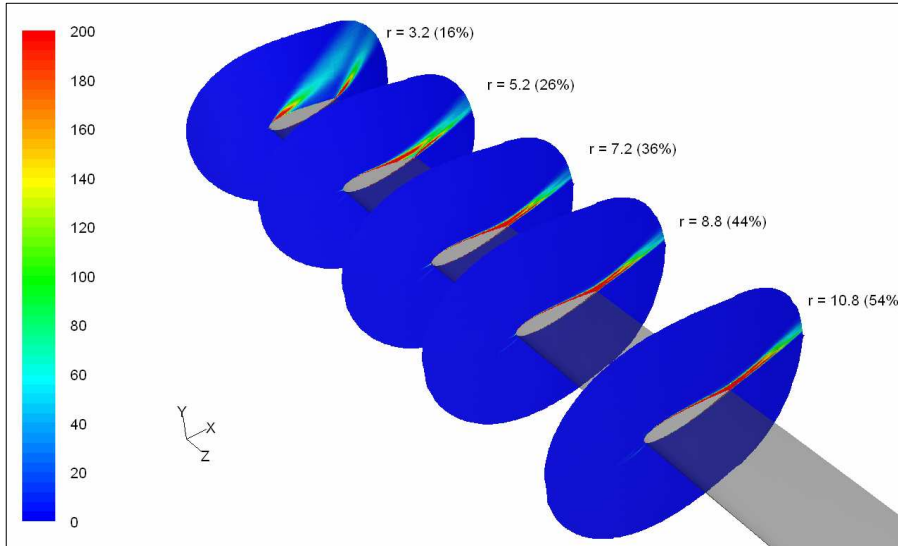
Figure 47. Contours of vorticity magnitude ξ [1/s], radial slices along the cylindrical blade, (U=10m/s)

As an example of the post-processing output, the magnitude of the Coriolis and spanwise–convection terms in the governing equations have been evaluated. The outcome is shown in Figure 48, which depicts the crossflow (r_1) and Coriolis (r_2) terms, computed from the following equations

$$r_1 = Log\left(\frac{\left|w\frac{\partial u}{\partial z}\right|}{\left|u\frac{\partial u}{\partial x}\right| + \left|v\frac{\partial u}{\partial y}\right|}\right) \tag{17}$$

$$r_2 = Log\left(\frac{2\Omega w \cos\theta}{\left|u\frac{\partial u}{\partial x}\right| + \left|v\frac{\partial u}{\partial y}\right|}\right) \tag{18}$$

The computations were postprocessed to investigate e.g. the crossflow term and the Coriolis term.

When separation occurs both terms increase, with the Coriolis term exhibiting the highest values. The figures are shown at two different positions, implying that the effective angle of attack and the Reynolds number are different for the two sections. Since the blade is rotating, different local angles of attack are seen by the blade sections. The area depicted in Figure 48 is a close up of the boundary layer region with the local normal-to-wall coordinate scaled to fit the computed boundary layer thickness. The very first part of the airfoil section has not been considered, since the boundary layer is still rather thin and the processed data are influenced by curvature effects at the leading edge. A more comprehensive analysis on the boundary layer integral properties is still in progress to determine more precisely the most important effect of rotation.

An important result of the analysis is the evaluation of the aerodynamic coefficients shown in Figure 49. It is clearly seen that the lift coefficient is increased when the blade is subject to rotation, and that this effect is most pronounced near the axis of rotation. On the other, the enhanced lift is associated with higher values of the drag coefficient. The results have been

• $r/R = 0.26\,(c/r \cong 0.2) - Re = 1.6 \cdot 10^6 - AOA = 15.2°$
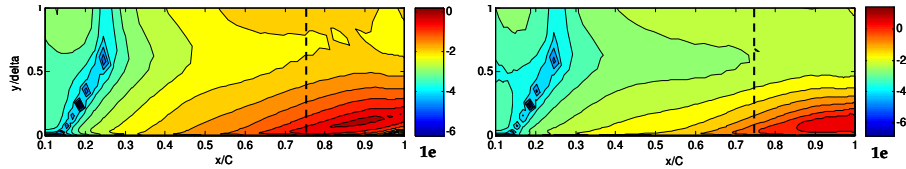
• $r/R = 0.54\,(c/r \cong 0.1) - Re = 3.0 \cdot 10^6 - AOA = 10.5°$
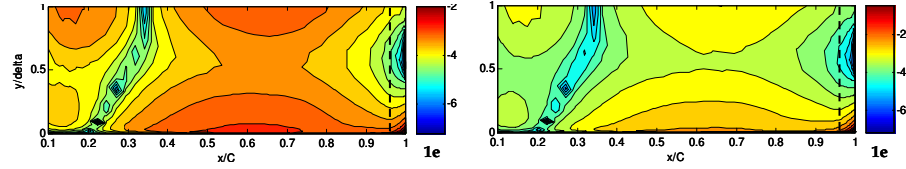
*Figure 48. Relative magnitude of crossflow derivative (*left*) and Coriolis term (*right*) in the boundary layer x-momentum equations, in logarithmic scale. Separation is marked with a black dashed line.*

compared with a pure 2–D airfoil, showing that 3–D values are higher for the whole range of flow angles. However, the 3–D rotating results also differ from the reference at lower angles of attack and attached flow conditions. A likely explanation is that the 2–D section is isolated, while the real flow is the result from a three-bladed rotor subject to cascade effects and at inbord sections the inviscid flow is dominated by strong adverse curvature effects. Moreover, despite the magnitude of the domain, boundary conditions could play a role in influencing the flow field. In fact the wind turbine has been modelled as a sort of ducted machine, rather than an open–flow rotor. This problem, however, can be resolved by using the outboard section (e.g. $r/R = 0.76$) as a reference to the 2–D case.

To check the results, further comparison was carried out by comparing 3–D computations with the semi-empirical 3–D correction of Snel *et al.* [1]. The correction, that basically depends on the square of the ratio of local chord and spanwise position, was employed to correct the 2–D data at a radial position of r/R=16%. Under the same inflow conditions (AOA, Re), 2–D computer simulations were run for a NACA 0018 airfoil. Applying the Snel *et al.* correction to the resulting 2–D lift distribution resulted in the plot shown in Figure 50. Here, the dashed line represents the linear trend of the first part of the 2–D curve. From the figure it is seen that the computed 3–D results in the linear region is higher than the coresponding 2–D case. The corrected lift coefficient is seen to be located in between the pure 2–D and the 3–D results. At high angles of attack (22 degrees), however, the corrected and computed 3–D results are almost identical.
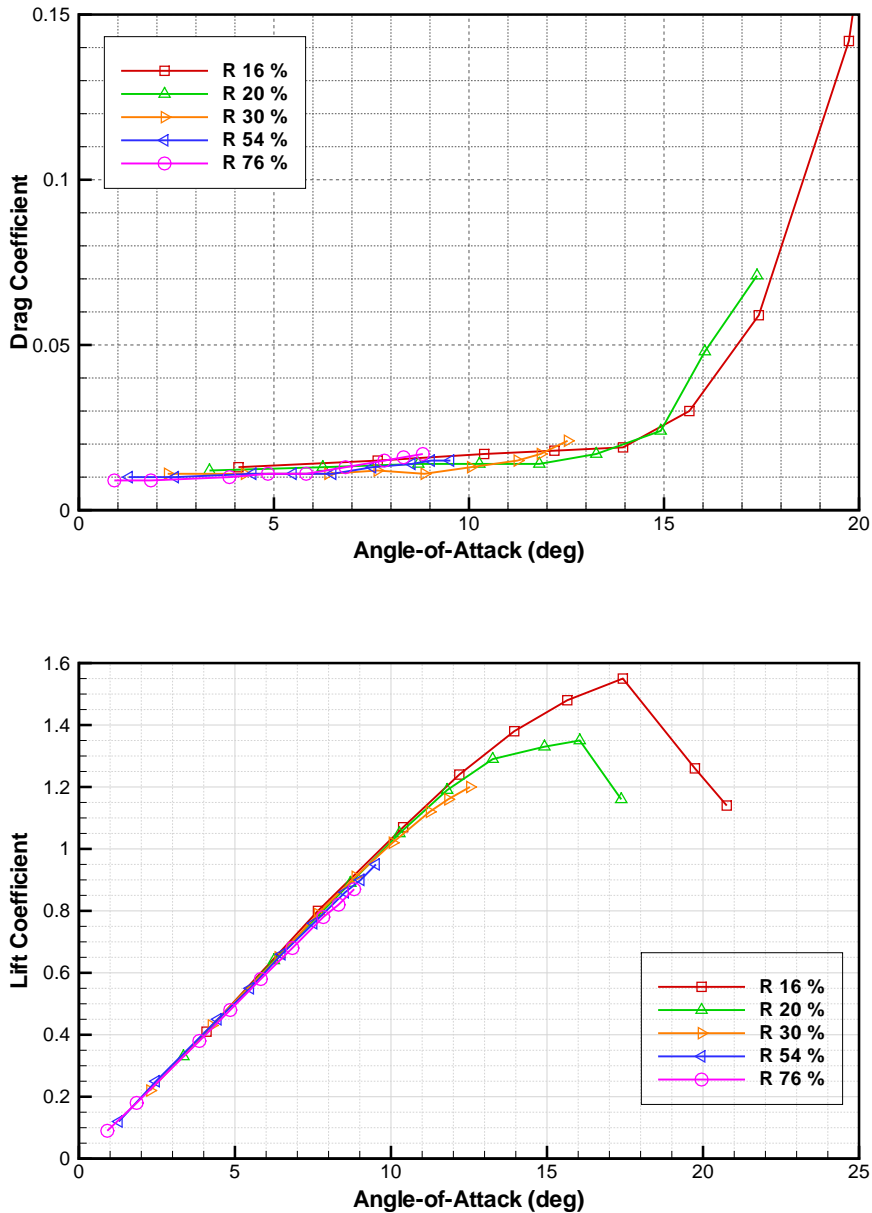
Figure 49. Drag and lift coefficients for the 3–D rotating blade sections at r/R = 0.16, 0.56 and 0.76 and the corresponding 2–D case. In the x-axis is the effective angle of attack

4.4   Concluding remarks

Present design approaches for wind turbines are typically based on employing the blade–element momentum (BEM) theory, with lift and drag forces determined from 2–D measurements. Although CFD is not a practical design tool, useful suggestions for classical design codes can be derived, based on a quantitative explanation of rotational phenomena. The aim of the present work is to derive the basic tools for studying the influence of rotational effects on rotating blades and utilize the results from the study in BEM codes.

In the present work CFD–RANS computations were carried out to solve the flow field past a rotating blade and to quantify the impact of rotational effects in the boundary layer.

A post-processing tool for studying the local velocity profiles and for evaluating the relative importance of rotational terms in the boundary layer equations were developed and implemented.
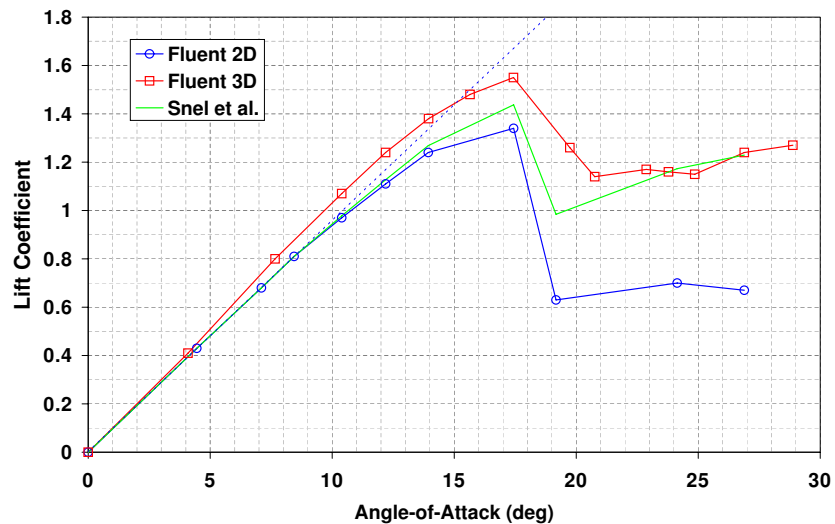
Figure 50. 2D and rotating 3D predicted C_L compared to the Snel et al. correction method output for the r/R=16% section, Re $= 10^6$

The tools are used to determine integral properties of boundary layers in order to derive practical 'empirical' corrections for use in the design. Early results for a simple blade geometry have been presented, confirming that the loads on a rotating blade are higher than those appearing on a corresponding non-rotating case, and that this is most pronounced at inboard sections and under separated flow conditions.

The work is still in progress and it is expected that the results from the Navier-Stokes computations can be used both to correct 2–D airfoil characteristics and to derive integral boundary layer solvers aimed specifically for rotating blades.

References

[1] Snel H, Houwink R, Bosschers J, Piers W J, van Bussel G J W and Bruining A 1993 Sectional prediction of 3-D effects for stalled flow on rotating blades and comparison with measurements *Proc. of EWEC* 395–9

[2] Harris F D 1966 Preliminary study of radial flow effects on rotor blades *J. of the American Helicopter Society* **11**(3) 1–21

[3] Himmelskamp H 1945 *Profile investigation on a rotating airscrew* (Göttingen: PhD Dissertation)

[4] Ronsten G 1992 Static pressure measurements on a rotating and non-rotating 2.375 m wind turbine blade. Comparison with 2D calculations *J. Wind Engineering and Industrial Aerodynamics* **39**(1-3) 105–18

[5] Tangler J L and Kocurek J D 2005 Wind turbine post-stall airfoil performance characteristics guidelines for Blade-Element Momentum methods *Proc. of 43rd AIAA Aerospace Sciences Meeting and Exhibit* (591) 1–10

[6] Schreck S 2002 The NREL full-scale experiment *Wind Energy* **5** 77–84

[7] Sears W R 1950 Potential flow around a rotating cylindrical blade *J. Aeronautical Sciences* (Readers' Forum) **17**(3) 183

[8] Fogarty L E and Sears W R 1950 Potential flow around a rotating, advancing cylinder blade *J. Aeronautical Sciences* (Readers' Forum) **17**(9) 599

[9] Fogarty L E 1951 The laminar boundary layer on a rotating blade *J. Aeronautical Sciences* **18**(4) 247

[10] Banks W H H and Gadd G E 1963 Delaying effects of rotation on laminar separation *AIAA Journal* **1**(4) 941–2

[11] McCroskey W J and Dwyer H A 1969 *Methods of analyzing propeller and rotor boundary layers with crossflows* NASA SP-228 473–514

[12] Sørensen J N 1986 Prediction of the three-dimensional stall on wind turbine blade using three-level, viscous-inviscid interaction model *Proc. of EWEC* 429–35

[13] Shen W Z and Sørensen J N 1999 Quasi-3D Navier-Stokes model for a rotating airfoil *J. of Computational Physics* **150** 518–48

[14] Chaviaropoulos P K and Hansen M O L 2000 Three-dimensional and rotational effects on wind turbine blades by means of a Quasi-3D Navier-Stokes solver *J. of Fluid Engineering* **122** 330-6

[15] Du Z and Selig M S 2000 The effect of rotation on the boundary layer of a wind turbine blade *Renewable Energy* **20** 167–81

[16] Sorensen NN, Micelsen JA and Schreck S 2002 Navier-Stokes predictions of the NREL Phase VI rotor in the NASA Ames 80 ft x 120 feet wind tunnel*Wind Energy* **5** 151–169

[17] Hu D, Hua O and Du Z 2006 A Study on stall-delay for horizontal axis wind turbine *Renewable Energy* **31** 821–36

[18] Lindenburg C 2004 Modelling of rotational augmentation based on engineering considerations and measurements *Proc. of EWEC*

[19] Bak C, Johansen J and Andersen P B 2006 Three-dimensional corrections of airfoil charcteristics based on pressure distributions *Proc. of EWEC*

[20] Schlichting H 1955 *Boundary layer theory* (New York: McGraw-Hill) 120–1

[21] Batchelor G K 1967 *An Introduction to Fluid Dynamics* (Cambridge University Press) 139–40

[22] Hansen M O L, Sørensen N N, Sørensen J N and Michelsen J A 1997 Extraction of lift, drag and angle of attack from computed 3-D viscous flow around a rotating blade *Proc. of EWEC* 499–502

[23] Johansen J and Sørensen N N 2004 Airfoil characteristics from 3D CFD rotor computations *Wind Energy* **7** 283–94

[24] Shen W Z, Hansen M O L and Sørensen J N 2006 Determination of Angle of Attack (AOA) for rotating blades *Proc. of Euromech Colloquium (Wind Energy)* 205–9

[25] Stock H W and Haase W 1999 Feasibility study of e^N transition prediction in Navier-Stokes methods for airfoils *AIAA Journal* **37**(10) 1187–96

5 Laminar turbulent transition using the $\gamma - \mathrm{Re}_\theta$ transition model

Author: Niels N Sørensen

When predicting the flow over airfoils and rotors, the laminar-turbulent transition process can be important for the aerodynamic performance. Today, the most widespread approach is to use fully turbulent computations, where the transitional process is ignored and the entire boundary layer on the wings or airfoils is handled by the turbulence model. The main reason for neglecting laminar/turbulent transition in rotor aerodynamics, is the dependence of most transition prediction methods on boundary layer quantities which makes them difficult to interface to modern parallelized multiblock general purpose flow solver. To compute the boundary layer quantities on a general 3D object, one needs to determine the stagnation point location, and track the boundary layer development along the local flow direction close to the surface. Additionally, one will need to transverse the boundary layer station in a direction normal to the wall surface. Neither the tracking of the local flow direction nor the normal direction, are guaranteed to follow local grid directions and may additionally cross the block interfaces, which makes the logistics of such a method very cumbersome. One implementation of such a method, based on the e^n method was implemented in 2D [1], which has proven to be very accurate and reasonably robust. In the same reference, work was ongoing to implement a similar method for 3D, work that was unfortunately never finished. As an alternative approach the correlation based transition model has lately shown promising results, and the present chapter describes the effort of deriving the two non-public empirical correlations of the model, as well as a series of applications to rotor and airfoil flows of interest to wind turbines. The main advantage of the model is the fact that it avoids the need to track the boundary layer flow and evaluate the boundary layer quantities at each boundary layer station. This is achieved by the use of two transport equations one for intermittency and one for the transition onset moment thickness Reynolds number.

A new correlation based 3D transition model is implemented

5.1 Nomenclature

dU/ds Acceleration along a streamline

k Turbulent kinetic energy

K Flow acceleration parameter $(\nu/U^2)dU/ds$

Re_x Reynolds number based on length, $\rho x U_{ref}/\mu$

Re_θ Momentum thickness Reynolds number,
$\rho\theta U_0/\mu$

$\text{Re}_{\theta c}$ Critical momentum thickness Reynolds
number

$\text{Re}_{\theta t}$ Transition onset momentum thickness
Reynolds number, $\rho\theta_t U_0/\mu$

$\widetilde{\text{Re}}_{\theta t}$ Local transition onset momentum
thickness Reynolds number,
obtained from transport equation

R_T Viscosity Ratio $\rho k/(\mu\omega)$

Re_ν Vorticity (Strain rate) Reynolds
number $\rho y^2 S/\mu$

S Absolute value of the strain rate, $(2S_{ij}S_{ij})^{\frac{1}{2}}$

S_{ij} Strain rate tensor, $\frac{1}{2}(\partial u_i/\partial x_j + \partial u_j/\partial xi)$

Tu Turbulence intensity $100(2k/3)^{\frac{1}{2}}/U$

U Local velocity $(u^2 + v^2 + w^2)^{\frac{1}{2}}$

U_o Local free stream velocity, outside of
boundary layer

U_{ref} Inlet reference velocity

y Distance to nearest wall

y^+ Distance in wall coordinats, $y u_\tau/\mu$

δ Boundary layer thickness

ε Turbulent dissipation rate

θ Momentum thickness

λ_θ Non-dimensional pressure gradient, $\frac{\rho\theta^2}{\mu}\frac{dU}{ds}$

μ Molecular viscosity

μ_t Eddy viscosity

u_τ Friction velocity $\sqrt{(\tau/\rho)}$

ρ Density

τ Wall shear stress

Ω Absolute value of vorticity $(2\Omega_{ij}\Omega_{ij})^{\frac{1}{2}}$

Ω_{ij} Vorticity tensor, $\frac{1}{2}(\partial u_i/\partial x_j - \partial u_j/\partial x_i)$

ω Specific turbulence dissipation rate

5.2 Introduction

The chapter describes the implementation of a new empirical correlation based transition model in the EllipSys code. A series of parametric computations are performed to determine the two non-public empiric relations needed to make the model complete; one relation for the Critical Momentum Thickness Reynolds Number; and one for the Transition Length Factor. This is done as described in the original work of Menter et. al. [2, 3] using flat plate boundary layers and the resulting expressions are given in the present paper. Other authors have proposed alternative correlations [4, 5], which for unknown reason do not agree with the present correlations.

Following the initial tuning of the model for flat plates, a series of typical wind turbine airfoils are computed comparing the present version of the correlations based transition model with an existing transition model featuring an e^n method, a by-pass model and a model for separation induced transition [1] and experimental data. Generally, the airfoil computations show good

agreement with both the existing e^n method and experimentally determined drag and transition point location. Additionally, it is shown that the model is capable of capturing both natural, by-pass and separation induced transition. Following the initial 2D tests, the model is applied to the case of flow around a three-dimensional prolate spheroid of Kreplin et. al. [6], to illustrate that the model is capable of predicting the correct transition location for the zero angle of attack cases. Finally, the NREL-Phase-VI [7–9] turbine is used as a test case to verify the applicability of the model to wind turbine rotor aerodynamics.

5.3 Flow solver

The in-house flow solver EllipSys3D is used in all computations presented in the following. The code is developed in co-operation between the Department of Mechanical Engineering at the Technical University of Denmark and The Department of Wind Energy at Risø National Laboratory (now Risø-DTU), see [10, 11],[12]. The EllipSys3D code is a multiblock finite volume discretization of the incompressible Reynolds-Averaged Navier-Stokes (RANS) equations in general curvilinear coordinates. The code uses a collocated variable arrangement, and Rhie/Chow interpolation [13] is used to avoid odd/even pressure decoupling. As the code solves the incompressible flow equations, no equation of state exists for the pressure, and in the present work the SIMPLE algorithm of Patankar and Spalding [14, 15] or the PISO algorithm of Issa [16, 17] is used to enforce the pressure/velocity coupling, for steady state and transient computations respectively. The EllipSys3D code is parallelized with MPI for executions on distributed memory machines, using a non-overlapping domain decomposition technique. Both steady state and unsteady computations can be performed. For the unsteady computations the solution is advanced in time using a 2nd order iterative time-stepping (or dual time-stepping) method. In each global time-step the equations are solved in an iterative manner, using under relaxation. First, the momentum equations are used as a predictor to advance the solution in time. At this point in the computation the flowfield will not fulfil the continuity equation. The rewritten continuity equation (the so-called pressure-correction equation) is used as a corrector making the predicted flowfield satisfy the continuity constraint. This two step procedure corresponds to a single sub-iteration, and the process is repeated until a convergent solution is obtained for the time step. When a convergent solution is obtained, the variables are updated, and we continue with the next timestep. For steady state computations, the global time step is set to infinity and dual time stepping is not used, this corresponds to the use of local time stepping. In order to accelerate the overall algorithm, a multi-level grid sequence is used in the steady state computations. The convective terms are discretized using a third order QUICK upwind scheme, implemented using the deferred correction approach first suggested by Khosla and Rubin [18] and applied along with a MinMod limiter to obtain TVD behavior. Central differences are used for the viscous terms, in each sub-iteration only the normal terms are treated fully implicitly, while the terms from non-orthogonality and the variable viscosity terms are treated explicitly. Thus, when the sub-iteration process is finished all terms are evaluated at the new time level. In the present work the turbulence in the boundary layer is modeled by the k-ω SST eddy viscosity model [19]. The equations for the turbulence model and the transition model are solved after the momentum and pressure-correction equations in every sub-iteration/pseudo time step, and in agreement with the recommendations of Menter et al. [2], a second order upwind TVD scheme is used for the transport equations for turbulence and transition. The three momentum equations, the $k - \omega$ equations and the two transition model equations are solved decoupled using a red/black Gauss-Seidel point solver. The solution of the Poisson system arising from the pressure-correction equation is accelerated using a multigrid method. In order to accelerate the overall algorithm, a multi-level grid sequence and local time stepping are used. For the rotor computations with uniform inflow a steady state moving mesh approach is used [20]. The moving mesh option has been implemented in the EllipSys3D solver in a generalized way allowing arbitrary deformation of the computational mesh, following [21].

The EllipSys3D Navier-Stokes solver is used for the present study

5.4 Transition Model

The $\gamma - \widetilde{\mathrm{Re}}_\theta$ correlation based transition model of [2], is a framework for implementing empirical correlation based transition criterions in general purpose flow solvers, that can be used together with structured, unstructured and parallelized solvers. The backbone of the model is two transport equations one for intermittency γ and one for the local transition onset momentum thickness Reynolds number $\widetilde{\mathrm{Re}}_{\theta t}$. Basically, the model relates the local momentum thickness Reynolds number Re_θ evaluated by Eqn. 19 to the critical value $\mathrm{Re}_{\theta c}$, and switches on the intermittency production when Re_θ is larger than the local critical value.

The model is based on a simple relation between Reynolds numbers and transition onset

$$\mathrm{Re}_\theta = \frac{\mathrm{Re}_{v,\max}}{2.193} \ . \tag{19}$$

The transport equation for the intermittency is given by:

$$\frac{\partial(\rho\gamma)}{\partial t} + \frac{\partial(\rho U_j \gamma)}{\partial x_j} = P_\gamma - E_\gamma + \frac{\partial}{\partial x_j}\left[\left(\mu + \frac{\mu_t}{\sigma_f}\right)\frac{\partial\gamma}{\partial x_j}\right] \ .$$

Where the production and destruction terms can be computed from the relations given below:

$$P_\gamma = F_{length}c_{a1}\rho S(\gamma F_{onset})^{0.5}(1-\gamma) \ .$$

$$E_\gamma = c_{a2}\rho\Omega\gamma F_{turb}(c_{e2}\gamma - 1) \ .$$

$$F_{onset1} = \frac{\mathrm{Re}_v}{2.193\mathrm{Re}_{\theta c}} \ .$$

$$\mathrm{Re}_v = \frac{\rho y^2 S}{\mu} \ ; \ R_T = \frac{\rho k}{\mu\omega} \ ; \ F_{turb} = e^{-(\frac{R_T}{4})^4} \ .$$

$$F_{onset2} = \min(\max(F_{onset1},F_{onset1}^4),2) \ .$$

$$F_{onset3} = \max\left(1 - \left(\frac{R_T}{2.5}\right)^3,0\right) \ .$$

$$F_{onset} = \max(F_{onset2} - F_{onset3},0) \ . \tag{20}$$

$\mathrm{Re}_{\theta c}$ and F_{length} are both functions of $\widetilde{\mathrm{Re}}_{\theta t}$, and are not given in the original reference due to proprietary reasons. The empirical relations for these will be determined later in the present paper. Additionally, the model is very simple to use in connection with forced transition, as we can artificially force F_{onset} to assume the maximum of the computed value from Eqn. 20 and a function set to one downstream of the forced transition point.

The model consist of two partial differential equations

The transport equation for the transition onset momentum thickness Reynolds number $\widetilde{\mathrm{Re}}_{\theta t}$ is given by:

$$\frac{\partial(\rho\widetilde{\mathrm{Re}}_{\theta t})}{\partial t} + \frac{\partial(\rho U_j\widetilde{\mathrm{Re}}_{\theta t})}{\partial x_j} = P_{\theta t} + \frac{\partial}{\partial x_j}\left[\sigma_{\theta t}(\mu + \mu_t)\frac{\partial\widetilde{\mathrm{Re}}_{\theta t}}{\partial x_j}\right] \ .$$

Where the production term can be computed from the relations below:

$$P_{\theta t} = c_{\theta t} \frac{\rho}{t} (Re_{\theta t} - \widetilde{Re_{\theta t}})(1.0 - F_{\theta t}) .$$

$$t = \frac{500\mu}{\rho U^2} .$$

$$F_{\theta t} = \min\left(\max\left(F_{wake} e^{-\left(\frac{y}{\delta}\right)^4}, 1.0 - \left(\frac{\gamma - 1/c_{e2}}{1.0 - 1/c_{e2}} \right)^2 \right), 1.0 \right) .$$

$$\theta_{BL} = \frac{\widetilde{Re_{\theta t}}\mu}{\rho U} , \delta_{BL} = \frac{15}{2}\theta_{BL} , \delta = \frac{50\Omega y}{U}\delta_{BL} , Re_\omega = \frac{\rho\omega y^2}{\mu} .$$

$$F_{wake} = e^{-\left(\frac{Re_\omega}{1\times10^5}\right)^2} .$$

The following constants are used in the model:

$$c_{a1} = 1 , c_{a2} = 0.03 , c_{e2} = 50 , \sigma_f = 1.0 , c_{\theta t} = 0.03 , \sigma_{\theta t} = 2.0 .$$

Additionally, the correction to handle separation induced transition according to [2, 3, 22] is also implemented:

$$\gamma_{sep} = \min\left(s_1 \max\left[0, \left(\frac{Re_v}{3.235 Re_{\theta c}} \right) - 1 \right] F_{reattach}, 2 \right) F_{\theta t} ,$$

where:

$$F_{reattach} = e^{-\left(\frac{R_T}{20}\right)^4} , \text{ and } s_1 = 2 .$$

$$\gamma_{eff} = \max(\gamma, \gamma_{sep}) . \tag{21}$$

The empirical correlation needed for the critical transition onset momentum thickness Reynolds number $Re_{\theta t}$ is given by the following relation from [2]:

$$Re_{\theta t} = 803.73 \left[Tu + 0.6067\right]^{-1.027} F(\lambda_\theta, K) , \tag{22}$$

where:

$$F(\lambda_\theta, K) = 1 - [-10.32\lambda_\theta - 89.47\lambda_\theta^2 - 265.51\lambda_\theta^3] e^{\frac{-Tu}{3.0}} , \text{ if } \lambda_\theta \leq 0 ,$$

$$F(\lambda_\theta, K) = 1 + [0.0962\widetilde{K} + 0.148\widetilde{K}^2 + 0.0141\widetilde{K}^3]$$
$$(1 - e^{\frac{-TU}{1.5}}) + 0.556\left[1 - e^{-23.9\lambda_\theta}\right] e^{\frac{-Tu}{1.5}} , \text{ if } \lambda_\theta > 0 ,$$

where $\widetilde{K} = K \cdot 10^6$, and the following constraints are used for numerical robustness:

$$-0.1 \leq \quad \lambda_\theta \quad \leq 0.1 \, , \tag{23}$$

$$-3 \times 10^{-6} \leq \quad K \quad \leq 3 \times 10^{-6} \, , \tag{24}$$

$$\mathrm{Re}_{\theta t} \quad \geq 20 \, . \tag{25}$$

At farfield boundaries γ is equal to one, while the boundary condition at the wall is zero flux. The farfield value for the $\widetilde{\mathrm{Re}}_{\theta t}$ is set according to Eqn.22 assuming the pressure gradient parameter λ_θ to be zero, while the wall boundary condition is zero flux.

The transition model is coupled to the $k - \omega$ SST model through the use of the effective Intermittency from Eqn. 21, by modifying the production and dissipation terms in the k-equation as shown below:

$$\tilde{P}_k = \gamma_{eff} P_k \text{ and, } \tilde{D}_k = \min(\max(\gamma_{eff}, 0.1), 1.0) D_k \, ,$$

where P_k and D_k are the production and destruction term from the turbulent kinetic energy equation of the original SST equation. One has to be aware that the F_1 blending function needs to be adjusted in order to be able to treat fully laminar boundary layers, according to [2]. Additionally the limiter used to prevent build up of eddy viscosity in stagnation regions is slightly different from the one originally used, see [23]:

$$P_k = \min(\mu_t S^2, 10 D_k) \, , \text{ compared to the original expression: } P_k = \min(\mu_t S^2, 20 D_k) \, ,$$

and the present author has experienced problems with buildup of turbulence/eddy viscosity in the stagnation regions of airfoils using the original formulation, while the first limiter performs flawlessly.

It is well known that the turbulence will decay from the inlet value, in the case of zero shear where there is no production in the farfield. To control the level of turbulent kinetic energy at the boundary layer edge, the farfield value can be estimated from Eqn. 26, from [23]:

$$k = k_{inlet} (1 + \omega_{inlet} \beta t)^{-\frac{\beta^*}{\beta}} \, , \tag{26}$$

with $\beta = 0.09$, and $\beta^* = 0.0828$.

The t featuring in the above expression is a time scale, equal to the distance from the inlet to the location of the geometry divided by the convective velocity.

5.5 Tuning of empirical relations

The two missing correlations, for $\mathrm{Re}_{\theta c}$ and F_{length} both reported in [2, 3] to be a function of $\mathrm{Re}_{\theta t}$ must be determined before the model can be used. Similar to the original work of [2] the tuning is done for four flat plate boundary layers with zero pressure gradient, namely the T3A, T3A-, T3B [24–26] and Schubauer and Klebanoff [27] cases, see Table (2). Other authors have proposed alternative correlations [4, 5], which do not agree with the present correlations. The present author has not been able to verify the correctness of these correlations in connection with the incompressible EllipSys code. F_{length} in the model is used to control the length of the

transition region. As high values of F_{length} correspond to high intermittency production and thereby shorter transition length as also indicated in Fig. 3.4 in [23], the relation used in [4] where F_{length} is proportional to the transition length seems to be wrong.

As the new transition model is very sensitive to insufficient grid resolution, grid stretching and the differencing scheme it is extremely important to assure that grid independent results are obtained in connection with the calibration of the model. For all four flat plate cases three levels of grid refinement were used to establish that the results were grid independent. The finest grid had 512×128 cells in chordwise and normal direction, with a y^+ below 0.2 on the finest grid level. The grid is a simple stretched Cartesian grid with constant spacing in the flow direction and stretching in the cross-flow direction. The plate starts at the edge of the domain, and a uniform inlet velocity profile is used. Determining the empirical correlations by numerical optimization along with debugging the model, demands a very large amount of computations, and it is the hope that other researcher can confirm the present expressions by implementation in other flow solvers.

The tuning of the model is based on a large amount of parametric runs

Table 2. Summary of inlet conditions for the four flat plate test cases.

Case	U inlet [m/s]	FSTI %	μ_t/μ	ρ [kg/m^3]	μ [kg/ms]
T3B	9.4	6.500	100.00	1.2	1.8e-5
T3A	5.4	3.500	13.30	1.2	1.8e-5
T3A-	19.8	0.874	8.72	1.2	1.8e-5
S&K	50.1	0.180	5.00	1.2	1.8e-5
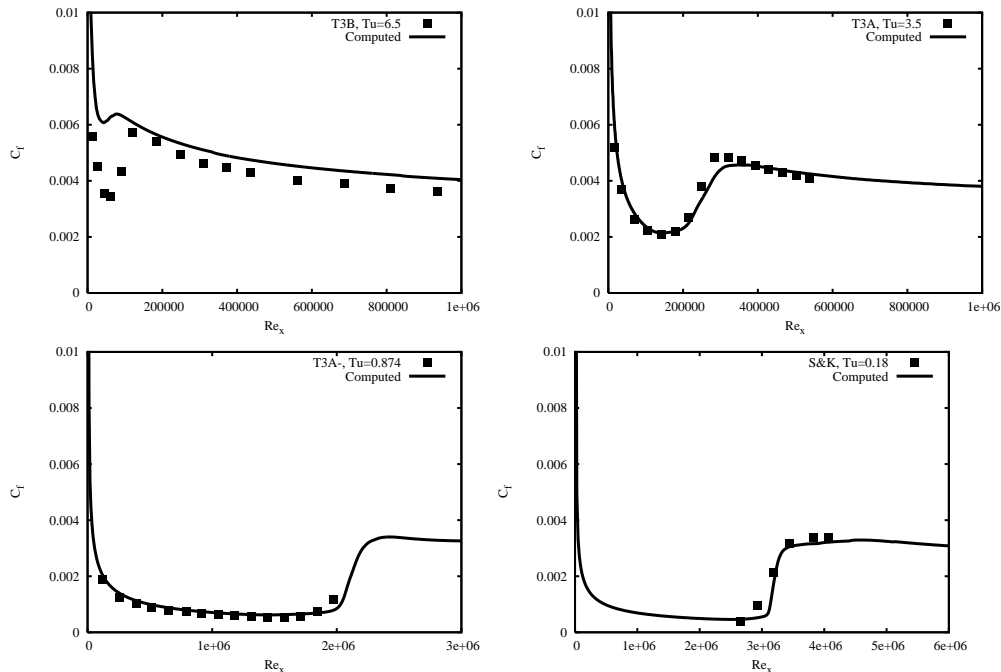
Figure 51. Verification of the empirical correlations Eqn. 27 and 28 using four zero pressure gradient flat plate cases.

The following procedure was used to determine the two functional dependencies: First a series of parametric runs were performed where the critical Reynolds number $Re_{\theta c}$ and the constant controlling the length of the transition region F_{length} was directly specified. Secondly, having found the values $Re_{\theta c}$ and F_{length} that gives the optimum agreement with the measured data, a

second series of runs were performed determining the constant α, so that using $\text{Re}_{\theta c} = \alpha\widetilde{\text{Re}}_{\theta t}$ gave identical results with the previously determined optimum. Using this procedure, the $\widetilde{\text{Re}}_{\theta t}$, $\text{Re}_{\theta c}$ and F_{length} can be determined for each of the four cases. The resulting values are listed in Table 3.

Table 3. The result of the numerical optimization of the missing correlations for $\text{Re}_{\theta c}$ and F_{length} as function of $\widetilde{\text{Re}}_{\theta t}$.

Case	$\widetilde{\text{Re}}_{\theta t}$	$\text{Re}_{\theta c}$	α	F_{length}
T3B	173	80	0.46	> 30
T3A	480	182	0.38	30
T3A-	967	532	0.55	0.55
S&K	1023	583	0.57	0.20

Comparing the critical Reynolds number from Table 3 determined by the numerical optimization with the one from Eqn. 22 excellent agreement is observed, supporting the correctness of the implementation of the model. The functional dependency is approximated by the following expressions:

$$\text{Re}_{\theta c} = 0.0005 \cdot \widetilde{\text{Re}}_{\theta t}^2 + 65(1 - e^{-\frac{\widetilde{\text{Re}}_{\theta t}^2}{1550}}) , \tag{27}$$

and

$$F_{length} = \max\left[270 \cdot e^{-\frac{\widetilde{\text{Re}}_{\theta t} - 200}{110}}, 200\right] . \tag{28}$$

The reason why the expressions do not exactly reproduce the values from Table 3 is to account for the feedback in the model due to non-linearities, and represents a final numerical optimization. The results of using the determined correlation for the four flat plate cases can be seen in Fig. 51, indicating similar agreement as observed in [2, 22]. The less than perfect agreement of the laminar part of the skin friction for the T3B case with Tu=6.5% is not due to the correlation functions used, but shows agreement identical to the best possible solution that can be obtained using fixed values for $\text{Re}_{\theta c}$ and f_{length}, see also [2]

5.6 Verification of transition prediction method

To validate the expressions derived for the two lacking correlations and the implementation of the model especially for applications related to wind energy, two airfoil flows were computed, as well as the flow around the NREL Phase-VI rotor. Additionally, the flow over a prolate spheroid at zero incidence and 30 degree incidence were performed to investigate the behavior in connection with cross flow instabilities.

5.6.1 Airfoil Flows, S809

The S809 airfoil was used as the first wind turbine related test, even though the S809 airfoil is not typical for modern turbines. The fact that the S809 airfoil was used for the NREL Phase-VI rotor which is used as a rotor test case in the present study, makes it interesting.

To verify the accuracy of the method, a grid refinement study was performed first using a series of grids based on a full coarsening of a 1024×512 grid. The y^+ of the finest grid (refinement ratio 4) was ~ 0.25 assuring a y^+ of approximately 1 on the second coarsest level (refinement
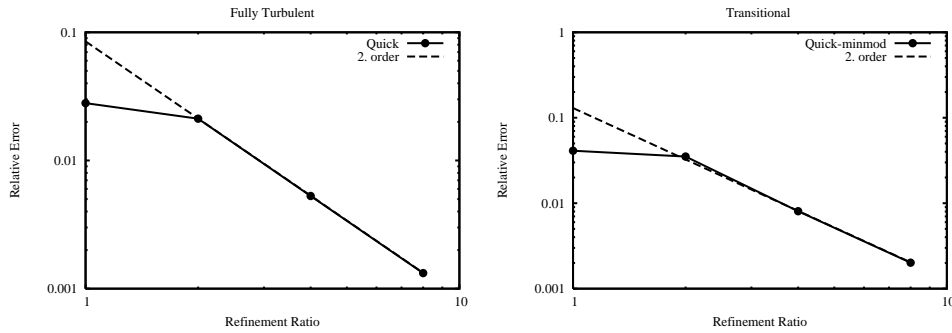
Figure 52. The order of accuracy of the EllipSys2D code using the QUICK scheme for a fully turbulent computation top, and and a TVD version of the QUICK scheme for a transitional computation bottom.

ratio 2). Additionally, it was assured that the expansion rate in the normal direction was approximately 2.5 percent at the finest grid level for the first 360 grid points, so that the expansion rate on the second coarsest level was below 10 percent. In order to capture the true order of the scheme, the grids needed to be sufficiently fine to be in the asymptotic range. For the transitional case, the fact that the transition point is in fact a discontinuity in the equations pose an additional requirement on the chordwise resolution of the grid near the transition point. In the present computation around 10 cells are used around the transition point on the second coarsest level. In Fig. 52 the outcome of these studies are shown, both indicating second order accuracy of the method is obtained already on the second coarsest level. Based on these tests, and in agreement with the previous work of Langtry [23], the necessary grid resolution can be estimated.

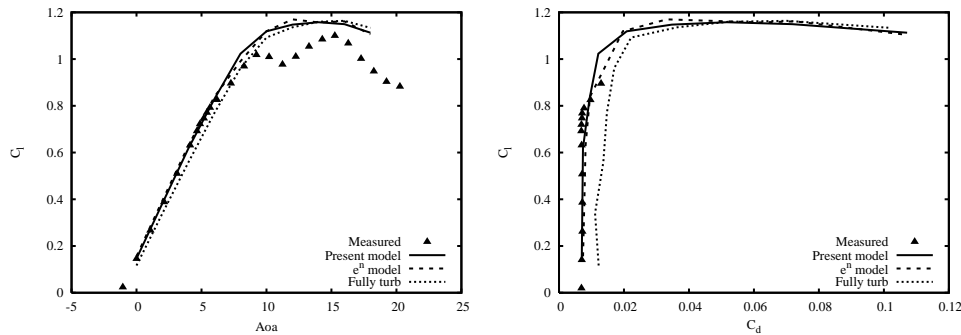The model greatly improves the agreement with measured drag for airfoils

Figure 53. Comparison of computed and measured lift and drag, using the new correlation based model, the e^n model and fully turbulent computations for the S809 airfoil.

Having verified the numerical accuracy of the method, the new $\gamma - \widetilde{\mathrm{Re}}_\theta$ based transition model was compared to an existing transition model featuring an e^n, a by-pass and a model for separation induced transition developed and implemented by Michelsen [1] and was also compared to existing measurements. The S809 airfoil was computed at a Reynolds number of 2 millon, assuming natural transition. An O-grid of 512×128 cells was used based on the grid refinement study, with a high concentration of cells near the wall to limit y^+ and a low cell expansion rate. As seen by Fig. 53 the new method agrees well with the existing extended e^n method and with measurements for the low angles of attack. Additionally, the figure shows that the transition model improves the results compared to a fully turbulent computation with respect to agrement with the measurements of Somers [28].
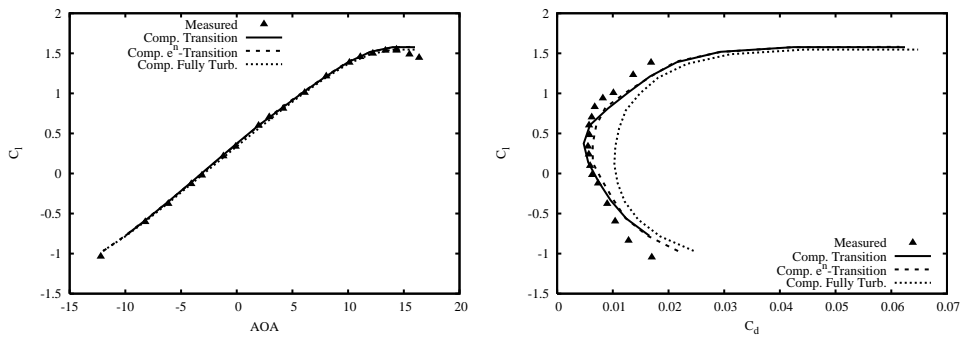
Figure 54. Comparison of computed and measured lift and drag, using the new correlation based model, the e^n model and fully turbulent computations for the NACA 63-415 airfoil.

5.6.2 Airfoil computation, NACA 63-415

Next the NACA 63-415 airfoil was investigated, an airfoil with more practical relevance for modern wind turbines. Again an O-mesh of 512×128 cells was constructed around the airfoil, using the HypGrid2D code [29]. The Reynolds number was specified to 3.0 million, and a turbulence intensity of 0.04 % was used corresponding to natural transition. The angle of attack was varied between -12 degrees and 16 degrees. In Figure 54 the computed lift is compared for the new model, the extended e^n model by Michelsen, fully turbulent computations and measurements. Good agreement is observed for all three types of computations, with minimal changes due to transition modeling. Looking at the computed drag, see Figure 54, the effects of the transition models are more evident. Here the computed drag using any of the two transition models shows much better agreement with measured data, especially at low angles of attack.

As seen from Figure 55 showing the computed C_p and C_f distributions, the reason for the large deviations between the computed drag for the transition and fully turbulent computations is clearly illustrated at 2 and 8 degrees angle of attack, where the skin friction is strongly influenced by the location of the transition point on both the suction and pressure side of the airfoil. For the two degree case, the two transition models do not predict the exact same transition location, which results in the drag being slightly too high for the enhanced e^n method and slightly too low for the present model. Even though a small difference exists between the two transition models, both models do considerably better than the fully turbulent computations, see Figure 54.

5.6.3 Prolate Spheroid

The 6:1 prolate spheroid has been used for several studies of laminar, turbulent and transitional flows. In the present study, the data of Kreplin et al. [6, 30] is used to study the performance of the model in 3D and illustrate the by-pass transition capabilities. As the present version of the model do not include the effect of cross-flow instabilities, mainly the 0 degree angle of attack case is used. The 10 and 30 degree cases may eventually be used later on to calibrate the model to account for cross-flow instabilities. A single case of the 30 degree case is shown to illustrate the lack of cross-flow capacity of the model in the present version. An O-O-grid is constructed around the spheroid, using 128 cells in the chordwise direction, 256 in the cross-flow direction and a 64×64 block at the nose and rear of the spheroid, see Figure 56. In the normal direction 128 cells are used, with a minimum cell size of $1.7 \cdot 10^{-7}$ the length of the spheroid, giving a total of 4.7 million cells.

Four cases were computed, corresponding to Reynolds numbers of [3.2, 6.4, 8.0, 9.6] million, based on free-stream velocity and length of the spheroid. In the original article [6] the turbulence intensity in the tunnel is reported to be between 0.1% and 0.2%, while it is said to
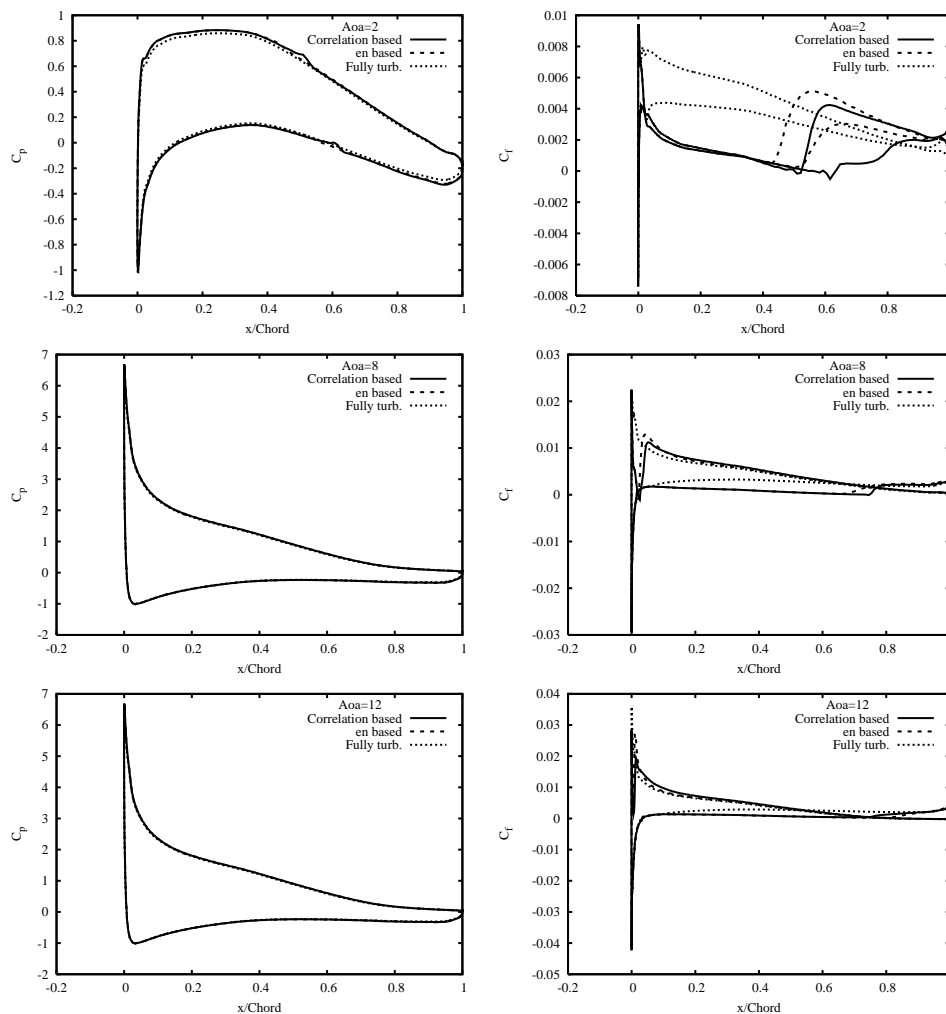
Figure 55. Comparison of computed pressure and skin friction distributions for the NACA 63-415 airfoil.

be between 0.3% and 0.4% in other references. After calibration of the computations for a Reynolds Number of 8.0 million, all computations were computed for a turbulence intensity of 0.25%. The resulting wall shear stress is shown in Fig 57. The qualitative agreement with increasing wall stress for increasing Reynolds number along with the forward shift of the transition point is well reproduced. The qualitative agreement is also good, considering that the $\Delta C_f / C_f = \pm 0.1$ is reported in the measurements.

To illustrate the lack of sensitivity of the model to cross flow instabilities, a single case of the spheroid at a Reynolds number of 7.2×10^6 and 30 degrees incidence was computed. In Fig 58 the shear stress and pressure coefficient are compared with measurements at the cross stream position $x/2a = 0.05$ close to the front of the spheroid. The agreement of the pressure is good both for the transitional and the fully turbulent computations, while the shear stress is not well predicted for either the turbulent nor the transitional computations. At this location the measurements indicate that transition is triggered by flow separation, which is reproduced by the transition model and clearly visible by the peak in the shear stress around $\phi = 140$ degrees. in Fig. 58. At the second section $x/2a = 0.48$ the agreement of the pressure distribution is still good for both the fully turbulent and the transitional computation, see Fig. 59, while some disagreement is observed for both types of computations with respect to the shear stress. At this section, the transitional computation fails to predict any laminar region. Looking at Fig. 60 the boundary layer transition happens just upstream of this position in the x-direction,

The model reproduces the forward movement of the transition point with increasing Reynolds number for the spheroid
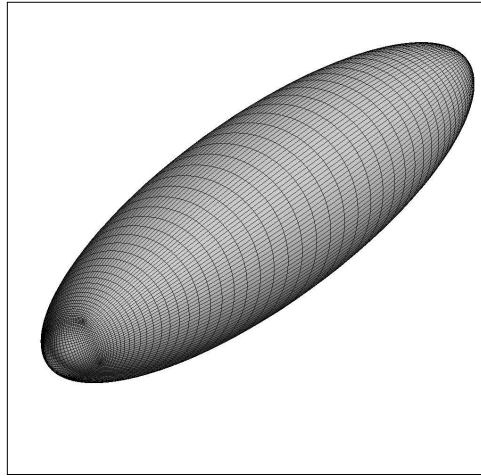
Figure 56. The surface grid topology used for the 6:1 prolate spheroid. The plot shows only every second point on the surface.
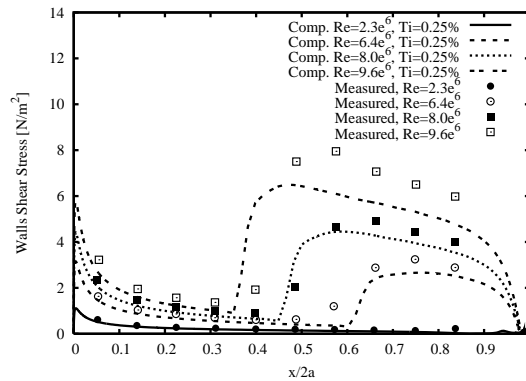

Figure 57. The measured and computed wall shear stress distributions at four different Reynolds numbers at 0 deg. incidence.

due to natural/bypass mechanisms, in contrast to the observation in the measurements. As the transition process in the measurements at this position is controlled by cross flow instabilities one should not expect the present method lacking the ability to predict this type of transition to give the correct answer. Even though the method cannot predict cross flow instabilities, there is nothing that prevents this to be included through correlations in a new version of the model.

5.7 NREL Phase-VI rotor

The final application of the model is to the well-known NREL Phase-VI dataset [7, 8]. Here the upwind cases for zero yaw angle, originally computed fully turbulent by the present author and colleagues in connection with the blind comparison in 1999 [31] were used. The mesh used in the present computations explicitly models the full two bladed rotor, using 5.2 million cells with 256 cells around the blade in the chordwise direction, a $y^+ \sim 1$ and the farfield boundary placed 80 meters from the rotor center. The mesh has previously been used for yaw computations in [32] where pictures and more details can be found.

The NREL Phase-VI rotor is based on the S809 airfoil, and as seen previously we must expect that the laminar/turbulent transition mainly affects the airfoil characteristics for aoa's below 10 degrees, corresponding to the low wind speeds for the present stall controlled turbine. At the high wind speeds/aoa's the transition even for natural transition is located very close to the
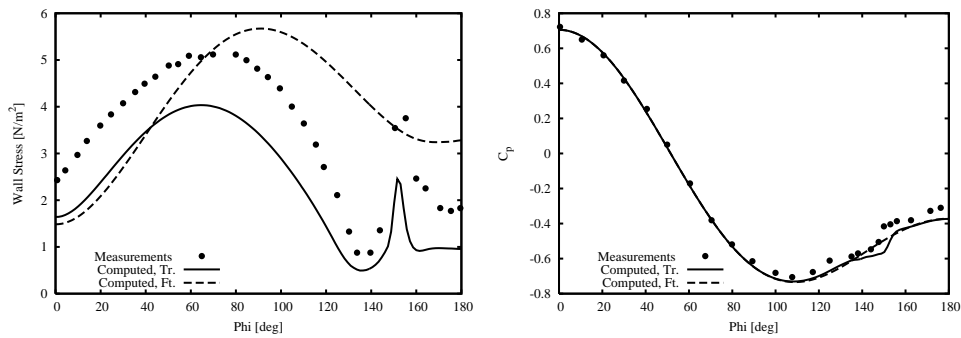
Figure 58. The measured and computed wall shear stress and pressure coefficients at x/2a=0.05 for a Reynolds number 7.2×10^6 and 30 deg. incidence, where phi (φ) is angle in the cross stream direction measured from the windward side of the spheroid.
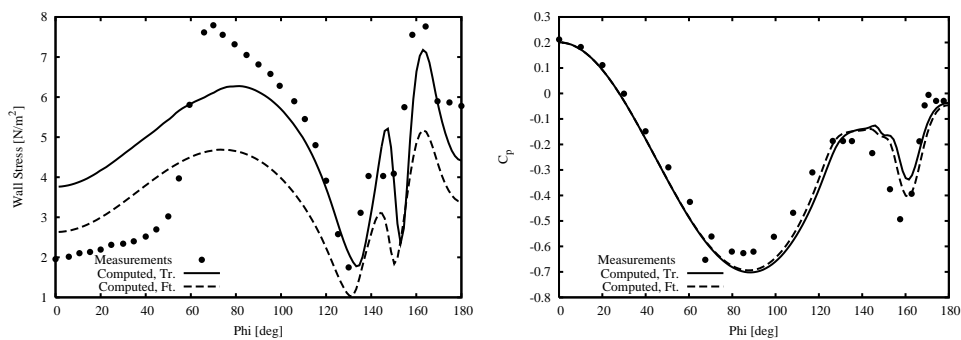

Figure 59. The measured and computed wall shear stress and pressure coefficients at x/2a=0.48 for a Reynolds number 7.2×10^6 and 30 deg. incidence, where phi (φ) is angle in the cross stream direction measured from the windward side of the spheroid.

leading edge and the results are very similar to the fully turbulent computations.

The turbulence intensity in the NASA/Ames tunnel is reported to be around 0.5 % for the velocity range investigated in the present computations [31, 33]. From reference [33] it is not clear which part of the turbulent spectra is used for the intensity estimates, and therefore the turbulence intensity is varied around the reported value to investigate possible influences on the results. In the present investigation, the turbulence intensity in percent is set to the following four values [0.5, 1.0, 1.25, 1.5]. In Fig. 5.7 the variation of the torque for the different turbulence intensities are shown. As was also seen in the original blind comparison, the present CFD solver over-predicts the torque at 10 m/s for the fully turbulent computations. The figure additionally shows how the torque decreases around stall when the turbulence intensity is lowered. For the
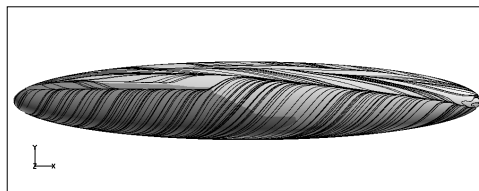

Figure 60. Intermittency and limiting streamlines on the surface of the spheroid at a Reynolds number of 7.2×10^6 and 30 deg. incidence. The flow is from bottom left and the dark regions at the bottom left indicates laminar flow, while the light gray regions indicate turbulent flow.

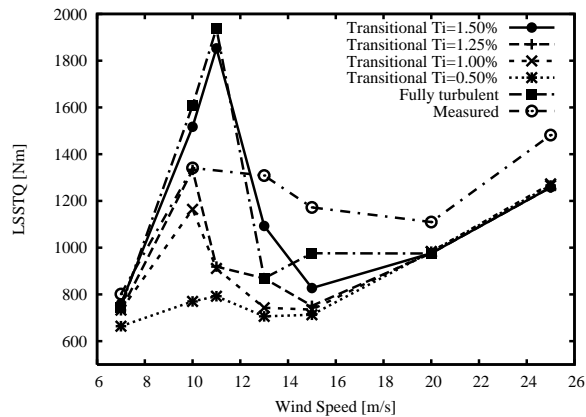higher wind speeds, no influence of the transitional model is observed.

Figure 61. The low speed shaft torque of the NREL Phase-VI rotor for fully turbulent and transitional conditions all compared to measured values.

For a low turbulence inflow it is well-known that the S809 airfoil at low aoa's has separation induced transition located around half chord at both suction and pressure side, producing a pattern similar to the one observed at the 7 m/s transitional case in Fig 62. When the aoa is increased above ~ 5 degrees the transition point on the upper side moves towards the leading edge. At higher aoa's not much difference is observed between the by-pass transitional, the 'natural' transitional and the fully turbulent cases, due to the leading edge proximity of the transition point, which explains the minimal differences observed in the low speed shaft torque for high wind speeds. The reason why the inflow turbulence intensity can severely influence the performance of the rotor close to stall, as observed in Fig 5.7 can not directly be explained by the change in airfoil performance observed in 2D between transitional and fully turbulent cases. This effect is connected to the three dimensionality of the flow and the rotation of the blade. For all cases computed here, even for the fully turbulent cases, separated flow is predicted on the suction side of the blade in the root region. For the 7 m/s case, the transition of the flow from laminar to turbulent around half chord is capable of suppressing this spanwise component. When increasing the wind speed to 10 m/s, the spanwise flow become stronger in the root region. Depending on the chordwise location of the transition point at sections close to the root, which is controlled by the inflow turbulence, the flow on the suction side may become totally separated. For a turbulence intensity of 1.25% the flow pattern for the transitional case looks similar to the fully turbulent flow as seen in Fig 62. Identical patterns are observed for turbulence intensity of 1.0% and 1.5%, while the pattern totally changes when the turbulence intensity is lowered to 0.5%, where the computations predict the flow to be totally stalled at the suction side of the blade.

Additionally, we need to be aware that the intensity is given relative to the free wind speed, while the turbulence intensity observed by the individual blade sections is influenced by the rotational speed of the blade. The intensity in the computations will decrease when moving towards the tip. Using the rotational speed of the NREL Phase-VI rotor of 7.53 rad/s, a wind speed of 10 [m/s] and a turbulence intensity of 1.5% based on free stream velocity the turbulence intensity will vary from 1.20% at 1 meter radius to 0.38% at 5 meters radius. The fact that in reality the rotationally sampled turbulence spectrum as seen by the rotating blade will look completely different from the turbulence spectra observed by a non-rotating blade, may change this picture. In the present version the transition model cannot account for the length scale and rotational sampling effects on the turbulence intensity.

Looking at pictures of limiting streamlines on the blade surface for three wind speeds, the transitional flow patterns are generally more complicated due to the presence of laminar separation/turbulent reattachment regions, which similar to what is know for typical trailing edge

stall on rotors has a tendency to spread radially towards the blade tip, see Fig. 62. Additionally, the figures reveal that when the flow speed is beyond 15 m/s the transitional and fully turbulent flow patterns are very similar. The effects of transition may have a severe effect on the power production depending on the actual rotor design and airfoil sections, and from the present investigation this may be especially true for the lower wind speeds and near the onset of stall.
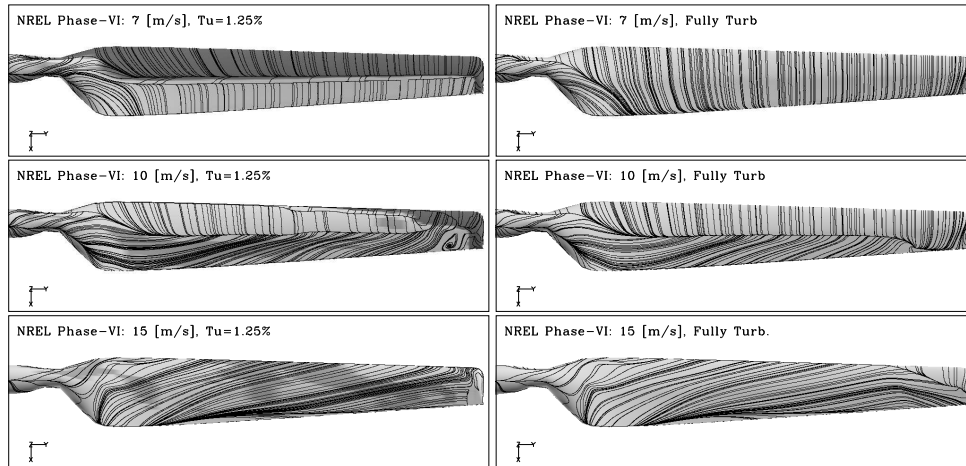
Figure 62. Limiting streamlines on the suction side of the blades. The light gray regions indicates the fully turbulent regions, while the dark regions in the first and the third picture from top are laminar regions.

5.8 Conclusion

The correlation based transition model of Menter et al. [2] has been implemented in the incompressible EllipSys2D/3D Navier-Stokes solver. Based on a series of zero pressure gradient flat plate boundary layers, expressions for the two missing correlation functions relating $Re_{\theta c}$ and F_{length} to $\widetilde{Re}_{\theta t}$ have been determined. Next, the model has been used to predict the lift and drag for two wind turbine airfoils, the S809 and NACA63-415 respectively. Both computations show good agreement and distinct improvement in the drag predictions compared to using fully turbulent computations. The model was used to successfully predict transition on a 6:1 prolate spheroid at zero degrees incidence for four different Reynolds numbers, while the model due to lack of cross-flow by-pass transition capability was not able to predict the correct location of transition for the spheroid at 30 degrees incidence. The model was finally applied to the well known NREL Phase-VI rotor, corresponding the the upwind cases from the original blind comparison. It was shown how the transition model, through variation of the intensity of the inflow turbulence could improve the prediction around stall, while the low wind speed and high wind speed regions were nearly unaffected by the transition model. Generally, one must expect that the transition process can be very important for predicting the correct aerodynamics of rotors depending of rotor design and airfoil choice, and that the present model can be a valuable tool.

5.9 Post Scriptum

After the present work was finished, an error was discovered in the 3D implementation of the model. This error caused the transition model to predict a too aft location of the transition point. The consequence of this error was a excessive sensitivity to inflow turbulence level, as seen for the NREL Phase-VI rotor computations. Having corrected this flaw in the model, the high sensitivity of the shaft torque on the inflow turbulence level disappeared, while producing

results similar to the 1.0 % case shown in the present work for turbulence intensity varying between 0.1 and 0.5 percent. The model is at the moment being further verified, both with respect to the correlation functions and further applications.

5.10 Acknowledgement

References

[1] Michelsen J.A. *Forskning i aeroelasticitet EFP-2001*, chapter Beregning af laminar-turbulent omslag i 2D og 3D, page 73. Risø-R1349(DA). 2002. In Danish.

[2] Menter F.R., Langtry R.B., Likki S.R., Suzen Y.B., Huang P.G., and Völker S. A Correlation-Based Transition Model Using Local Variables, Part I - Model Formulation. In *Proceedings of ASME Turbo Expo 2004, Power for Land, Sea, and Air*, Vienna, Austria, June 14-17 2004. ASME. GT2004-53452.

[3] Menter F.R., Langtry R.B., Likki S.R., Suzen Y.B., Huang P.G., and Völker S. A correlation-based transition model using local variables, part ii - test cases and industrial applications. In *Proceedings of ASME Turbo Expo 2004, Power for Land, Sea, and Air*, Vienna, Austria, June 14-17 2004. ASME. GT2004-53454.

[4] Toyoda A., Misaka T., and Obayashi S. An Application of Local Correlation-Based Transition Model to JAXA High-Lift Configuration Model. AIAA Paper 2007-4286, June 2007.

[5] Misaka T. and Obayashi S. Application of Local Correlation-Based Transition Model to Flows around Wings. 44th AIAA Aerospace Sciences Meeting and Exhibit, January 2006. AIAA 2006-918.

[6] Kreplin H.P., Vollmers H., and Meier H.U. Measurements of the Wall Shear Stress on an Inclined Prolate Spheroid. *Zeitschrift für Flugwissenschaften und Weltraumforschung*, (4):248–252, 1982.

[7] Simms D., Hand M.M., Fingersh L.J., and Jager D.W. Unsteady Aeorydnamics Experiment Phases II-IV: Test Configurations and Available Data Campaigns. NREL/TP -500-25950, Nat. Ren. Energy Lab., Golden, CO, 1999.

[8] Fingersh L., Simms D., Hand M., Jager D., Cortrell J., Robinsion M., Schreck S., and Larwood S. Wind Tunnel Testing of NREL's Unsteady Aeorydnamics Experiment. In *2001 ASME Wind Energy Symposium*, pages 129–135, Reno, NV, January 11-14 2001. ASME. AIAA-2001-0035.

[9] Hand M., Simms D., Fingersh L.J., Jager D., and Larwood S. Cotrell J., Schreck S. Unsteady Aeorydnamics Experiment Phases VI: Wind tunnel Test Configurations and Available Data Campaigns. NREL/TP -500-29955, Nat. Ren. Energy Lab., Golden,CO, 2001.

[10] Michelsen J.A. Basis3D - a Platform for Development of Multiblock PDE Solvers. Technical Report AFM 92-05, Technical University of Denmark, 1992.

[11] Michelsen J.A. Block structured Multigrid solution of 2D and 3D elliptic PDE's. Technical Report AFM 94-06, Technical University of Denmark, 1994.

[12] Sørensen N. N. General Purpose Flow Solver Applied to Flow over Hills. Risø-R- 827-(EN), Risø National Laboratory, Roskilde, Denmark, June 1995.

[13] Rhie C. M. *A numerical study of the flow past an isolated airfoil with separation*. PhD thesis, Univ. of Illinois, Urbana-Champaign, 1981.

[14] Patankar S. V. *Numerical Heat Transfer and Fluid Flow*. Hemisphere, 1980.

[15] Patankar S. V. and Spalding D. B. A Calculation Prodedure for Heat, Mass and Momentum Transfer in Three-Dimensional Parabolic Flows. *Int. J. Heat Mass Transfer*, 15:1787, 1972.

[16] Issa R. I. Solution of the Implicitly Discretised Fluid Flow Equations by Operator-Splitting. *J. Computational Phys.*, 62:40–65, 1985.

[17] Issa R. I., Gosman A. D., and Watkins A. P. The Computation of Compressible and Incompressible Recirculating Flows by a Non-iterative Implicit Scheme. *J. Computational Phys.*, 62:66–82, 1986.

[18] Khosla P. K. and Rubin S. G. A diagonally dominant second-order accurate implicit scheme. *Computers Fluids*, 2:207–209, 1974.

[19] Menter F. R. Zonal Two Equation k-ω Turbulence Models for Aerodynamic Flows. AIAA-paper-932906, 1993.

[20] Sørensen N.N. Rotor computations using a 'Steady State' moving mesh. IEA Joint Action Committee on aerodynamics, Annex XI and 20, Annex XI and 20. Aero experts meeting, Pamplona, Spaine, May 2005.

[21] Demirdzic I. and Peric M. Space conservation law in finite volume calculations of fluid flow. *Int. J. Numer. Methods Fluids*, 8:1037–1050, 1988.

[22] Menter F.R., Langtry R., and Völker S. Transition Modelling for General Purpose CFD Codes. *Flow Turbulence Combust*, 77(1-4):277–303, November 2006.

[23] Langtry R.B., Gola J., and Menter F.R. Predicting 2D Airfoil and 3D Wind Turbine Rotor Performance using a Transition Model for General CFD Codes. AIAA-paper-2006-0395, 2006.

[24] Savill A.M. *Some recent progress in the turbulence modelling of by-pass transition*, page 829. Elsevier, The Netherlands, 1993.

[25] Savill A.M. *One-point closure applied to transition*, pages 233–268. Kluwer, Cambridge, 1996.

[26] Savill A.M. *By-Pass transition using Conventional Closures*, chapter 17, pages 464–492. Cambridge University Press, Cambridge, 2002.

[27] Schubauer G.B. and Klebanoff P.S. Contribution on the Mechanics of Boundary Layer Transition. NACA-TN- 3489, NACA, 1955.

[28] Somers D.M. Design and Experimental Results for the S809 Airfoil. NREL/SR- 440-6918, National Renewable Energy Laboratory, US, Golden, Colerado 80401-3393, January 1997.

[29] N.N Sørensen. HypGrid2D a 2-D Mesh Generator. Risø-R- 1035-(EN), Risø National Laboratory, Roskilde, Denmark, Feb 1998.

[30] Meier H.U. and Kreplin H.P. Experimental Investigation of the Boundary Layer Transition and Separation on a Body of Revolution. *Zeitschrift für Flugwissenschaften und Weltraumforschung*, (2):65–71, Marts/April 1980.

[31] Simms D., Schreck S., Hand M., and Fingersh L.J. NREL Unstead Aeorydnamics Experiment in the NASA-Ames Wind tunnel: A Comparison of Predictions to Measurements. NREL/TP -500-29494, Nat. Ren. Energy Lab., Golden, CO, 2001.

[32] Sørensen N.N.and Michelsen J.A. and S. Schreck. Application of CFD to wind turbine aerodynamics. In Tsahalis D.T., editor, *CD-Rom proceedings. 4. GRACM congress on computational mechanics*, Patras, Greece, June 2002.

[33] Zell P.T. Performance and Test Section Flow Characteristics of the National Full-Scale Aerodynamics Complex 80- by 120-Foot Wind Tunnel. NASA TM 103920, NASA, January 1993.

6 Verification of Airfoil Design With Focus on Transition

Author: Christian Bak, Mads Døssing, Helge A. Madsen, Peter B. Andersen, Mac Gaunaa (Risø DTU)
Peter Fuglsang, Stefano Bove (LM Glasfiber)

This chapter presents wind tunnel tests on three different airfoils in the LM Glasfiber wind tunnel, Denmark. The objectives with the wind tunnel tests were two fold: 1) To detect the transition from laminar to turbulent flow on airfoil surfaces and 2) to verify the methodology for designing airfoils with high lift-drag ratio, insensitive to surface contamination and turbulence intensity and showing high bending stiffness.

Approximately 70 microphones were mounted in the surface of each of the three airfoils NACA0015, Risø-B1-18 and Risø-C2-18 to measure the transition from laminar to turbulent flow. Information such as the transition point as a function of the Reynolds number, the Tollmien-Schlichting frequency building up upstream of the transition point and energy spectra at different positions of the airfoil surface are available from this measurement technique. Also, good agreement between measurements and the e^n transition model was seen.

The Risø-C2 airfoil family is dedicated for MW-size wind turbines. It was designed to have high maximum lift coefficient, while maintaining high aerodynamic efficiency. Given these characteristics the airfoil was designed with maximum stiffness. Finally, because of the varying wind turbine conditions the airfoil was designed to be resistant to surface contamination and varying turbulence intensity. The design was carried out with a quasi 3D multi disciplinary optimization tool to take into account the complete blade shape and rotor flow. Thus, the design of the Risø-C2-18 airfoil was verified and showed good agreement with predicted characteristics.

6.1 Nomenclature

AOA	Angle of attack
AOA_r	Angle of attack relative to zero lift AOA
a_k	Fourier coefficient
b_k	Fourier coefficient
c	Chord length
c_l	Lift coefficient
c_d	Drag coefficient
c_p	Normalized coefficient for the pressure on the airfoil surface
C_P	Normalized coefficient for the wind turbine rotor power
f	Frequency
k	Fourier index
Ma	Mach number
Re	Reynolds number
U	Flow speed
x	Coordinate in chordwise direction
μ_1	Mean of the power spectra
ρ	Air density
σ	Standard deviation

6.2 Introduction

The uncertainty of the turbulence intensity for the inflow to wind turbines in the very small scales makes the performance of wind turbine airfoils uncertain. Also, Computational Fluid Dynamics (CFD) has shown significant differences in the aerodynamic performance if either fully turbulent flow or transitional flow are assumed, see Chapter 5. Thus, it is important to

know 1) how the turbulence intensity is in the small scales and 2) how trustworthy the models are predicting the transition. This fact motivated Risø DTU to start up an investigation on the flow behaviour in small scales, i.e. eddies of the size of the chord length or smaller. This led to the development of a technique using microphones, which can measure pressure vibrations up to 20kHz. This technique was in comparison to e.g. Kulite sensors tested in the VELUX wind tunnel December 2006 and June 2007 to investigate the applicability for this purpose. It turned out that the microphones were both robust and gave valuable information.

From October to December 2007 three wind tunnel test were carried out in the LM Glasfiber wind tunnel where the Risø-B1-18, Risø-C2-18 and NACA0015 were tested. The latter airfoil was tested because the airfoil is well known and has been tested in similar tests before [1]. The two former airfoils were tested to investigate the design philosophy and to investigate how much the simulation models can be trusted, e.g. in the airfoil design process. This knowledge is important because design of tailored airfoils for wind turbine rotors is essential for the continuing development of wind turbines. It has been known for decades that wind turbine airfoils should differ from traditional aviation airfoils in choice of design point, off-design characteristics and structural properties. The development of wind turbine airfoils has been ongoing since the mid 1980's. Significant efforts have been made by Tangler and Somers [2], Timmer and Van Rooij [3], Björk [4] and Fuglsang and Bak [5]. For wind turbine airfoils operating in the atmospheric boundary layer there is influence from the turbulence intensity and contamination of bugs and dust and the airfoils should show both high performance in terms of high lift-drag ratio and maximum lift resistant to leading edge roughness. The Risø-C2 airfoil family was designed for MW-size wind turbines with variable speed and pitch control and many characteristics from the Risø-B1 airfoil family were inherited because this airfoil family has shown to be both efficient and to have a high degree of insensitivity to leading edge roughness. However, evaluating the Risø-B1 family has also shown the need for maximizing the stiffness and thereby maximizing the moment of resistance around the chord axis, i.e. the flap direction. Furthermore, the new airfoil family was designed to have a high degree of compatibility.

Key design objectives for the new airfoil family were twofold: (1) To maximize the lift-drag ratio and (2) To have a high $c_{l,max}$. Insensitivity of maximum lift to leading edge roughness was ensured by two additional design objectives: (1) Having suction side transition from laminar to turbulent flow in the leading edge region for angles of attack close to but below $c_{l,max}$ and (2) Obtaining a high $c_{l,max}$ with simulated leading edge roughness. Further design objectives ensured good structural and aerodynamic compatibility between the different airfoil sections and good structural properties for inboard airfoils.

The design was carried out with a Risø in-house multi disciplinary optimization tool, AIRFOILOPT, that has been developed since 1996 [6], which was extended to include a complete blade with its structural surface characteristics and rotor aerodynamics. The numerical optimization algorithm works directly on the airfoil shape providing a direct and interdisciplinary design procedure, where multiple design objectives for aerodynamics and structure may be handled simultaneously. This chapter describes the microphone measurements and the design and verification of the Risø-C2 airfoil family.

6.3 Measurement set up in LM Glasfiber wind tunnel

The Risø-B1-18, Risø-C2-18 and NACA0015 airfoils were tested in the LM Glasfiber LSWT wind tunnel in Lunderskov, Denmark, see Figure 63.

The tunnel is of the closed return type with a closed test section and with a cross section of 1.35×2.70 m. The flow speed was between 26.7 m/s to 100 m/s with a turbulence intensity of around 0.1%. The airfoils had a chord length of 900 mm and the width in spanwise direction was 1350 mm. The Reynolds number was between $Re = 1.6\times10^6$ and $Re = 6.0\times10^6$, which is the maximum attainable. The airfoils were mounted on a turntable to measure high precision angles of attack. The absolute pressure was measured using 96 pressure taps using a PSI
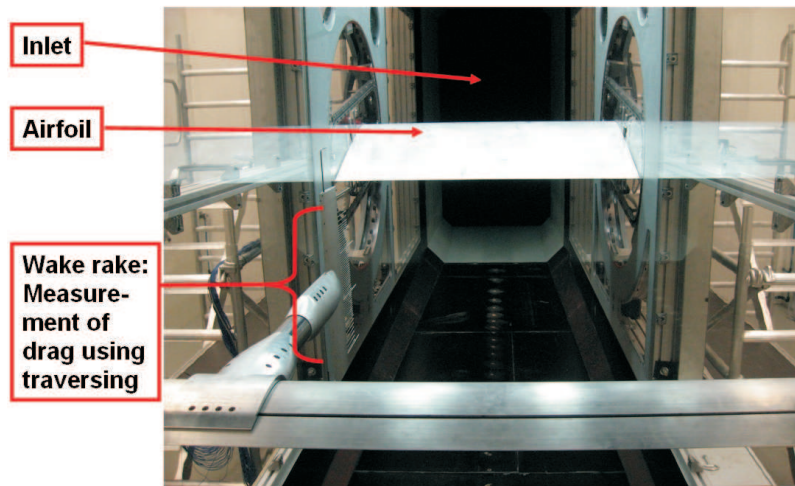
Figure 63. The LM Glasfiber wind tunnel.

measurement system with a sampling rate of 5Hz. The aerodynamic characteristics were obtained from the pressure distributions and from the wake rake traversing in spanwise direction for 50sec. In the airfoil section wake, a wake rake consisting of 54 pressure probes was positioned. The data acquisition system used was the PSI system, see [7]. Microphones of type Sennheiser KE 4-211-2 with a linear characteristic from 30Hz to 20kHz were surface mounted in the airfoils from the very leading edge along the chord to close to the trailing edge, see Figure 64.

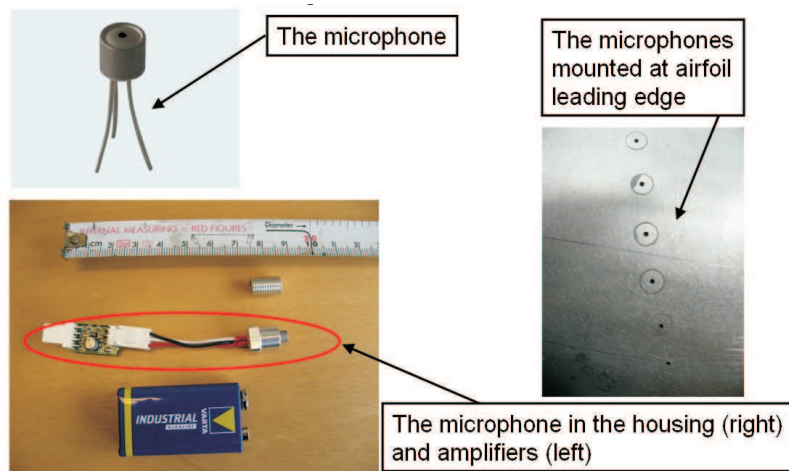Microphones were mounted in the airfoil surfaces.

Figure 64. The microphones mounted in the airfoil surface.

The data acquisition was carried out using National Instruments CampactRIO, cRIO-9052 which sampled with 50kHz. Thus, simultaneous sampling of all microphone signals was carried out. Besides the microphones in the airfoil surface, also microphones outside the test section were mounted to measure the background noise from motors etc.

Steady state polar measurements were conducted with several different configurations of the airfoils, e.g. 1) Clean surface with no aerodynamic devices mounted on the airfoil (Clean) and 2) Leading edge roughness (LER) simulated by 90 zigzag tape of height 0.40 mm and width 3 mm, where the zigzag tape was mounted at the suction side at $x/c = 0.05$ and at the pressure

side at $x/c = 0.10$. This is labeled standard roughness. Also, two additional configuration with the same kind of zigzag tape at $x/c = 0.02$ on the suction side and bump tape with height 0.12 mm were used. The different configurations were as well tested with two different grids in the tunnel upstream of the airfoils to generate additional turbulence, see Figure 65. The first grid (grid1) had a distance between the plates in the grid of 200 mm and the second grid (grid2) had a distance between the wires of 100 mm.
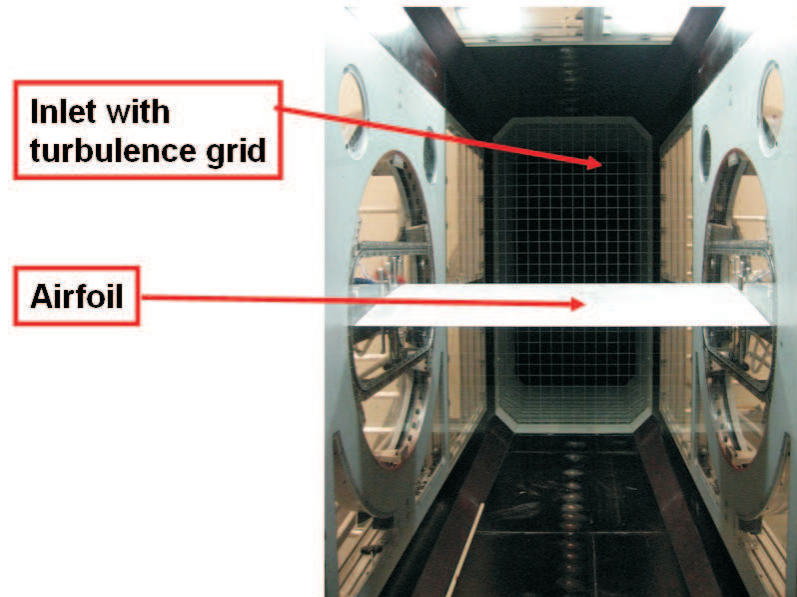

Figure 65. The LM Glasfiber wind tunnel including grid upstream of airfoil.

6.4 Method for transition detection

2D flow measurements are made at Reynolds and Mach numbers corresponding to wind turbine operation.

Sections of three different airfoils were equipped with microphones embedded in the surface, the Risø-B1-18, Risø-C2-18 and NACA0015 airfoils. 2D flow properties were measured at Reynolds numbers from 1.60×10^6 to 6.00×10^6 and Mach numbers in the range from 0.08 to 0.30 [1]. This corresponds well to the conditions of a full scale horizontal axis wind turbine. An efficient numerical method for automatic detection of transition was developed and the processing of microphone data has been established. Literature about experimental determination of transition is very limited and in most cases at too low Reynolds numbers. Therefore, a direct comparison with existing results has not been made. A thorough presentation of the experiment and data processing is given in the report [8]. A comprehensive set of results is given in the Appendix reports [9], [10] and [11].

Time series of pressures have been obtained simultaneously at all microphone positions for a constant angle of attack, *Re* and *Ma* number. The transition is then detected by observing how statistical quantities varies over the chord. Two quantities, the sample standard deviation (σ) and the mean of the power spectra (μ_1), are especially important. The former is calculated directly from the sample vector $\mathbf{Y}$

$$\mathbf{Y} = \{y_1 \ldots y_n \ldots y_N\}^T$$

$$\sigma = \sqrt{\frac{1}{N} \sum_{n=1}^{N} (y_n - \bar{Y})^2} \quad \text{where} \quad \bar{Y} = \frac{1}{N} \sum_{n=1}^{N} y_n$$

[1]Based on incompressible speed of sound = 333 m/s

The latter, μ_1, is calculated from the power spectrum (P_s) as a raw moment of order 1 about zero

$$P_s = \sqrt{a_k^2 + b_k^2}$$

$$\mu_1 = \frac{\int_0^{f_{Ny}} f P_s \, df}{\int_0^{f_{Ny}} P_s \, df}$$

Where a_k and b_k are Fourier coefficients. The integral is calculated numerically using the appropriate relation between k and frequency f. f_{Ny} is the Nyquist frequency, i.e. the upper bound of frequencies in the power spectrum. This formulation is equivalent to normalizing the power spectrum to a probability distribution and calculating the mean. From a physical point of view higher values of μ_1 means that a larger proportions of the energy at high frequencies are present relative to low frequencies. Notice the special definition of the power spectrum.

Figure 66 shows σ and μ_1 plotted against angle of attack (α) and relative chordwise position (x/c) for a clean Risø-B1-18 airfoil at $Re = 3.0 \times 10^6$. σ is scaled by the dynamic pressure ($0.5\rho U^2$), but it is noted that this is not a sufficient scaling parameter and $\frac{\sigma}{0.5\rho U^2}$ decreases with increasing Reynolds number. At transition σ increases and in some regions there is even a clear peak. In stall there is a substantial increase in σ close to the trailing edge. In general, unfortunately, the data is not as easily interpreted as in this case.

μ_1 varies in a well defined manner and at transition it increases monotonically to a near constant value. This is true in practically all cases and the only important variation is the length in chordwise direction over which μ_1 is increasing. The latter can be interpreted as the distance over which the full transition occurs, but this is not known as a fact because only the initial instability can be determined exactly from observations of Tollmien-Schlichting frequency peaks. The exact position of a fully-developed turbulent boundary layer can not be determined. To enable a stable numerical analysis the transition point (x_{tr}) is defined to be the point of maximum positive derivative in the chordwise direction. I.e. formally as

$$x_{tr} \equiv \left\{ x \quad | \quad \left. \frac{d\mu_1}{dx} \right|_x = max\left(\frac{d\mu_1}{dx} \right) \right\} \tag{29}$$

Figure 67 (left) shows the contours of Figure 66 (right), i.e. contours of μ_1. There is a clear band at transition and the center of this corresponds to x_{tr}. Transition points calculated in the airfoil flow simulation code XFOIL [12] are also shown, corresponding to turbulence intensities of the incoming flow of 0.563%, 0.245%, 0.106% and 0.07%, respectively. 0.07% corresponding to free transition. The agreement is good except for $\alpha < $-5 deg, which is typical for the XFOIL computations. Figure 67 (right) shows the Fourier spectra at various chordwise positions at 7° angle of attack. The instability around the Tollmien-Schlichting frequency is seen as well as how a broad band of frequencies quickly develops at transition. Due to numerical issues there is an uncertainty of approximately 5% on x_{tr} if detected within 10% of the leading edge, however in most cases this is not important because the transition is known to be very close to the leading edge.

6.5 Results from transition detection

In the following only selected results for the suction side is presented and without a turbulence grid mounted. The turbulence intensity in the tunnel is believed to be close to the conditions that are present at normal operation for wind turbine rotors.

Figure 68 shows x_{tr} detected on clean airfoils. Despite the uncertainty near the leading edge (i.e. at low values of x_{tr}/c), it is clearly seen at what angle the transition shifts fast to the leading edge. The Risø-C2-18 airfoil performs best, with a shift around 8 deg at $Re = 6.0 \times 10^6$. The transition moves forward with increasing Reynolds number for all airfoils, and the forward shift happens at lower angles of attack.
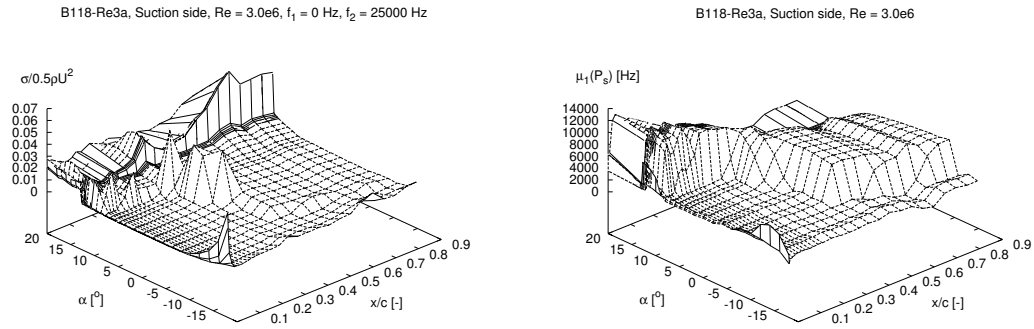
Figure 66. Scaled pressure standard deviation (left) and mean of Fourier spectrum (right) plottet against angle of attack and chordwise position
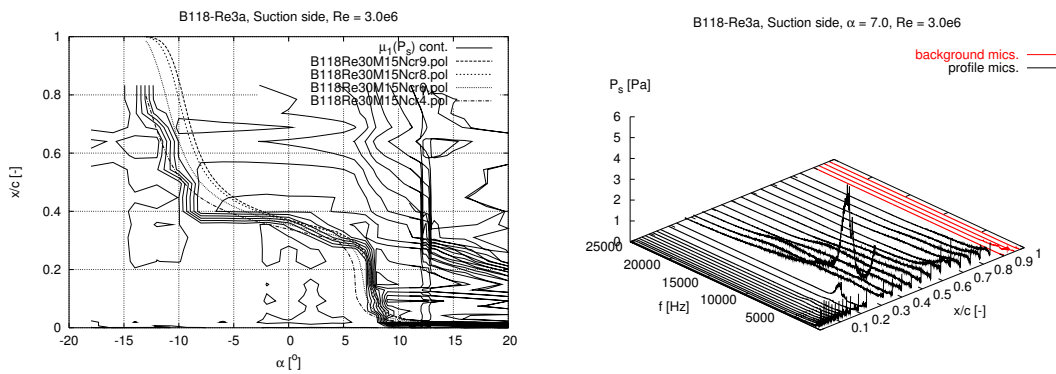

Figure 67. Contours of Figure 66.right (left) and Fourier spectra at α=7° (right)

Figure 69 shows x_{tr} detected on airfoils with trip wire/bump tape. The effect is strongly dependent on the Reynolds number. All airfoils are largely unaffected at $Re = 1.6 \times 10^6$. At $Re = 3.0 \times 10^6$ the transitions shifts to the leading edge at α values 1-2 deg lower than in the clean case. At $Re = 6.0 \times 10^6$ this happens at approximately zerodeg angle of attack, which is substantially lower than in the clean case for Risø-B1-18 and Risø-C2-18. The Risø-C2-18 airfoil has a visible hysteresis effect at $Re = 1.6 \times 10^6$ due to the angle of attack being increased into deep stall and then lowered. This effect is seen in practically all measurements.

ZZ90 and LER forces transition at all Reynolds numbers.

6.6 Discussion of the transition detection

The numerical method for transition detection based on Eq. (29) is very stable and has some nice numerical properties. Contour plots of μ_1, e.g. Figure 67, gives a clear picture of the transition process by manual inspection. A major drawback is the numerical detection of the maximum derivative which in the 2D case is troublesome near the leading edge. On full size turbines the 3D flow properties may affect the numerical stability in regions away from the leading edge but this is not yet known for sure. The Fourier spectra can be made from relatively few samples (e.g. 4096 measurements of pressure) which can be sampled in approximately 0.1 seconds and corresponds to a rotation of a large turbine of approximately 5 deg. It is hoped that flow properties are relatively constant in this time period, allowing the properties on rotating turbines to be measured as function of time/position.

XFOIL predicts the transition point well for the clean Risø-B1-18 and Risø-C2-18 airfoils,
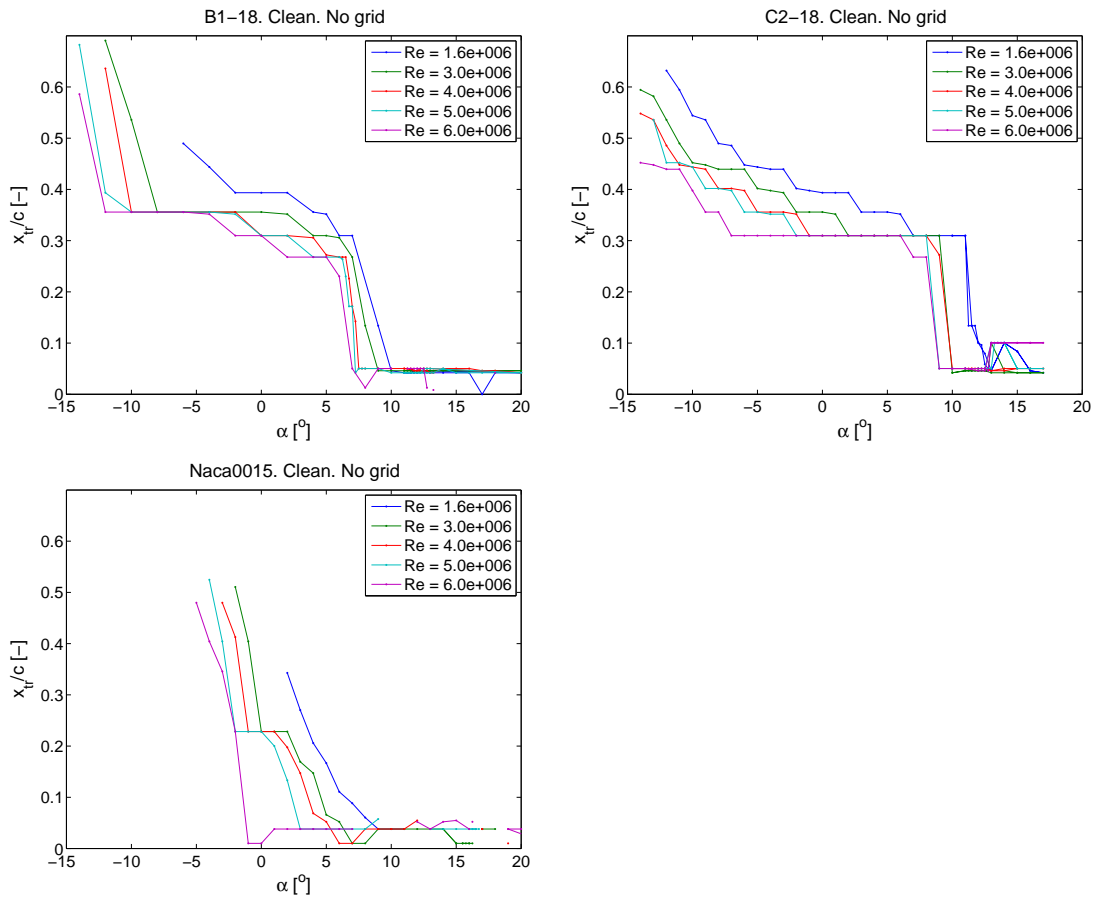
Figure 68. Transition points on clean airfoils.

with the exception of inflow angles less than -5deg. These airfoils are designed in a manner which can be modeled accurately in XFOIL and the results confirm this. Only a limited number of calculations with forced transition has been made and the agreement with experimental data is not known. It is noticed that the effect of tripwire / bump tape depends strongly on Reynolds number and does not necessarily force transition, and therefore it is difficult to model numerically. The agreement between XFOIL and measured transition for a clean NACA0015 airfoil is not good except at Re=1.6×10^6. For larger Reynolds numbers the calculations are too optimistic. Details can be found in [11].

Turbulence grids were mounted in the wind tunnel in order to increase the turbulence intensity. This clearly enhances transition but it is difficult to make any general conclusions and the cases must be studied individually. The turbulence intensity with grids mounted has not yet been successfully measured and it is therefore not known if the turbulence intensities are of the same scale as for full size turbines.

6.7 Method for airfoil design

The airfoil design tool can be divided into a 2D design tool and a 3D design tool. The 2D design tool has been used to design the former Risø airfoil families. It uses a direct method where numerical optimization is coupled with both the flow solver XFOIL [12], which is a panel code with inviscid/viscous interaction, and the flow solver EllipSys2D, which is a code based on the solution of the Navier Stokes equations in 2D [13], [14], [15]. A number of design variables form the airfoil shape, which is optimized subject to design objectives and constraints. Direct methods, such as the method used, are basically interdisciplinary and multi-point and they
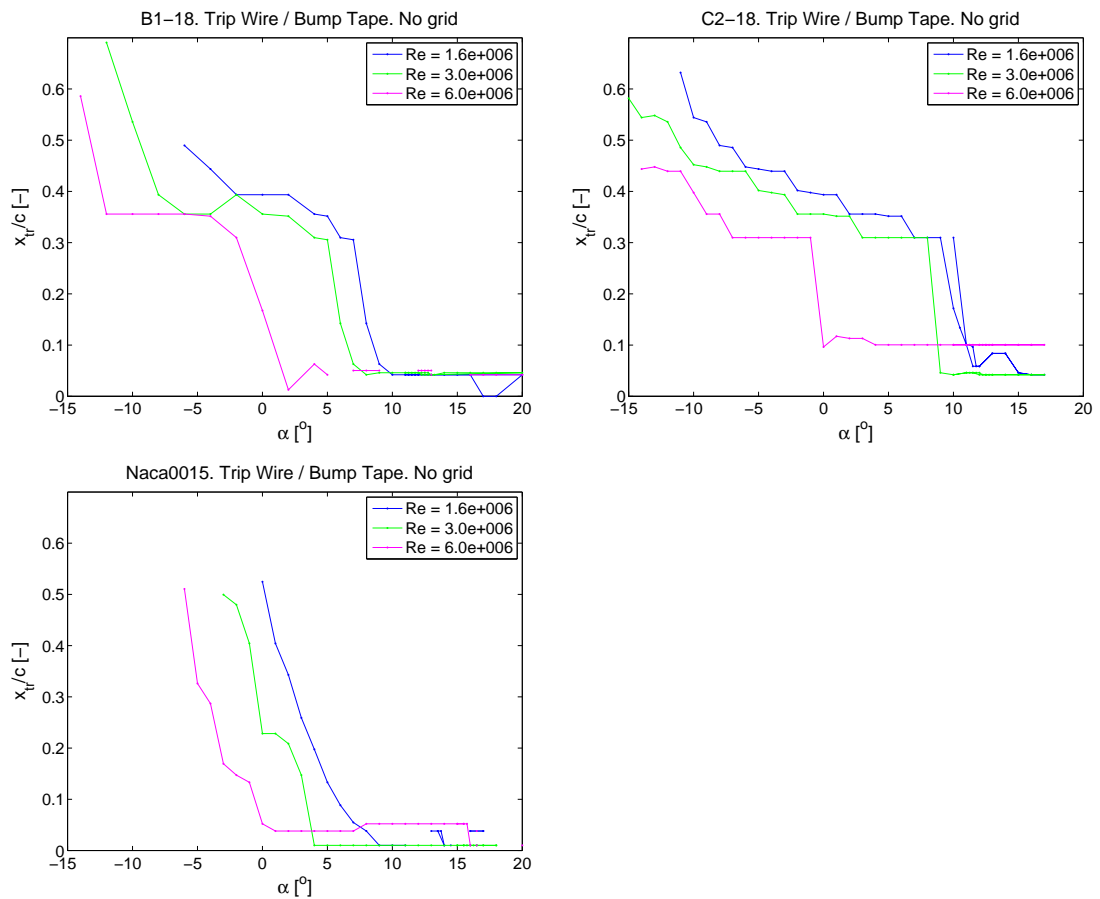
Figure 69. Transition points on airfoils with trip wire/bump tape

allow direct use of integrated response parameters such as airfoil c_l and c_d directly as design objectives. Also, boundary layer response parameters, e.g., skin friction and transition point location can be constrained or used as objectives. Structural characteristics can be controlled by constraining the shape in terms of coordinates, gradients and curvatures.

The 3D tool is developed for the design of the new airfoils and models a complete blade with all its airfoil sections to form the blade surface and compute the aerodynamic performance of the rotor. Gradients and curvatures in the direction from the root to the tip were included to quantify the compatibility. Also, the 3D tool opens up the possibility of maximizing the rotor power performance in terms of, e.g. the power coefficient C_P. With the 3D tool follows a graphical user interface so that information about the geometry can either be extracted for use in the optimization process or existing blades can be inspected visually and quantitatively.

6.7.1 Design algorithm

The design variables are changed in an optimization problem to minimize the objective function. This is done subject to constraints. In this case the design variables are the control points that describe the airfoil shape. The constraints are side values for the design variables and bounds on response parameters from flow and structural calculations. A traditional Simplex optimizer was used with a finite difference sensitivity analysis. This is a simple and robust solution method, which however, is computationally expensive because of the large number of necessary flow calculations. The optimization process is iterative involving numerous calculations of flow and structural response parameters where the design gradually changes to improve the objective. The calculated flow and structural response parameters are used to estimate the

value of the objective function and the constraints. Multiple angles of attack are calculated to allow off-design optimizations. The combination of flow and structural responses allows multidisciplinary optimization (MDO).

6.7.2 Geometry description

A smooth shape is important for the optimization results. The 2D airfoil shape was represented by a single B-spline defined from the trailing edge around the airfoil contour by a set of control points. The blade shape was represented by cubic B-splines fixed at the top and bottom of the 2D sections and at the leading and trailing edge. In between these four fixed points at the sections the splines were distributed evenly along the surface length. Creation of the blade is seen in Figure 70, which shows a screen dump from the 3D tool reflecting the blade planform at the top with a number of corresponding master airfoil sections with thick lines. In between the master airfoil sections are seen thin, grey lines showing the interpolated airfoil sections from the connecting curves from the root to the tip and forming the mesh. At the bottom of the screen dump is seen a 2D airfoil section in the blade.
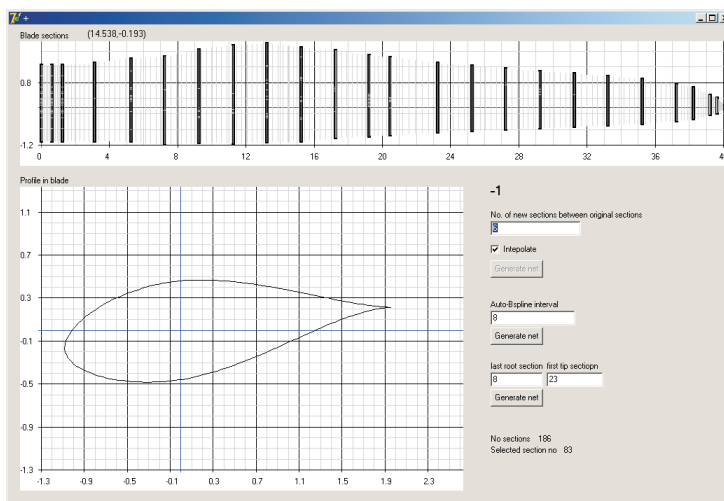

Figure 70. Screen dump of a window from the design tool showing the blade planform.

The splines creating the 2D sections and the connection between the 2D sections form a mesh from where coordinates, gradients and curvatures can be extracted and used either for inspection or for use in the optimization process.

6.7.3 Flow analysis

The XFOIL code by Drela was used for the flow calculations during the optimization [12]. For a given *AOA* and *Re*, XFOIL provides the c_p-distribution and c_l, and c_d. In addition, numerous boundary layer parameters are calculated. Transition was modeled by the e^n method with $n = 9$. Prescribing transition to 0.1% after the leading edge on the suction side and at 10% after the laeding edge on the pressure side simulated leading edge roughness. XFOIL is well suited for optimization because of the fast and robust viscid/in-viscid interaction scheme. However, the integral boundary layer formulation is not well suited for separated flows. XFOIL should therefore be used with caution at $c_{l,max}$. Others find that it may be necessary to modify or even tune XFOIL to better match measured results [3], but the computations seems to compare relatively well to EllipSys2D computations.

6.8 Strategy for airfoil design

The desirable airfoil characteristics form a complex matrix of properties of which some are in conflict with others. This has been a topic of discussion in the literature, e.g., in [16],[17] and [18]. There seems to be consensus on most of the general desirable characteristics. However, the means of achieving them are strongly related to the design method and the philosophy of the designer. The new airfoils were designed for operation on a wind turbine rotor. The force that contributes to the rotor power is the tangential force, T, whereas the force that contributes to the rotor thrust, is the normal force, N. As it was the case with Risø-B1 airfoil family T can be used as the objective function, but also the lift-drag ratio (L/D) can be used. The latter is a common measure of the airfoil efficiency because L can be considered as the production and D can be considered as the loss. The new airfoil family was designed with maximum $c_l - c_d$ ratio. Figure 71 shows in terms of a c_l vs. *AOA* plot the different characteristics that are taken into account in the design process.
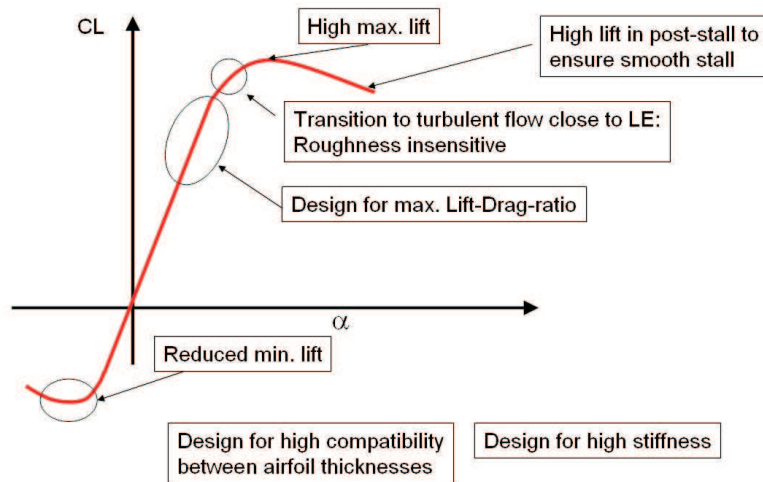
Figure 71. Sketch of the design strategy for wind turbine airfoils.

6.8.1 Structure

A wind turbine blade may be divided into the root, mid and tip parts. The mid and tip parts are determined mainly from aerodynamic requirements whereas structural objectives are relevant mainly for the inboard part of the blade, e.g., for $t/c > 24\%$. The t/c ratio is the most important parameter and also important are the location of the maximum thickness on the chord and the local shape of the airfoil. Another issue is the geometric compatibility between airfoils of the same family to ensure smooth transition from one airfoil to the other. Geometric compatibility was ensured by using the new 3D tool, where two airfoils with $t/c = 15\%$ and 24%, respectively, designed with the 2D tool, formed the basis for the remaining airfoil sections, 18%, 21% and 30%, by interpolating and even extrapolating between the two airfoils. These interpolated and extrapolated airfoils were adjusted to maximize the aerodynamical and structural performance. Because of the desire for high $c_{l,max}$ significant camber was allowed on the pressure side. The thickness of the trailing edge was kept finite but thin to minimize trailing edge noise.

6.8.2 Insensitivity of $c_{l,max}$ to leading edge roughness

Roughness in the airfoil leading edge region formed by accumulation of dust, dirt and bugs is well recognized as a main design driver for wind turbine airfoils [16]. The new airfoils

were designed for minimum sensitivity of $c_{l,max}$ to leading edge roughness by two separate design objectives: (1) The suction side natural transition point was constrained to move to the very leading edge for *AOA* around 3deg below $c_{l,max}$ predicted with forced transition. This determined the local shape of the leading edge region so that a small pressure rise at the leading edge caused natural transition to turbulent flow at the leading edge a few degrees before $c_{l,max}$. Premature transition caused by roughness will therefore be eliminated close to $c_{l,max}$ by a very forward position of the natural transition point. (2) The level of $c_{l,max}$ resulting from a flow analysis with simulation of leading edge roughness, i.e. forced transition, was constrained to a sufficiently high value compared to results from analysis with smooth flow. This shapes the airfoil suction side so that the pressure recovery region does not separate prematurely because of an increase of the boundary layer thickness caused by roughness, which would reduce $c_{l,max}$. Even with this constraint massive roughness will inevitably reduce $c_{l,max}$. Also, the existence of minor leading edge roughness will result in an unavoidable reduction in the $c_l - c_d$ ratio.

6.8.3   Design $c_{l,max}$

The airfoil sections were designed for high $c_{l,max}$. This was chosen because the airfoil sections can be used for design of slender blades and in general ensuring minimum fatigue loads and extreme loads. However, a disadvantage from this choice is the loss of stiffness for the blade if the relative airfoil thicknesses are maintained even though the chord distribution is reduced. Thus, the choice of high maximum lift is closely related to the choice of concept in the blade design. No matter which concept is used in the blade design, the inner part of the rotor needs airfoil sections with both high relative thickness and high maximum lift.

6.8.4   Design objective

A compound objective function was defined as a weighted sum of $c_l - c_d$ ratio values resulting from multiple angles of attack in the design *AOA* range. Some were for a clean airfoil surface whereas others were for flow with simulated leading edge roughness to ensure good performance at both conditions. The airfoil design *AOA*-region is also determined from the requirements to the wind turbine off-design operation. Because of the stochastic nature of the wind, turbulence gusts and wind direction changes will always lead to some off-design operation due to non uniform inflow. However, the degree of off-design is mainly given by the power control principle. In most cases it is desirable that the design *AOA*-region is close to $c_{l,max}$ since this enables low rotor solidity and/or low rotor speed. For all the new airfoils the design point region was $AOA_r \in [5°; 14°]$. This should lead to an expected high $c_{l,max}$ at around $AOA_r = 16°$ corresponding to $c_{l,max} = 1.8$ at a lift curve slope of $2\pi/rad$. The airfoil family was designed for $Re = 6 \times 10^6$, because this corresponds to the largest blade designs.

6.8.5   The Risø-C2 family

The airfoil family is seen in Figure 72. The airfoils show high compatibility between the different airfoil thicknesses. Also, a high degree of camber is seen close to the trailing edge to obtain high $c_{l,max}$.

6.9   Verified performance of the Risø-C2-18 airfoil

In the following c_l vs. c_d and c_l vs. *AOA* are shown for the Risø-C2-18 and the Risø-B1-18 airfoils which were tested in the LM Glasfiber wind tunnel. The results shown for $Re = 6 \times 10^6$. The characteristics were computed using XFOIL assuming forced transition from the very leading edge and free transition from laminar to turbulent flow. Figure 73 show the characteristics for the Risø-C2-18 airfoil with clean airfoil surface. Relatively good agreement between the
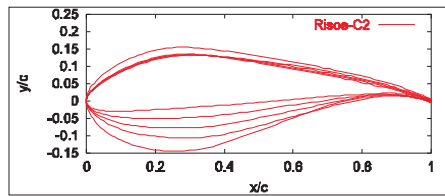
Figure 72. The Risø-C2 airfoil family.

wind tunnel test and the computations with XFOIL assuming free transition is seen. However, maximum lift seems to be reduced somewhat in the tunnel compared to the computations. Also, the transition point compared to the computations is shown and good agreement is seen.
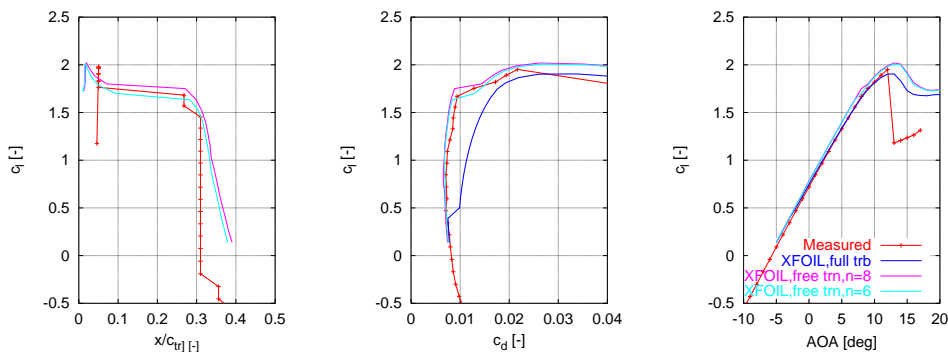

Figure 73. Left: c_l vs. transition point, Mid: c_l vs. c_d, Right: c_l vs. AOA for the Risø-C2-18 airfoil at $Re = 6 \times 10^6$ with clean surface. Also, computations with XFOIL are shown with the assumption of free transition (with $n = 6$ and $n = 8$) and forced transition from the leading edge.

The airfoil characteristics for the Risø-C2-18 and Risø-B1-18 are very similar.

Figure 74 shows the aerodynamic characteristics for Risø-C2-18 airfoil compared to Risø-B1-18. It is seen that the characteristics for the two airfoils are similar, however with the Risø-C2-18 airfoil showing significantly higher lift-drag ratio.
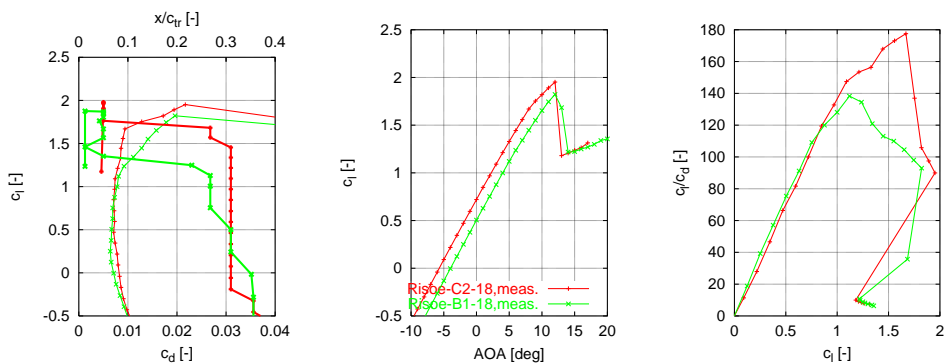

Figure 74. Left: c_l vs. c_d and c_l vs. transition point, Mid: c_l vs. AOA, Right: c_l/c_d vs. c_l for the Risø-C2-18 and Risø-B1-18 airfoils at $Re = 6 \times 10^6$ with clean surface.

Figure 75 shows the aerodynamic characteristics for Risø-C2-18 airfoil with leading edge roughness. It is seen that the leading edge roughness results in increasing drag, but the loss in $c_{l,max}$ is very limited. Also, the comparisons to the XFOIL computations show very good agreement between the assumption of forced transition from the leading edge on the suction side and the aerodynamic characteristics from tests with the leading edge roughness.

Comparing the performance of the Risø-C2-18 airfoil with the Risø-B1-18 airfoil with leading
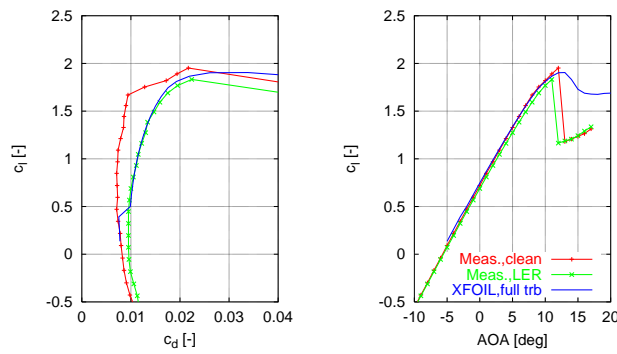
Figure 75. Left: c_l vs. c_d, Right: c_l vs. AOA for the Risø-C2-18 airfoil at Re $= 6\times10^6$ with clean surface and leading edge roughness. The measurements are compared to XFOIL computations assuming fully turbulent flow.

edge roughness, Figure 76, shows a very similar behaviour of the two airfoils, however with slightly higher $c_l - c_d$ ratio for the Risø-B1-18 airfoil for $c_l < 1.2$, but slightly higher $c_l - c_d$ ratio for the Risø-C2-18 airfoil for $c_l > 1.2$ until $c_{l,max}$. In general it is seen that the $c_l - c_d$ ratio is decreased to a value of around 100, not dependent on the $c_l - c_d$ ratio for the clean configuration. This loss in $c_l - c_d$ ratio is believed to be unavoidable. Thus, the desired insensitivity to leading edge roughness for wind turbine airfoils concerns primarily the value of $c_{l,max}$.
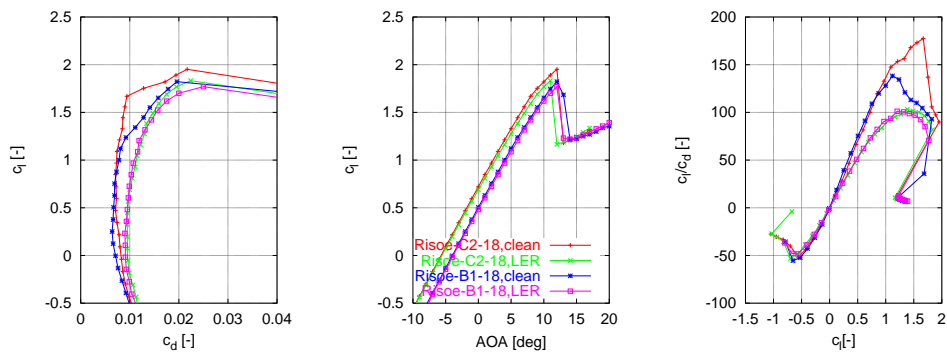

Figure 76. Left: c_l vs. c_d, Mid: c_l vs. AOA, Right: c_l/c_d vs. c_l for the Risø-C2-18 and the Risø-B1-18 airfoils at Re $= 6\times10^6$ with clean surface and leading edge roughness.

The Risø-C2-18 airfoil shows similar roughness insensitivity as Risø-B1-18.

The Risø-C2-18 airfoil is insensitive to turbulence intensity.

Figure 77 shows lift and drag for the airfoil with three levels of inflow turbulence. Concerning $c_{l,max}$ it seems that it is increasing somewhat with the level of turbulence. However, the drag is increasing with the turbulence level, which is expected. This results in a lower level of the lift-drag ratio as seen in Figure 77. The increased turbulence intensity seems to work as a kind of vortex generators.

6.10 Conclusions

This chapter presented results from the wind tunnel tests on three airfoils in the LM Glasfiber wind tunnel. Two subjects were described 1) transition detection and 2) Verification of the Risø-C2-18 airfoil compared to the Risø-B1-18 airfoil.

A large amount of microphone data has been processed with reference to transition detection and selected results are presented. All results show expected values and the method for transition detection is well established. The only drawback in the method is uncertainty with respect to the accuracy of the detected values near the leading edge. In all cases contour plots like Figure 67 shows clearly transition and also the onset of instability as well as the chord over which
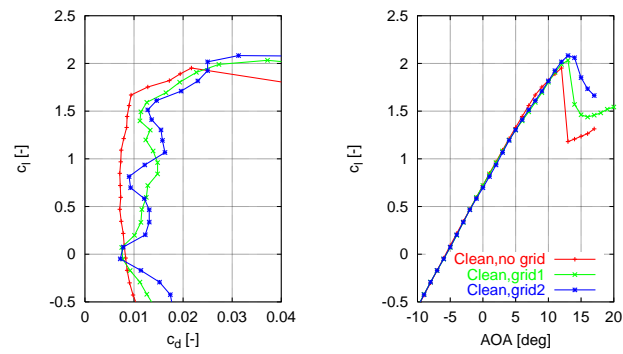
Figure 77. Left: c_l vs. c_d, Right: c_l vs. AOA for the Risø-C2-18 airfoil at Re = 6×10^6 with clean surface. Three different levels of inflow turbulence are seen in terms of no turbulence grid in the tunnel and two different turbulence grids.

transition develops.

The Risø-C2 airfoil family for wind turbines is developed considering structural stiffness and compatibility in addition to excellent aerodynamics. For this purpose the airfoil design tool AIRFOILOPT was used. AIRFOILOPT has a 3D description of the airfoils mounted on a blade and the possibility of computing gradients, curvatures and angles at the surface. Also, the design tool makes it possible to compute the rotor flow in terms of the Blade Element Momentum theory. Furthermore, a method of designing an airfoil family was developed. Two airfoils were designed without taking the 3D shape into account. They were positioned at the tip, t/c=15%, and closer to the root, t/c=24%. Interpolation and extrapolation of these two airfoils made initial guesses for the remaining airfoil thicknesses. Based on these guesses the airfoils were adjusted both aerodynamically and structurally. The airfoils were developed for variable speed operation and pitch control of large megawatt sized rotors. Design objectives were used with simultaneous use of airfoil flow simulations assuming both free and forced transition. The main design objective was to maximize $c_l - c_d$ ratio, contributing to the power efficiency of a wind turbine, over a range of design angles of attack along with numerous constraints on flow and structural response parameters to ensure a high maximum lift coefficient and insensitivity of this to leading edge roughness. An important feature of the Risø-C2 airfoils is the structural stiffness which is maximized and the high degree of compatibility subject to the high requirement to the aerodynamic characteristics.

The design of the Risø-C2-18 airfoil was verified in the LM Glasfiber wind tunnel and showed that the design criteria were fulfilled. Thus, the airfoil with clean surface showed the characteristics as predicted with the flow simulation tools, however with a slightly lower maximum lift. For example the fast movement of the transition point at around $c_l = 1.7$ showed to be predicted well by the e^n model in XFOIL. Also, an unavoidable but acceptable loss in maximum lift was seen which was at its highest up to δc_l=0.15. Furthermore, it was as expected seen that the drag was not resistant to leading edge roughness and an increase in both maximum lift and drag were seen. Testing the airfoils with different turbulence intensity showed an increase in drag and an increase in maximum lift compared to the tests at lower turbulence intensity.

References

[1] P.F. Mish. An experimental investigation of unsteady surface pressure on single and multiple airfoils. Technical report, Virginia Polytechnic Institute and State University, Virginia, USA, March 2003.

[2] Tangler J.L. and Somers D.M. Nrel airfoil families for hawt's.

[3] Timmer W.A. and van Rooij R.P.J.O.M. Summary of the delft university wind turbine dedicated airfoils. *Proc. AIAA-2003-0352*, 2003.

[4] Björk A. Coordinates and calculations for the ffaw1-xxx, ffa-w2-xxx and ffa-w3-.xxx series of airfoils for horizontal axis wind turbines. Ffa tn 1990-15, FFA, Stockholm, Sweden, 1990.

[5] P. Fuglsang and C. Bak. Development of the risø wind turbine airfoils. *Wind Energy*, 7:145–162, 2004.

[6] P. Fuglsang and K.S. Dahl. Multipoint optimization of thick high lift airfoil wind turbines. *Proc. EWEC97, Dublin, Ireland*, pages 468–471, 1997.

[7] P. Fuglsang and S. Bove. Wind tunnel testing of airfoils involves more than just wall corrections. *Proc. European Wind Energy Conference, Brussels*, March 31st April 3rd 2008.

[8] Døssing M. High Frequency Microphone Measurements for Transition Detection on Airfoils. Risø R-report ISBN 978-87-550-3674-1, Risø DTU, Wind Energy Department, 2008.

[9] Døssing M. High Frequency Microphone Measurements for Transition Detection on Airfoils - Risø B1-18 Appendix Report. Risø R-report ISBN 978-87-550-3675-8, Risø DTU, Wind Energy Department, 2008.

[10] Døssing M. High Frequency Microphone Measurements for Transition Detection on Airfoils - Risø C2-18 Appendix Report. Risø R-report ISBN 978-87-550-3676-5, Risø DTU, Wind Energy Department, 2008.

[11] Døssing M. High Frequency Microphone Measurements for Transition Detection on Airfoils - NACA-0015 Appendix Report. Risø R-report ISBN 978-87-550-3677-2, Risø DTU, Wind Energy Department, 2008.

[12] M. Drela. *XFOIL, An Analysis and Design system for Low Reynolds Number Airfoils. Low Reynolds Number Aerodynamics*, volume 54. In Springer- Verlag Lec. Notes in Eng., 1989.

[13] JA. Michelsen. Basis3d - a platform for development of multiblock pde solvers. Technical report afm 92-05, Technical University of Denmark, 1992.

[14] JA. Michelsen. Block structured multigrid solution of 2d and 3d elliptic pde's. Technical report afm 94-06, Technical University of Denmark, 1994.

[15] N.N. Sørensen. General purpose flow solver applied to flow over hills. Risø-r-827(en), Risø National Laboratory, Denmark, June 1995.

[16] J.L. Tangler and D.M. Somers. Status of the special purpose airfoil families. *Proc. WIND-POWER'87, San Fransisco*, 1987.

[17] A. Björk. Airfoil design for variable rpm horizontal axis wind turbines. *Proc. EWEC'89, Glasgow, Scotland*, 1989.

[18] P. Fuglsang. Aerodynamic design guidelines for wind turbine rotors. *Proc. 4th GRACM Congress on Computational Mechanics GRACM 2002, Patra, Greece*, 2002.

7 Comparison of Design Methods for Turbines in Wake

Author: Torben J. Larsen, Helge Aa. Madsen and Gunner C. Larsen

In this paper two different design methods are compared regarding design loads for a wind turbine operating in park configuration and thereby accounting for wakes of neighboring turbines. The first method used for calculating the fatigue and extreme loads is the prescribed method by IEC61400-1 edition 3, which basically is a method to adjust the intensity of the natural turbulence according to the park configuration and the load component observed. The second method is completely different since it uses the wind speed deficit of the upstream turbine together with a meandering process in order to simulate the incoming flowfield of the downstream turbine. The meandering process causes time periods of full, half or no wake situation - varying in time - as a result of large scale natural turbulence. This more correct implemented modelling of the physical process has previously been verified by load, inflow and wake measurements. It has also previously been seen that there are important differences in the turbine loading depending of the method chosen [1]. However, a full load base has not previously been compared regarding fatigue and extreme loads as well as power production. The meandering wake method is implemented in the aeroelastic code HAWC2 [2] and a case study performed. In this study a pitch controlled 2MW turbine is investigated for site conditions with low ambient turbulence corresponding to offshore conditions. The load cases considered are purely production cases for which the fatigue and extreme loads are calculated.

The dynamic wake meandering (DWM) model has been implemented in HAWC2 *Re*.

7.1 Introduction

This paper is to be considered as an extension of the paper by Madsen et. al. [3] where the dynamic wake meandering (DWM) model, its practical implementation and comparisons to measurements and CFD calculation is described. Where Madsen et al. [3] has focus on the model description and validation, this paper addresses the load consequences of applying the DWM model instead of the IEC model. The implementation of the DWM model described in [3] is identical to the model applied in this paper as is the chosen 2MW turbine. The load differences between the DWM and the IEC model were previously addressed in the paper by Thomsen et. al. [1] where a comparison of loads between the DWM and the IEC model was performed for mean wind speeds of 10 and 20 m/s and large differences were seen especially regarding the extreme loads for the yaw moment. The differences regarding fatigue loads were generally in the range of 20%, with less deviation for the blade loads and higher deviation for tower loads. This analysis assumed only influence of one upstream turbine combined with an assumption of rotationional symmetry and also only one stochastic turbulence seed was used for each wind direction.

In the present investigation eight surrounding turbines are included in the model (however downstream turbines are automatically neglected internally in the code), and simulations are performed for all mean wind speeds ranging from 8 to 26 m/s. Influence of wind direction is investigated with a two degrees step, and to take influence of statistical uncertainty into account, six different stochastic seeds are used for each parameter setting leading to a total of 2760 simulations used for the DWM analysis. Originally, simulations covering the mean wind speeds 4 and 6 m/s were also included, but negative wind speed could suddenly cover the rotor causing numerical problems in combination with the induction model. These low wind speeds are therefore excluded in the present analysis and they are in general considered to contribute only marginally to the total load. More work will be addressing this issue in the future.

7.2 Wind farm configuration

As illustrated in Figure 78 a park configuration with equal row spacing is assumed. Influence of the 8 surrounding turbines are taken into consideration. However due to symmetry reasons, only wind directions from 0 to 44 deg are investigated causing only wake influence from the three left turbines (down wind placed turbines are ignored automatically as mentioned previously). Two spacing configurations are investigated with 3 and 8 diameter distance, respectively.
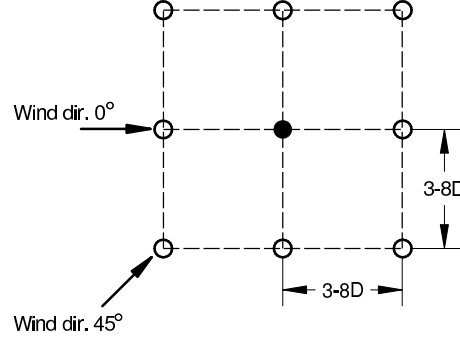

Figure 78. The wind farm layout is a quadratic grid with distance of 3 and 8D spacing.

7.3 Methods - the IEC model

The method of equivalent turbulence originally formulated by Frandsen [4] forms the basis of an informative annex in the recent IEC standard [5]. In the method of equivalent turbulence, the effects of all load generating mechanisms are condensed into a modification of the intensity of the free flow turbulence. The method has primarily been calibrated in order to obtain correct values for flapwise blade bending fatigue loads. For a uniform wind directional distribution, the effective turbulence intensity can be calculated as:

$$I_{eff} = \frac{1}{V_{hub}} \left[(1 - N p_w)\sigma^m + p_w \sum_{i=1}^{N} \sigma_T^m d_i \right]^{\frac{1}{m}} \tag{30}$$

where V_{hub} is the average wind speed at hub height, N is the number of neighbouring wind turbines, p_w is the probability density function of the wind direction (for a uniform distribution, $p_w = 0.06$ is used), and m is the relevant material SN-exponent. σ is the ambient wind speed standard deviation, and σ_T is the maximum centre-wake wind speed standard deviation calculated as:

$$\sigma_T = \sqrt{\frac{0.3 V_{hub}}{1.5 + 0.3 d_i \sqrt{\frac{V_{hub}}{c}}} + \sigma^2} \tag{31}$$

where d_i is the distance to neighbouring turbines normalized by the rotor diameter, and $c = 1 m/s$. More details on the model are given in references [4] and [5]. The used turbulence intensities can be seen in Figure 79.

7.4 Methods - the DWM model

The Dynamic Wake Meandering (DWM) model complex is based on the combination of three corner stones: 1) modeling of quasi-steady wake deficits, 2) a stochastic model of the down wind wake meandering, and 3) added wake turbulence. The wake meandering part is based on a fundamental presumption stating that the transport of wakes in the atmospheric boundary layer can be modeled by considering the wakes to act as passive tracers driven by the
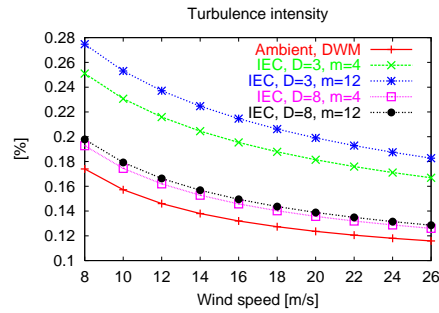
Figure 79. Used turbulence intensities for the DWM and IEC method.

large-scale turbulence structures. Modeling of the meandering process consequently includes considerations of a suitable description of the "carrier" stochastic transport media as well as of a suitable definition of the cut-off frequency defining large-scale turbulence structures in this context. For the stochastic modeling of wake meandering, we consider a wake as constituted by a cascade of wake deficits, each "emitted" at consecutive time instants in agreement with the passive tracer analogy [6], [7]. We then subsequently describe the propagation of each of the emitted wake deficits, and the collective description of these thus constitutes the wake meandering model. Adopting Taylor's hypothesis, the down-stream advection of these is assumed to be controlled by the mean wind speed of the ambient wind field. With this formulation the wake momentum in the direction of the mean flow is invariant with respect to displacement. This is a considerable simplification allowing for a straight forward decoupling of the wake along the wind deficit profile (and its expansion) and the wake transportation process. As for the dynamics in the lateral- and vertical directions, each considered wake cascade-element is displaced according to the large-scale lateral- and vertical turbulence velocities at the position of the particular wake cascade element at each time instant. The choice of a suitable stochastic turbulence field, that in turn defines the stochastic wake transport process, is not mandatory, but may be guided by the characteristics of the atmospheric turbulence at the site of relevance. These characteristics encompass, in principle, not only turbulence standard parameters such as turbulence intensity, turbulence length scale and coherence properties, but also features like degree of isotropy, homogenity of the turbulence, Gaussianity of the turbulence etc.. The meandering mechanism in the DWM model has been successfully verified by correlating DWM predictions with direct full-scale measurements of the instantaneous wake position obtained from LiDAR recordings [8].

7.5   Results - influence of wind direction

Results showing selected loads as function of wind direction is shown in Figure 80 for the 3D configuration and in Figure 81 for 8D. In these figures main loads for tower, shaft and blades are represented.

Starting with the 8D configuration the wake effects are clearly seen causing high variations in loads depending on the wind direction. At wind directions of 17-30° (the free direction) the turbine experiences no or very limited influence from wake effects, where a high contribution to loads are seen especially for half wake situation in the wind direction interval 5-10° and 35-45°. The variation in fatigue loads for the tower is a factor of 2.5 between the highest and lowest loaded wind direction, where the same factor is of the size of 1.5 for yaw, shaft and blade loads. When the downstream turbine operates in full wake condition the loads are less severe than in half wake. The same variation in max-min loads are also seen in the statistics shown to the right in Figure 81, except for the shaft torsion loads where there is less sensitivity regarding wind direction. The variation in mean level is also shown, where the most visible variation is associated with the mean level of the driving torque which also represents the variation in

power. A reduction of 30% is seen from free flow to full wake. The mean level variation for the rest of the sensors are in the range of 10-20%.

Looking at the similar results for the 3D configuration in Figure 80 a completely different variation pattern of the loads are seen. Specifically, it is the lack of variation that is interesting. For the flapwise bending moment very little variation is seen for the fatigue loads, clearly indicating that the turbine *never experiences any free flow condition*. When the wind direction is 23°, which normally is the free flow situation, the wake loaded turbine is either in a half wake situation of the one or the other upstream turbines. This effect is only seen because the wake source is modeled for several turbines simultaneously using the same meandering turbulence field, hence the meandering paths of the individual wakes are correlated. This (lack of) variation effect is also seen for the other sensors, but maybe not as pronounced as for the flapwise blade bending. The variation in fatigue loads, due to the change in wind direction, is in the size of 30% for the tower loads and 10-20% for the rest of the sensors. Regarding the max-min statistics also smaller variations are seen than for the 8D case.

When comparing the results between the 3D and 8D configurations, Figure 80 and Figure 81, it is not surprising that the flapwise blade bending loads are smaller for the 8D case than the 3D. It is especially the wind directions corresponding to free flow that causes the largest differences between the two configurations, since the 8D situation has free flow and the 3D does not. The loads are of the same size for full or half wake operation. What is more interesting is that it seems to be consistent, that the *tower loads in the longitudinal direction are larger for larger downstream distances*. This can be seen when comparing the tower loads for the 8D and 3D case, but also looking only at the 3 or 8D plot there is higher loads for wind direction of 35° than 5° which is the half wake situation from the most distant turbine. At first hand this might seem unphysical, since the depth of the velocity deficit is much more smooth for large distances, but the reason is the meandering process. If two turbines are located close to each other, the down wind turbine will mainly be in permanent full, half or no wake conditions, since the meandering path has hardly had any time to develop. For larger spacing the meandering path causes the downwind turbine to be in a mixing state between full, half and no wake conditions which is especially damaging to the tower. Clearly there must be a distance at which the tower loads will be reduced, but from this exercise it seems to be beyond 8 diameters.

7.6 Results - comparison of loads

The comparison of loads between the DWM and IEC simulations are shown in Figure 82 and 83 for the 3D and 8D case, respectively. Starting with the 3D situation the loads are comparable within 30% difference depending on the observed load component. The IEC loads are conservative regarding fatigue and extreme loads for the yaw, driving torque and flapwise bending, whereas the loads on tower and blade torsion are non-conservative. The extreme tower bending is 20% higher for the DWM model and 55% higher for the blade torsion moment. For all load components the fatigue loads of the IEC method are higher for high wind speeds, whereas the DWM model causes large loads at lower wind speeds where wake effects are most dominating.

The DWM model computes higher tower loads than the IEC model *Re*.

Regarding the 8D case the comparison shows a generally good agreement between the two models with respect to yaw, driving torque and flapwise blade bending with deviances in the size of 10%. However, for the tower loads and blade torsion a significantly higher load level is seen with the DWM model. Regarding tower loads the fatigue level is 25% higher with the DWM model and the maximum bending moment is 60% higher than for the IEC model. A similar difference is also seen for the blade torsion.

7.7 Conclusion

A new implementation of the Dynamic wake meandering model has been demonstrated, where all wake sources from the neighboring turbines are included. Production cases have only been

considered and ambient turbulence corresponding to a terrain class IC (high wind, low turbulence) has been applied. A comparison of loads between turbines with a row distance of 3 and 8 diameters respectively has been investigated with the DWM model and the method according to the IEC 61400-1 ed 3. standard. The simulations performed for very low wind speeds (<8m/s) were however excluded in the analysis due to problems with the induction model in HAWC2 when negative wind speed occurred on the downstream rotor, which is considered to be of minor importance to the results.

When comparing the loads between the 3D and 8D configuration, the turbine at the 3D configuration never experiences any free flow situation. Another interesting observation is that the tower loads seem more affected at longer downstream positions than when turbines are close to each other. This effect is addressed to the meandering effect causing higher states of full, half and no wake situation when the meandering has had time to develop.

In the direct comparison between the DWM and the IEC model for the 3D case, the IEC model seems conservative regarding fatigue and extreme loads for the yaw, driving torque and flapwise bending, whereas the loads on tower and blade torsion are non-conservative. The maximum tower bending is 20% higher for the DWM model and 55% higher for the blade torsion moment.

For the 8D case, the comparison shows a generally good agreement between the two models regarding yaw, driving torque and flapwise blade bending with deviances in the size of 10%. However, for the tower loads and blade torsion a significantly higher load level is seen with the DWM model. Regarding tower loads the fatigue level is 25% higher with the DWM model and the maximum bending moment is 60% higher than for the IEC model. A similar difference is also seen for the blade torsion.
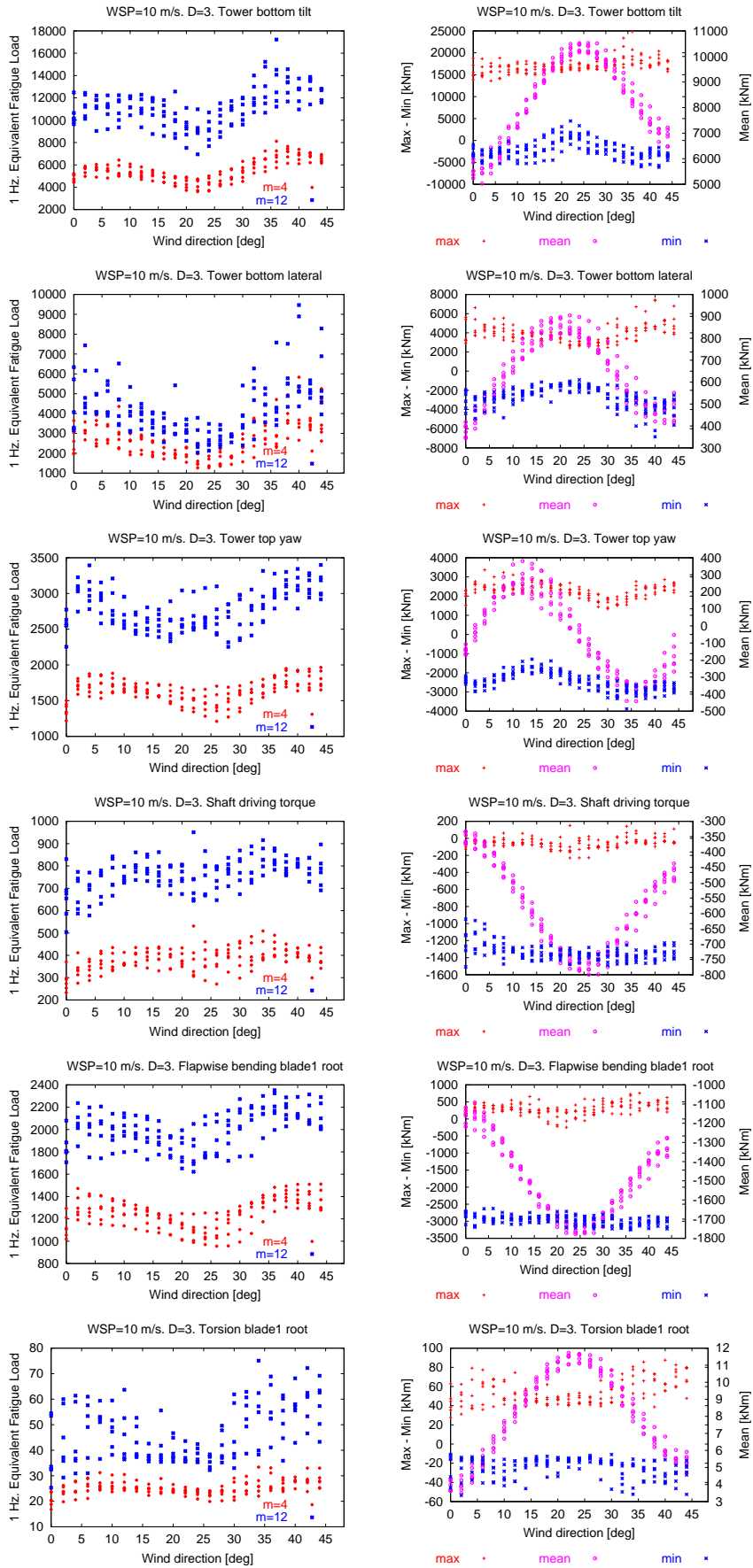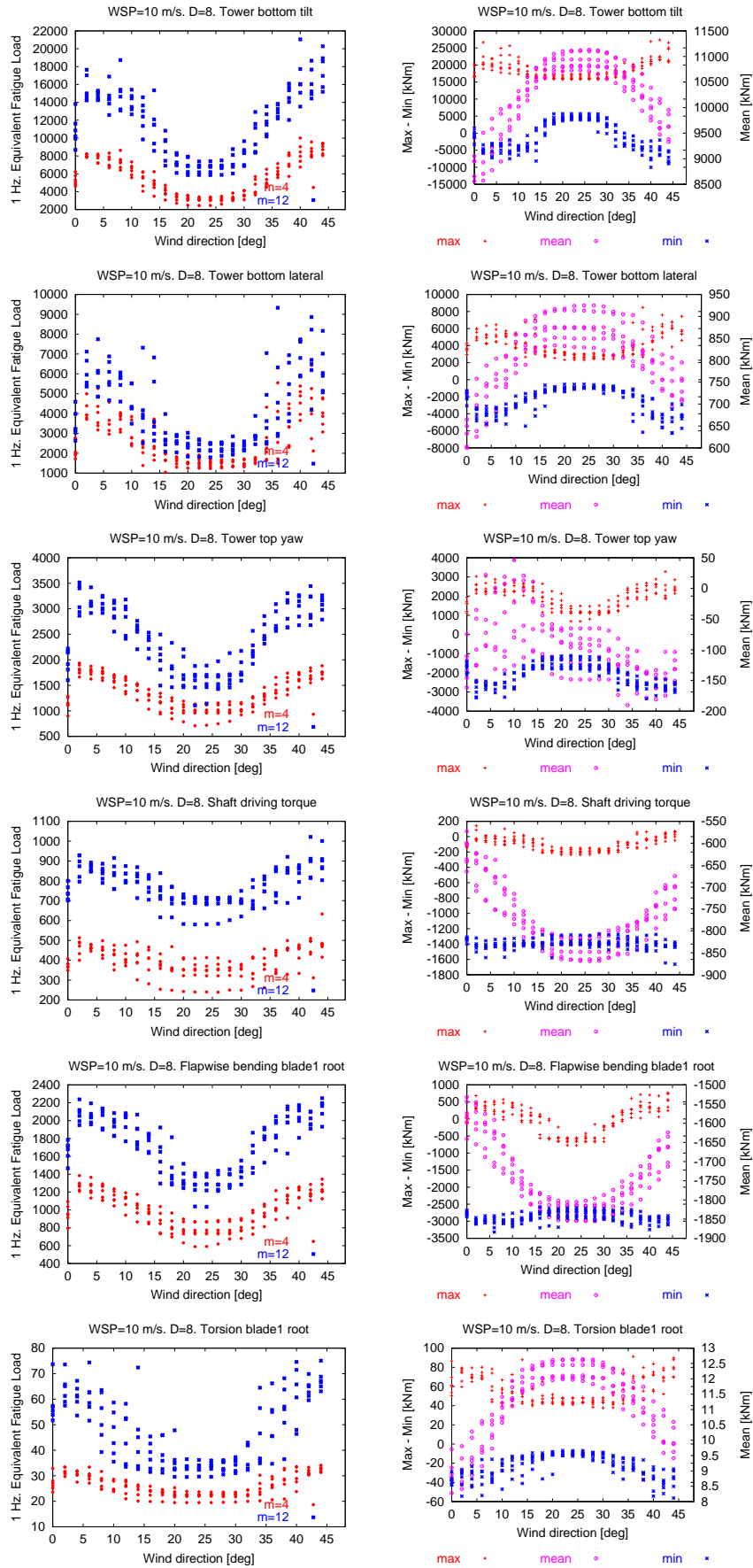
Figure 80. Influence of wind direction with spacing D=3.
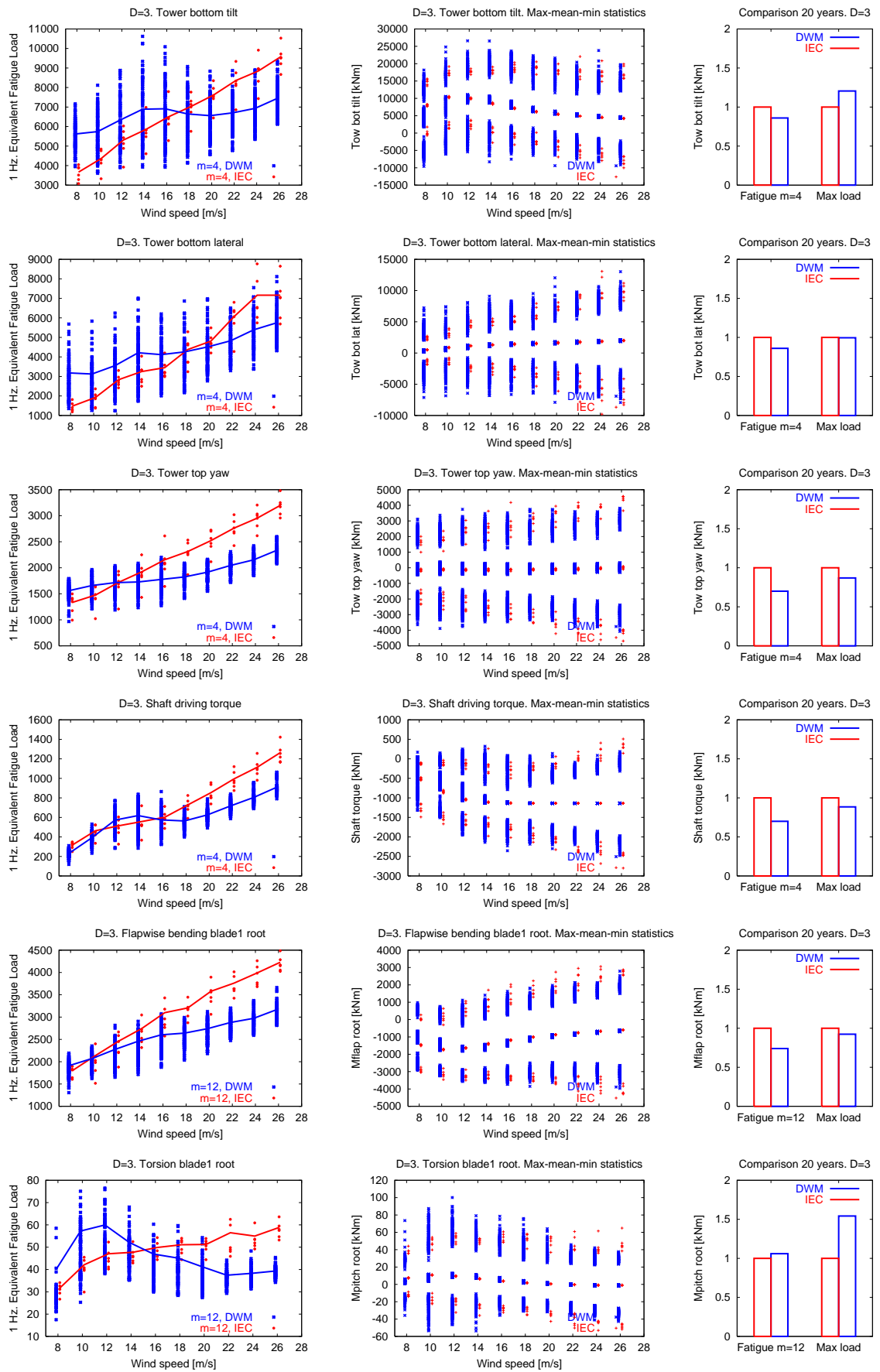
Figure 81. Influence of wind direction with spacing D=8.
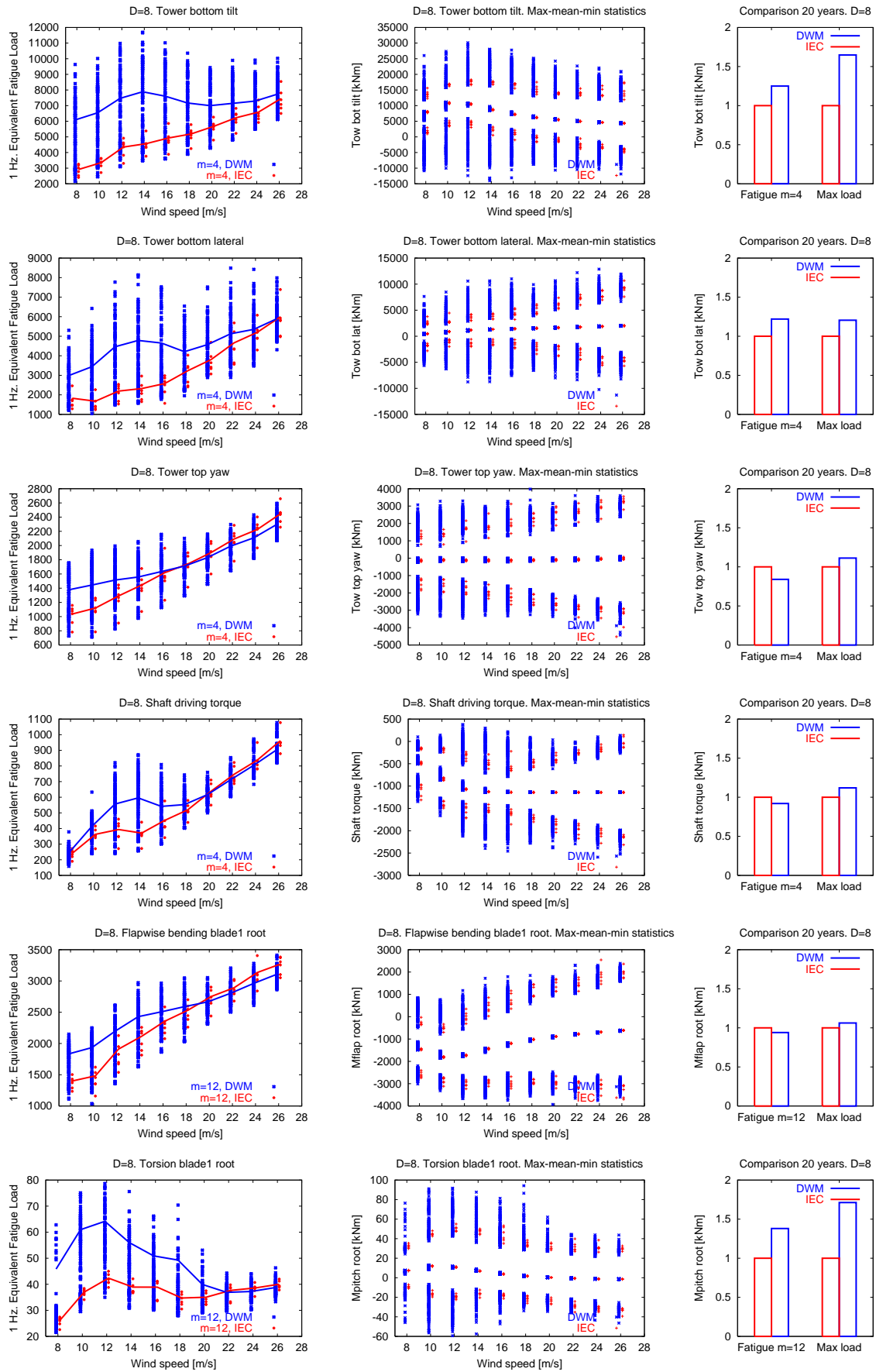
Figure 82. Fatigue and statistics for D=3.

Figure 83. Fatigue and statistics for D=8.

References

[1] K. Thomsen, H. A. Madsen, Larsen G.C., and Larsen T.J. Comparison of methods for load simulation for wind turbines operating in wake. *Journal of Physics: Conference Series*, 75, 2007. doi:10.1088/1742-6596/75/1/012072.

[2] T. J. Larsen and A.M. Hansen. How to HAWC2, the users manual. Technical Report Risø-R-1597(en), Risoe National Laboratory - Technical University of Denmark, December 2007.

[3] H.A. Madsen, Larsen G.C., Larsen T.J., R. Mikkelsen, and N. Troldborg. Wake deficit-and turbulence simulated with two models compared with inflow measurements on a 2MW turbine in wake conditions. In *Proceedings of the international wind energy conference held in Brussels*. EWEA, 2008.

[4] S. Frandsen. Turbulence and turbulence-generated structural loading in wind turbine clusters. Technical Report Risø-R-1188(EN), Ris-DTU, 2005.

[5] Wind turbines Part 1: Design requirements. Technical report, International electrotechnical commission, 2005.

[6] G. C. Larsen, H. Aa. Madsen, K. Thomsen, and T. J. Larsen. Wake meandering - a pragmatic approach. *Accepted for publication in Wind Energy*.

[7] K. Thomsen, H. Aa. Madsen, and S. M. Markilde. Wind Turbine Wake Data from Inflow Measurements using a Five Hole Pitot Tube on a NM80 Wind Turbine Rotor in the Tjreborg Wind Farm. Technical Report Risø-I-2108(EN), Risoe National Laboratory, 2003.

[8] G. C. Larsen, H. Aa. Madsen, F. Bingöl, J. Mann, S. Ott, J.N. Srensen, V. Okulov, N. Troldborg, M. Nielsen, K. Thomsen, T.J. Larsen, and R. Mikkelsen. Dynamic wake modeling. Technical Report Risø-R-1607(EN), Risoe National Laboratory - Technical University of Denmark, 2007.

8 Some Nonlinear Effects on the Flutter Speed and Blade Stability

Author: Morten H. Hansen and Bjarne S. Kallesøe

This chapter deals with two different nonlinear effects on the stability of a blade. This work has been performed under the milestone "Aero-servo-elastisk pitch dynamik for vinger med store udbøjninger" of the EFP-2007 project.

First, the effects of large bending deflections under steady state operation of the wind turbine blade on its stability limits, especially with regards to the flutter limit, are analyzed.

Politis and Riziotis [1] have shown the importance of nonlinear effects identified by aerodynamic and aero-elastic simulations on the 5 MW Reference Wind Turbine (RWT) [2]. Their results show that the curvature of a blade with large flapwise bending under the aerodynamic loading leads to a coupling of blade torsion to the edgewise bending. The blade torsion, and therefore the angle of attack along the blade, are increased near the rated speed by this coupling, which again causes the a higher thrust and mean flapwise deflections. Their aeroelastic simulations also show that the fatigue loads for blade root flapwise and edgewise moments are almost unaffected, whereas the extreme values of the torsion moment are increased.

The coupling of bending and torsion due to large blade bending are also assumed to have some effects of the flutter limits of wind turbines, as discussed in [3]. In the present report, the aeroelastic blade model suggested by Kallesøe [4], which is similar to the second order model used in [1], is used to investigate the aeroelastic stability limits of the RWT blade with and without the effects of the large blade deflection. The investigation shows no significant change of the flutter limit on the rotor speed due to the blade deflection, whereas the first edgewise bending mode becomes negatively damped due to the coupling with torsion. These observations are confirmed by nonlinear aeroelastic simulations using HAWC2 [5, 6].

To evaluate the validity of this analysis, the bending–torsion coupling due to pre-bending is investigated for a simple prebent test blade in the following subsections by computing the structural mode shapes using three different structural models.

Second, the effect of a free-play in the pitch system is analyzed. A linear pitch bearing stiffness with a free-play are imposed on a 2D wing-section model with flapwise, edgewise and torsional degrees of freedom, including both dynamic and steady state effects of pitch changes, suggested by Kallesøe [7]. The pitch system model and the wing-section model are combined into an autonomous system, which is subject to time simulations for determine steady state conditions. It is found that the flutter speed decrease when a free-play is introduced.

8.1 Effect of bending–torsion coupling due to pre-bending

The edgewise bending–torsion coupling effects of flapwise prebent on selected blade modes are investigated in this section using three different models. First, the second order Bernoulli-Euler (BE) beam theory model by Kallesøe [4] used in the subsequent flutter analysis. Second, the preliminary co-rotational finite beam element model [8] implemented in HAWCStab2 (new version of the stability tool HAWCStab [9]). Third, a solid 3D finite element model set up in the commercial tool COMSOL. Effects of the flapwise pre-bending are observed as edgewise bending–torsion coupling in the edgewise and torsional mode shapes. Qualitative agreements are seen for these effects predicted by the three different models, except that the edgewise bending component in the torsional mode is significantly smaller in the predictions by the second order BE model compared to the other two models.
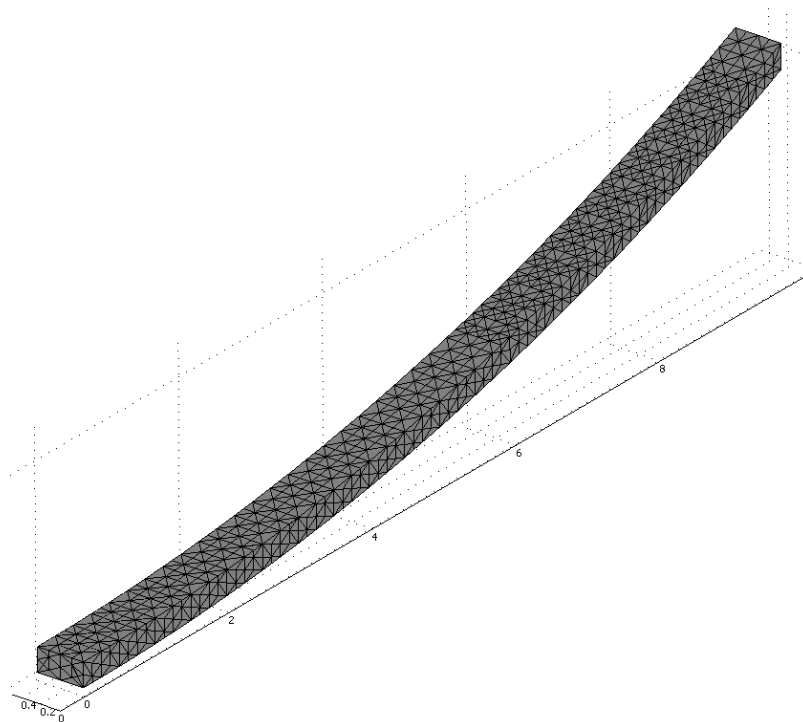
Figure 84. COMSOL model with 9,236 tetrahedral elements and 45,456 degrees of freedom which are sufficient for convergence of natural frequencies and mode shapes of the lower order modes. The 10 m test blade has squared prebent shape with 2 m tip deflection.

8.1.1 Simple test blade

A 10 m long, prismatic, and isotropic beam is used as a test blade. The cross-section has a aspect-ratio of 2, and the height of 0.245 m is selected such that the straight beam has a natural frequency of the first flapwise bending mode of 1 Hz with $E = 50$ GN/m^2 and Poisson's ratio of 0.33 (note that the first edgewise bending mode has a natural frequency of 2 Hz). The beam has squared prebent shape with 2 m tip deflection (keeping a curve length of 10 m) as shown in Figure 84, which shows the grid of the solid 3D finite element model set up in COMSOL.

Comparison of mode shapes   The first ten mode shapes of the prebent test blade have been computed by all three models; however, only the first three edgewise bending modes (numbers 2, 4, and 6) and the first torsional mode (number 8) are considered here, because the remaining flapwise bending modes are trivial by having no edgewise bending or torsional components in their mode shapes. The purely flapwise pre-bending of the test blade furthermore limits the comparisons of edgewise bending and torsional components, because all models agree that no flapwise bending arises due to edgewise bending or torsion of such prebent blade.

Figure 85 shows the normalized edgewise bending and torsional components in the first edgewise bending mode. The three models agree on the edgewise component, whereas the second order BE model predicts a lower torsional component than the other two models. All models agree on the qualitative behavior that the *forward* edgewise motion of a *downwind* bend blade is coupled to torsion towards *lower* angles of attack.

Figure 86 shows the normalized edgewise bending and torsional components in the second edgewise bending mode. Again, there is a qualitative agreement between the three models; note that the torsional component is most larger for the second edgewise bending mode. The co-rotational model (HAWCStab2) predicts a larger torsional component than the other two models, and the smallest torsional component is again for the second order BE model.
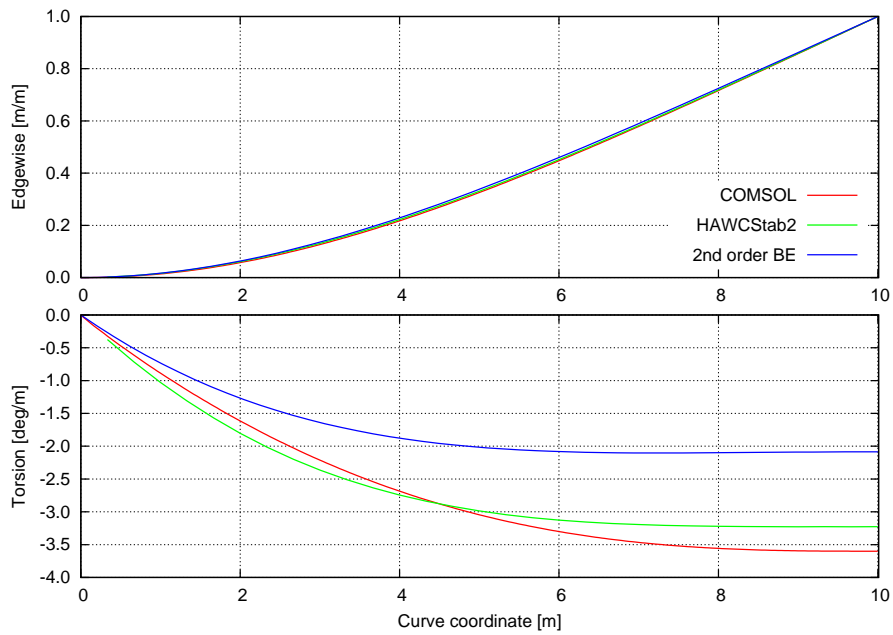
Figure 85. Edgewise bending (top) and torsional (bottom) components in the second blade mode of flapwise prebent 10 m blade computed by COMSOL model (2.02 Hz), HAWCStab2 (1.96 Hz), and second order BE model (2.02 Hz).
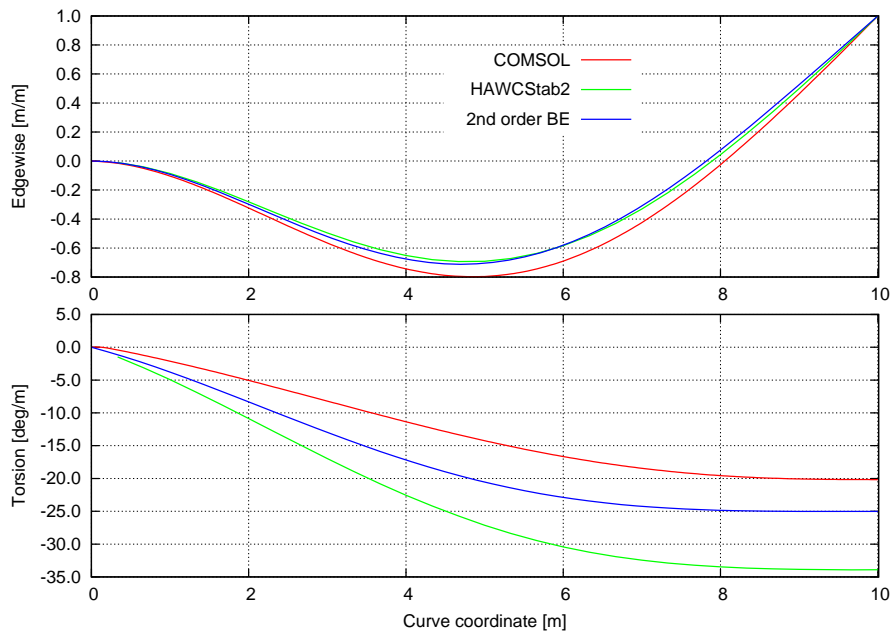

Figure 86. Edgewise bending (top) and torsional (bottom) components in the fourth blade mode of flapwise prebent 10 m blade computed by COMSOL model (11.72 Hz), HAWCStab2 (11.67 Hz), and second order BE model (12.45 Hz).

Figure 87 shows the computed normalized edgewise bending and torsional components in the first torsional mode. Here, the qualitative agreement is restricted to the HAWCStab2 and COMSOL predictions. There are almost no edgewise bending component in the torsional mode computed with the second order BE model. This surprising discrepancy to the other two models is still under investigation.

Figure 88 shows the computed normalized edgewise bending and torsional components in the

third edgewise bending mode. Here, the qualitative (and even quantitative) agreement between the three models is restored, which eliminates higher order effects as explanation for the discrepancy for the torsional mode.
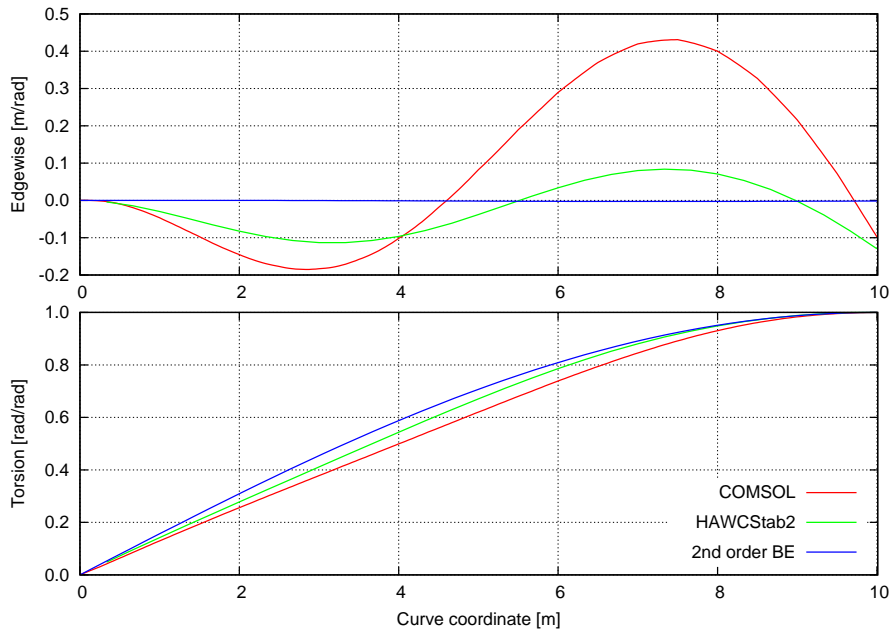

Figure 87. Edgewise bending (top) and torsional (bottom) components in the sixth blade mode of flapwise prebent 10 m blade computed by COMSOL model (29.95 Hz), HAWCStab2 (29.67 Hz), and second order BE model (31.25 Hz).
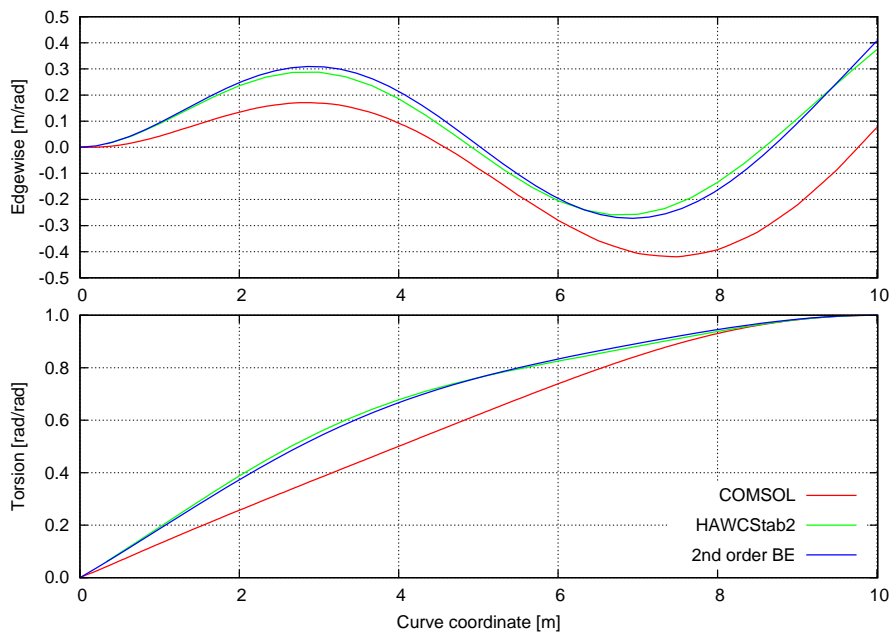

Figure 88. Edgewise bending (top) and torsional (bottom) components in the eighth blade mode of flapwise prebent 10 m blade computed by COMSOL model (35.99 Hz), HAWCStab2 (36.15 Hz), and second order BE model (34.87 Hz).

8.1.2 Stability of the RWT blade

The effect of blade deflection on the aeroelastic stability is analyzed by comparing the aeroelastic modes of blade motion with and without the blade deflection due to the mean steady state aerodynamic forces. These aeroelastic modes are computed for zero pitch angle and a series of rotor speeds and corresponding wind speeds are analyzed (see Table 8.1.2). The wind speed at the different rotor speeds are chosen such that the angles of attack stay low and almost constant.

A nonlinear steady state version (no dynamic terms) of the second order Bernoulli-Euler model coupled with a Blade Element Momentum model is used to compute steady state blade deformations under the assumption of constant inflow (no shear or tower effects) and no gravity. The full dynamic nonlinear model is then linearized about this steady state deformation to form a differential eigenvalue problem, which gives the aeroelastic frequencies, damping and mode shapes for the deformed blade (see all details in [4]). Similar, the full dynamic nonlinear model is linearized about the initial blade, which leads to the aeroelastic frequencies, damping and mode shapes for the undeformed blade.

The nonlinear model is linearized about the steady state deformed blade, which leads to the aeroelastic frequencies, damping and mode shapes for the deformed blade.

To check the results of the eigenvalue analysis, the same series of rotor speeds and wind speeds are also simulated with HAWC2 [5, 6] for zero pitch angle. The damping of the least damped mode is then estimated by the exponential decay/growth of the initial blade oscillation.

Results   Figure 89 shows the tip deflection for the different operation conditions given in Table 8.1.2. The flapwise deflection become relative large for a blade length of 63 m as the rotor speed increase.

Figure 90 shows the aeroelastic frequency for the first five blade modes under the different operation conditions (Table 8.1.2) for the undeformed and deformed blade, and the dominant frequency of the transient response in the nonlinear aeroelastic simulation with HAWC2. Figure 91 shows the corresponding aeroelastic damping, except for the first and second flapwise bending modes which are highly damped and therefore not shown.

The third flapwise bending mode (the fourth mode) becomes a flutter mode around 2.35 rad/s for both the deformed and undeformed blade. This result indicates that the large blade deflection has no significant effect on the flutter limit.

Rotor speed [rad/s]	Wind speed [m/s]
1.0	3.8674
1.1	4.2541
1.2	4.6409
1.3	5.0276
1.4	5.4144
1.5	5.8011
1.6	6.1878
1.7	6.5746
1.8	6.9613
1.9	7.3481
2.0	7.7348
2.1	8.1215
2.2	8.5083
2.3	8.8950
2.4	9.2818
2.5	9.6685

Table 4. Rotor speed and corresponding wind speeds used in the flutter analysis.

The second edgewise bending mode (the fifth mode) is significantly lower damped for the deformed blade than for the undeformed blade, which can only be explained by the increased torsional component in this edgewise bending mode due to the curvature of the flapwise blade deflection.

The first edgewise bending mode (the second mode) becomes negatively damped for rotor speeds above 1.5 rad/s when including deformations, while it stays positive damped for the undeformed blade. The HAWC2 simulations showing the dominant response (lowest damped mode) in its transients agree well with the results from the deformed blade. Notice the abrupt decrease of the damping of these transient at the rotor speed of 2.3 rad/s where the second order BE model predicts the flutter to occurs, which indicates that the HAWC2 simulations also confirms this flutter limit.

To understand the negative aeroelastic damping of the first edgewise bending mode for the deformed blade, the amplitudes and phases for the edgewise, flapwise and torsional components of this mode are plotted in Figure 92 and 93 for the undeformed and deformed blade. The phases between edgewise and flapwise blade motion are seen to shift sign for the rotor speed where the damping of the mode becomes negative. The change of sign on the phase between edgewise and flapwise blade motion corresponds to a change of the direction of vibration as shown in Figure 94. The coupling of the edgewise bending with blade torsion creates an aerodynamic coupling to between edgewise and flapwise bending through the lift–torsion coupling. The direction of vibration is related to the aerodynamic damping, and it is assumed that the negative aeroelastic damping of the first edgewise bending mode for the deformed blade is caused by this phase
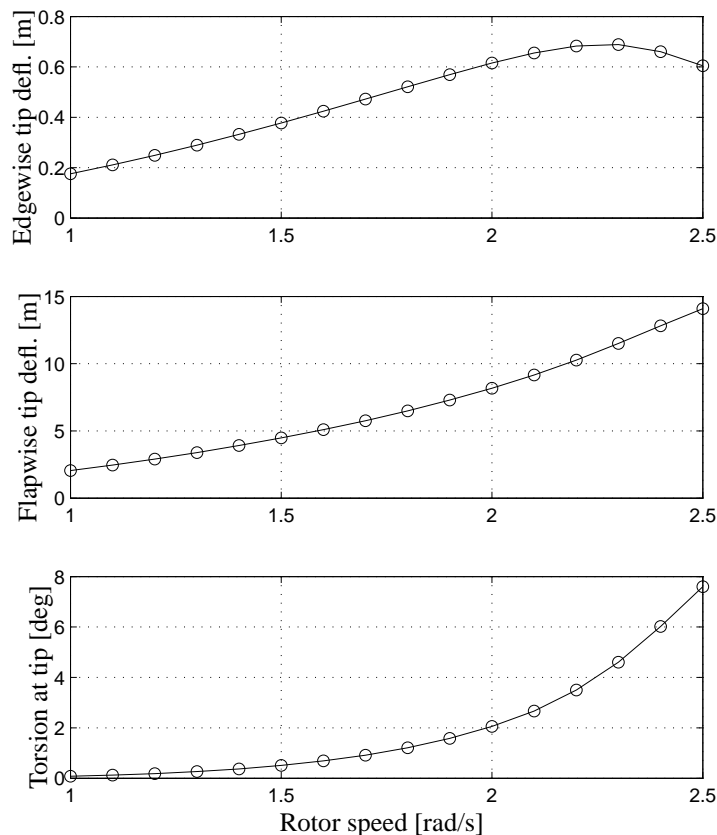

Figure 89. Tip bending deflection and torsion under steady state conditions versus rotor speed.
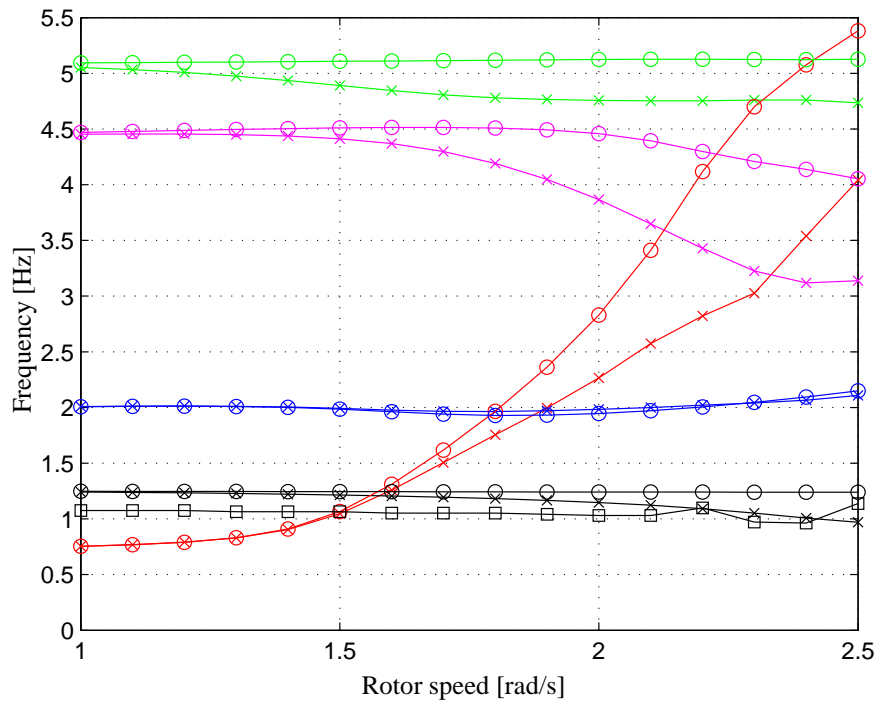
Figure 90. Aeroelastic frequencies of first flapwise (red), first edgewise (black), second flapwise (blue), third flapwise (magenta), and second edgewise (green) modes versus rotor speed. The circles (○) denote frequencies for the undeformed blade, and the crosses (×) denote results for the deformed blade. The black boxes (□) denote the dominant frequency of the transient response in the nonlinear aeroelastic simulation with HAWC2.
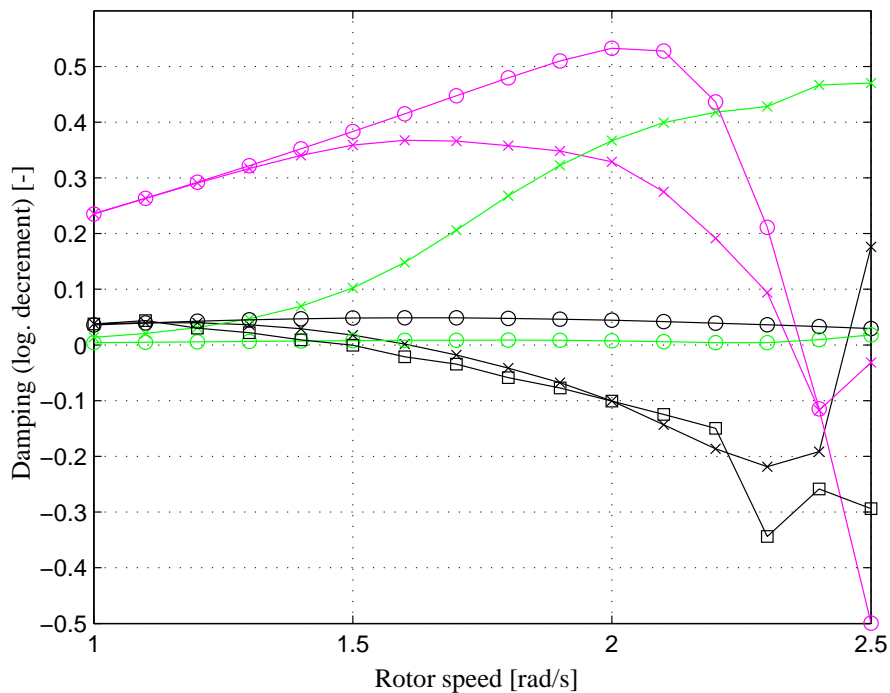

Figure 91. Aeroelastic damping of first edgewise (black), third flapwise (magenta), and second edgewise (green) modes versus rotor speed. The circles (○) denote frequencies for the undeformed blade, and the crosses (×) denote results for the deformed blade. The black boxes (□) denote the dominant frequency of the transient response in the nonlinear aeroelastic simulation with HAWC2.

8.2 Effect of Free-play in the Pitch System

The effect of a free-play in the pitch system is analyzed by the use of the 2D wing-section model suggested in [7], which includes the edgewise and flapwise bending, and torsional degrees of freedom for the section, and the pitch degree of freedom of the pitch system. Figure 95 shows the wing-section model with location of center of gravity and elastic axis about which the section is assumed to rotated in torsion. The stationary and dynamic effects of pitch angle variations are included in both the structural and aerodynamic models.

The structural equations of motion is given by

$$\ddot{\mathbf{x}} = \mathbf{f}_{struc}(\mathbf{x}, \dot{\mathbf{x}}, \beta, \dot{\beta}, \ddot{\beta}, V_t, V_n | \mathbf{P}_{struc}) \tag{32}$$

where β is the pitch angle, and the vector $\mathbf{x} = [x, y, \theta]^T$ contains the edgewise (x), flapwise (y), and torsional (θ) deflection of the wing-section, respectively. Model parameters, such as section mass, location of center of gravity, etc., are given by $\mathbf{P}_{struc}$.

The unsteady aerodynamic is described by a dynamic stall model [10] formulated as

$$\dot{\mathbf{z}} = \mathbf{f}_{aero}(\mathbf{z}, \mathbf{x}, \dot{\mathbf{x}}, , \ddot{\mathbf{x}}, \beta, \dot{\beta}, \ddot{\beta}, V_t, V_n | \mathbf{P}_{aero}) \tag{33}$$

where $\mathbf{z} = [z_1, z_2, z_3, z_4]^T$ are the aerodynamic states, two describing the effect of shed vorticity (the Theodorsen effect) and two describing the effect of the trailing edge separation. Aerodynamic parameters, such as lift data, time constants etc., are given by $\mathbf{P}_{aero}$

The effect of the aerodynamic forces and structural motion on the pitch system is described by

$$\ddot{\beta} = f_{pitch}(\dot{\beta}, \beta, \mathbf{x}, \dot{\mathbf{x}}, \ddot{\mathbf{x}} | \mathbf{P}_{pitch}) + M_\beta \tag{34}$$

where f_{pitch} describes the effect from the wing section on the pitch system, M_β is the actuator moment from the pitch system, and $\mathbf{P}_{pitch}$ holds parameters describing the transfer function from wing-section motion to pitch moment, such as stiffness and damping.

The pitch system is assumed to give a linear restoring force with a free-play at zero restoring force

The pitch system is assumed to give a linear restoring force with a free-play at zero restoring force. Figure 96 shows the pitch moment M_β in a case of 0.2 deg free-play.

Combination of (32), (33) and (34) into one set of equations, and assumption of constant wind speeds $[V_n, V_t]$, the system is autonomous and can be written as

$$\dot{\mathbf{y}} = \mathbf{f}(\mathbf{y} | V_t, \mathbf{P}) \tag{35}$$

where $\mathbf{y} = [x, y, \theta, \beta, z_1, z_2, z_3, z_4, \dot{x}, \dot{y}, \dot{\theta}, \dot{\beta}]^T$ holds the states and $\mathbf{P}$ holds all model parameters except for the relative inflow speed V_t.

Results For different relative inflow speeds V_t, the autonomous system (35) is simulated until it reach as a steady state where the amplitude of the oscillations either become zero or settles with a finite amplitude. The flutter speed is assumed to be the relative inflow speed when the steady state amplitudes are distinguishably larger than the zero amplitudes of the normal steady state solution.

The introduction of a free-play decrease the flutter speed.

Figure 97 shows at which wind speeds the amplitude of oscillations of the wing section begins to increase rapidly, indicating the flutter limit. It is seen that the introduction of a free-play decrease the flutter speed.

8.3 Conclusion

This chapter deals with nonlinear effects on the stability of a wind turbine blade. This work has been performed under the milestone "Aero-servo-elastisk pitch dynamik for vinger med store udbøjninger" of the EFP-2007 project.

First, the effects of large bending deflections under steady state operation of the wind turbine blade on its stability limits, especially with regards to the flutter limit, are analyzed. The coupling of bending and torsion due to large blade bending are assumed to have some effects of the

flutter limits of wind turbines [3]. In the present work, the aeroelastic blade model suggested by Kallesøe [4] is used to investigate the aeroelastic stability limits of the RWT blade with and without the effects of the large blade deflection. The investigation shows no significant change of the flutter limit on the rotor speed due to the blade deflection, whereas the first edge-wise bending mode becomes negatively damped due to the coupling with blade torsion which causes a change of the effective direction of blade vibration. These observations are confirmed by nonlinear aeroelastic simulations using HAWC2 [5, 6].

Second, the effect of a free-play in the pitch system is analyzed. A linear pitch bearing stiffness with a free-play are imposed on a 2D wing-section model, suggested by Kallesøe [7]. The pitch system model and the wing-section model are combined and simulated in time to determine the relative inflow speed where flutter onsets. It is found that this flutter speed decrease when a free-play is introduced.

References

[1] E. Politis and V. Riziotis. The importance of nonlinear effects identified by aerodynamic and aero-elastic simulations on the 5 mw reference wind turbine. Deliverable D2.1, Project UpWind, September 2007. (Restricted to WP members).

[2] J. Jonkman. NREL 5 MW baseline wind turbine. Technical report, NREL/NWTC, 1617 Cole Boulevard; Golden, CO 80401-3393, USA, 2005.

[3] M. H. Hansen. Aeroelastic instability problems for wind turbines. *Wind Energy*, 10:551–577, 2007.

[4] B. S. Kallesøe. Equations of motion for a rotor blade, including gravity, pitch action and rotor speed variations. *Wind Energy*, 10:209–230, 2007.

[5] T. J. Larsen, A. M. Hansen, and T. Buhl. Aeroelastic effects of large blade deflections for wind turbines. In *Proceedings of The Science of Making Torque from Wind*, pages 238–246, The Netherlands, April 2004. Delft University of Technology.

[6] T. J. Larsen, H. Aa. Madsen, A. M. Hansen, and K. Thomsen. Investigations of stability effects of an offshore wind turbine using the new aeroelastic code HAWC2. *Proceedings of the conference "Copenhagen Offshore Wind 2005"*, 2005.

[7] B. S. Kallesøe. A low-order model for analysing effects of blade fatigue load control. *Wind Energy*, 9(5):421–436, 2006.

[8] M. A. Crisfield. *Non-linear Finite Element Analysis of Solids and Structures*, volume 2. Wiley, New York, 1997.

[9] M. H. Hansen. Aeroelastic stability analysis of wind turbines using an eigenvalue approach. *Wind Energy*, 7:133–143, 2004.

[10] Hansen M. H., Gaunaa M., and Madsen H. A. A beddoes-leishman type dynamic stall model in state-space and indicial formulation. Technical Report Risø-R-1354(EN), Risø National Laboratory, (available from www.risoe.dk), August 2004.
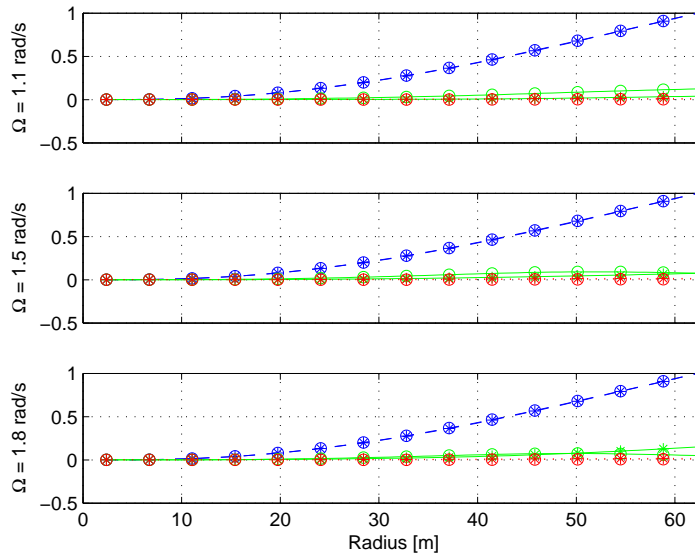
Figure 92. Amplitude of flapwise (green), edgewise (blue) and torsional (red) components of the first edgewise bending mode at different rotor speeds. Top, middle and bottom figures show the results for the rotor speeds 1.1, 1.5 and 1.8 rad/s, respectively. The circles (○) denote the components for the undeformed blade, and the crosses (×) denote the components for the deformed blade.
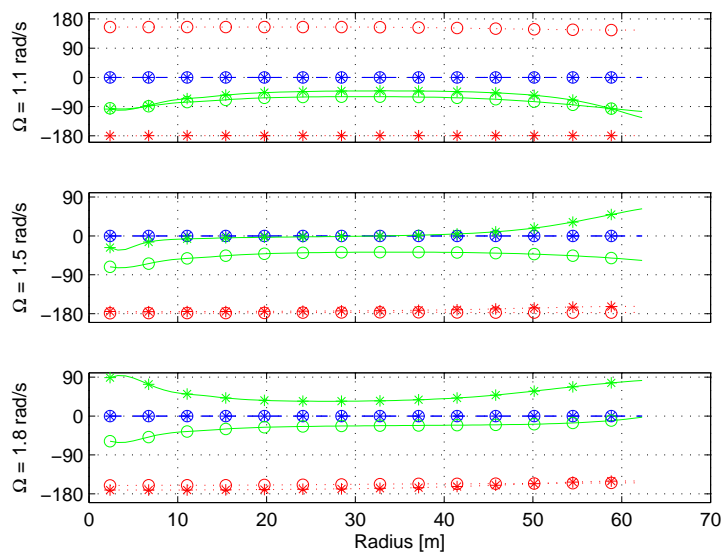

Figure 93. Phases between flapwise (green), edgewise (blue) and torsional (red) components of the first edgewise bending mode at different rotor speeds. Top, middle and bottom figures show the results for the rotor speeds 1.1, 1.5 and 1.8 rad/s, respectively. The circles (○) denote the components for the undeformed blade, and the crosses (×) denote the components for the deformed blade.
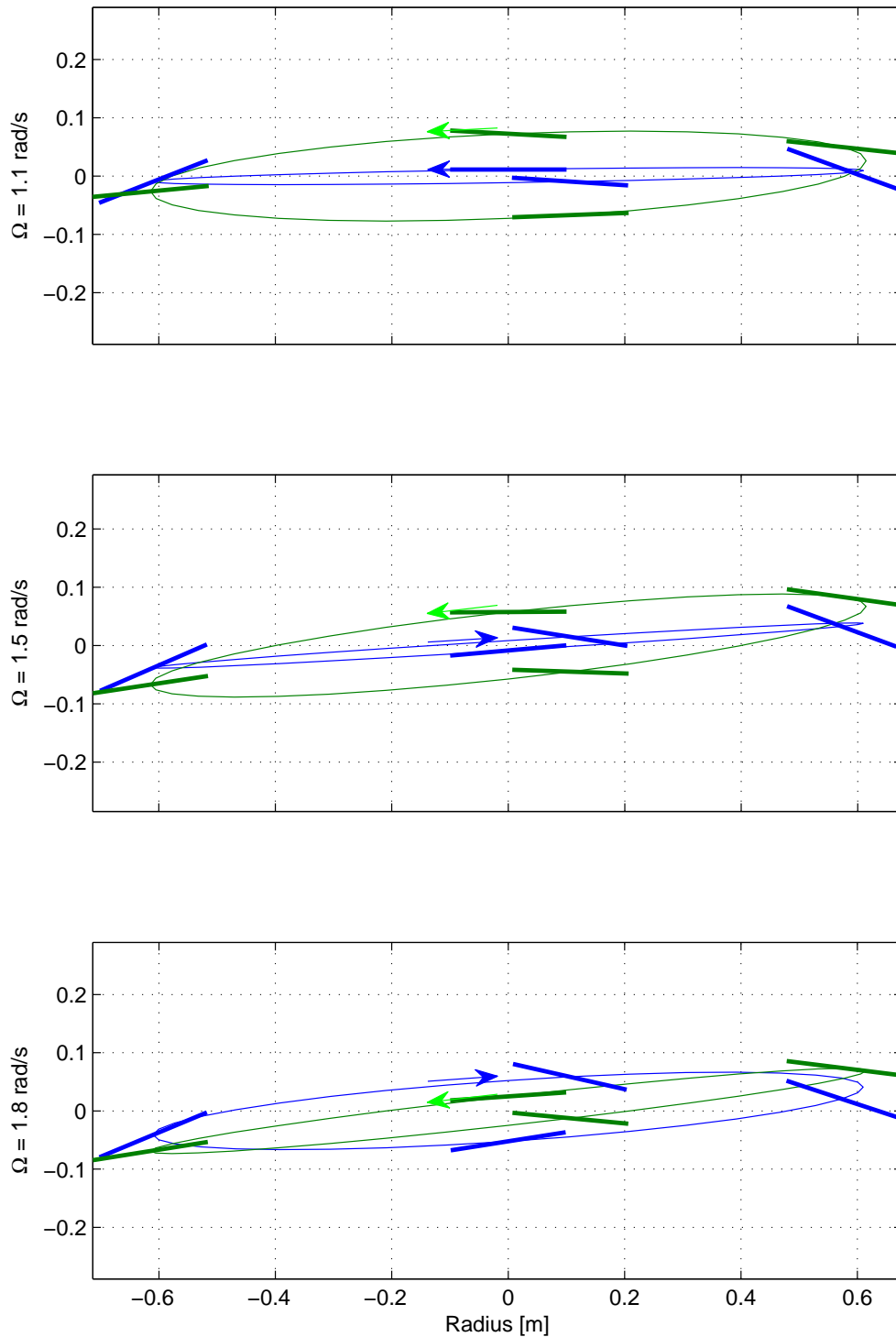
Figure 94. Traces of cross-sectional blade motion at 75 % radius in the first edgewise bending mode at different rotor speeds for the undeformed (green traces) and deformed (blue traces) blade with exaggeration of the torsional component with a factor of 1000. Arrows denote the direction of motion. Top, middle and bottom figures show the results for the rotor speeds 1.1, 1.5 and 1.8 rad/s, respectively. Note that the relative wind becomes from right to left in the displayed cross-sectional coordinate system.
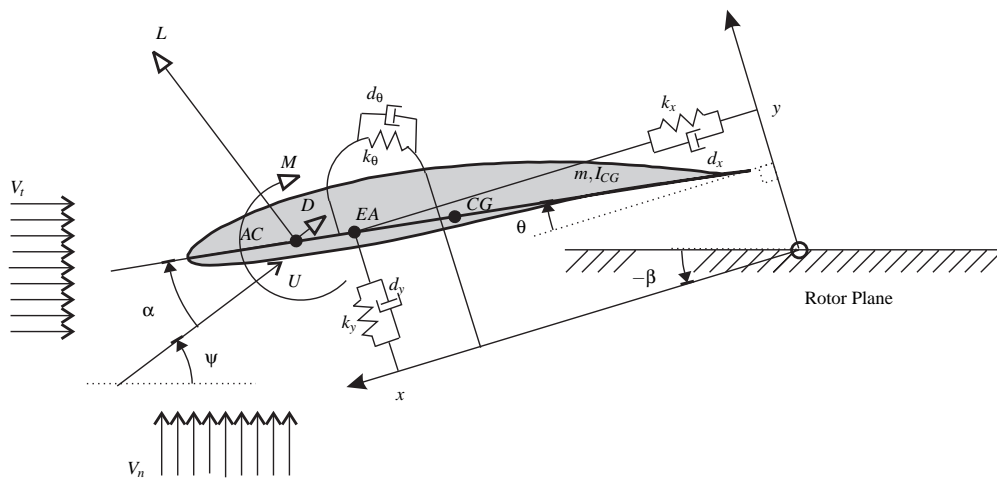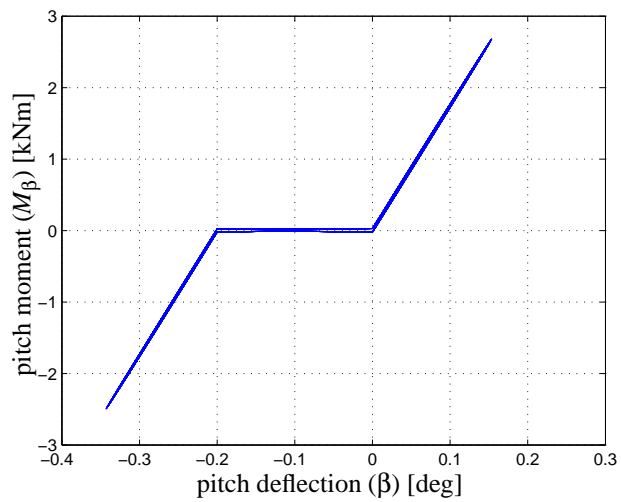
Figure 95. The wing-section model, suggested by [7].

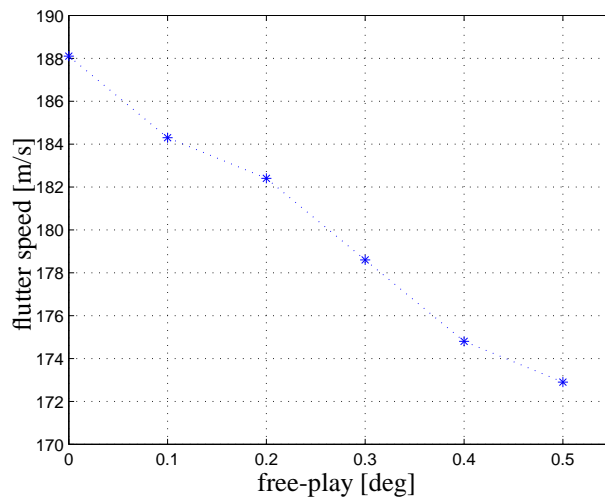*Figure 96. Pitch moment versus pitch motion for a case with a free-play on 0.2 deg.*

Figure 97. Flutter speed versus free-play in the pitch system.

9 Complete list of publications from the project

9.1 Journal papers

- Ivanell, S., Sørensen, J.N., Mikkelsen, R. and Henningson, D. (2008) "Analysis of Numerically Generated Wake Structures", to appear in Wind Energy.

- Shen, W.Z., Hansen, M.O.L. and Sørensen, J.N. (2008) "Determination of the Angle of Attack (AOA) on Rotor Blades", to appear in Wind Energy, vol. 11, no.4.

- Okulov, V.L. and Sørensen, J.N. (2008) "Refined Betz limit for rotors with a finite number of blades", to appear in Wind Energy, vol. 11, no.4.

- Okulov, V. L. and Sørensen, J. N. (2007) "Stability of helical tip vortices in a rotor far wake". Journal of Fluid Mechanics, vol. 576, pp. 1-25.

9.2 Conference papers

- Hansen, M.H.; Kallesøe, B.S., Servo-elastic dynamics of a hydraulic actuator pitching a blade with large deflections. International conference: The science of making torque from wind, Lyngby (DK), 28-31 Aug 2007. J. Phys.: Conf. Ser. (2007) 75 , 12 p.

- Larsen, T.J.; Larsen, G.C.; Aagaard Madsen, H.; Thomsen, K., Comparison of design methods for turbines in wake. 2008 European Wind Energy Conference and Exhibition, Brussels (BE), 31 Mar - 3 Apr 2008.

- Thomsen, K.; Aagaard Madsen, H.; Larsen, G.C.; Larsen, T.J., Comparison of methods for load simulation for wind turbines operating in wake. International conference: The science of making torgue from wind, Lyngby (DK), 28-31 Aug 2007. J. Phys.: Conf. Ser. (2007) 75 , 12 p.

- Aagaard Madsen, H., A verification study of the BEM model and a proposal for two modifications. IEA Annex XI/XX meeting, Risø (DK), 14-15 Jun 2007. Unpublished.

- Aagaard Madsen, H., A verification study of the BEM model and a proposal for two modifications. Seminar on wind turbine wakes - model and measurements, Visby (SE), 7-8 Jun 2007. Unpublished.

- Aagaard Madsen, H.; Mikkelsen, R.; øye, S.; Bak, C.; Johansen, J., A detailed investigation of the blade element momentum (BEM) model based on analytical and numerical results and proposal for modifications of the BEM model. International conference: The science of making torque from wind, Lyngby (DK), 28-31 Aug 2007. J. Phys.: Conf. Ser. (2007) 75 , 11 p.

- Gaunaa, M.; Johansen, J., Can winglets increase Cp? ...and if so, how much. IEA Annex XI/XX meeting, Risø (DK), 14-15 Jun 2007. Unpublished.

- Gaunaa, M.; Johansen, J., Determination of the maximum aerodynamic efficiency of wind turbine rotors with winglets. International conference: The science of making torque from wind, Lyngby (DK), 28-31 Aug 2007. J. Phys.: Conf. Ser. (2007) 75 , 12 p.

- Zahle, F.; Sørensen, N.N., Rotor aerodynamics in atmospheric shear flow. In: Scientific proceedings. 2008 European Wind Energy Conference and Exhibition, Brussels (BE), 31 Mar - 3 Apr 2008. (2008) p. 120-124

- Sørensen, N.N., CFD modeling of laminar-turbulent transition for airfoils and rotors using the gamma - Retheta model. In: Scientific proceedings. 2008 European Wind Energy Conference and Exhibition, Brussels (BE), 31 Mar - 3 Apr 2008. (2008) p. 106-112

- Zahle, F.; Sørensen, N.N., Rotor aerodynamics in atmospheric shear flow. In: Scientific proceedings. 2008 European Wind Energy Conference and Exhibition, Brussels (BE), 31 Mar - 3 Apr 2008. (2008) p. 120-124

- Bak, C.; Andersen, P.B.; Gaunaa, M., Wind turbine airfoil design considering aerodynamic and structural characteristics in 3D blade design. IEA Annex XI/XX meeting, Risø (DK), 14-15 Jun 2007. Unpublished.

- Bak, C., Sensitivity of key parameters in aerodynamic wind turbine rotor design on power and energy performance. International conference: The science of making torque from wind, Lyngby (DK), 28-31 Aug 2007. J. Phys.: Conf. Ser. (2007) 75 , 10 p.

- Ivanell, S., Sørensen, J.N., Mikkelsen, R. and Henningson, D. (2008) ″Stability analysis of the tip vorticies of a wind turbine″, AIAA conference paper, Reno.

- Shen, W.Z., Zakkam, V.A.K., Sørensen, J.N. and Appa, K. (2007) ″Analysis of counter-rotating wind turbines″. In: Sørensen, Hansen and Hansen (Eds.), Journal of Physics: Conference Series, Vol. 75, paper 012003, http://www.iop.org/EJ/journal/conf.

- Okulov, V.L. and Sørensen, J.N. (2007) ″Optimum operating regimes for the ideal wind turbine″. In: Sørensen, Hansen and Hansen (Eds.), Journal of Physics: Conference Series, Vol. 75, paper 012009, http://www.iop.org/EJ/journal/conf.

- Carcangiu, C.E., Sørensen, J.N., Cambuli, F. and Mandas, N. (2007) ″CFD-RANS analysis of the rotational effects on the boundary layer of wind turbine blades″. In: Sørensen, Hansen and Hansen (Eds.), Journal of Physics: Conference Series, Vol. 75, paper 012031, http://www.iop.org/EJ/journal/conf.

- Martinez, G.G., Sørensen, J.N. and Shen, W.Z. (2007) ″3D boundary layer study on a rotating wind turbine blade″. In: Sørensen, Hansen and Hansen (Eds.), Journal of Physics: Conference Series, Vol. 75, paper 012032, http://www.iop.org/EJ/journal/conf.

- Walther, J.H., Guenot, M., Machefaux, E., Rasmussen, J.T., Chatelain, P., Okulov, V.L., Sørensen, J.N., Bergdorf, M. and Koumoutsakos, P. (2007) ″A numerical study on the stability of helical vortices using vortex methods″. In: Sørensen, Hansen and Hansen (Eds.), Journal of Physics: Conference Series, Vol. 75, paper 012034, http://www.iop.org/EJ/journal/conf.

- Ivanell, S., Sørensen, J.N., Mikkelsen, R. and Henningson, D. (2007) ″Numerical analysis of the tip and root vortex position in the wake of a wind turbine″. In: Sørensen, Hansen and Hansen (Eds.), Journal of Physics: Conference Series, Vol. 75, paper 012035, http://www.iop.org/EJ/journal/conf.

- Mikkelsen, R., Sørensen, J.N., øye, S. and Troldborg, N. (2007) ″Analysis of power enhancement for a row of wind turbines using the actuator line technique″. In: Sørensen, Hansen and Hansen (Eds.), Journal of Physics: Conference Series, Vol. 75, paper 012044, http://www.iop.org/EJ/journal/conf.

- Leloudas, G., Zhu, W.J., Sørensen, J.N., Shen, W.Z. and Hjort, S. (2007) ″Prediction and reduction of noise from a 2.3 MW wind turbine″. In: Sørensen, Hansen and Hansen (Eds.), Journal of Physics: Conference Series, Vol. 75, paper 012083, http://www.iop.org/EJ/journal/conf.

- Mikkelsen, R.; Sørensen, J.N.; Troldborg, N. ″Prescribed wind shear modelling with the actuator line technique″,Presented at EWEC, European Wind Energy Conf.. Milan, Italy, 2007.

9.3 Reports

- Døssing, M., High frequency microphone measurements for transition detection on airfoils. NACA-0015 appendix report. Risø-R-1645(App. 1)(EN) (2008) 140 p.

- Døssing, M., High frequency microphone measurements for transition detection on airfoils. Risø C2-18 appendix report. Risø-R-1645(App. 2)(EN) (2008) 178 p.

- Døssing, M., High frequency microphone measurements for transition detection on air-foils. Risø B1-18 appendix report. Risø-R-1645(App. 1)(EN) (2008) 166 p.

- Døssing, M., High frequency microphone measurements for transition detection on air-foils. Risø-R-1645(EN) (2008) 24 p.

9.4 Oral presentations

- Døssing, M., Profiler i LM's vindtunnel: Bestemmelse af transitionspunkt vha. mikro-foner. Temamøde om aeroelasticitet - seneste resultater, Risø (DK), 14 May 2008. Unpublished.

- Kallesøe, B.S.; Hansen, M.H., Forskellige ikke-lineære effekter der influerer fluttergrænsen. Temamøde om aeroelasticitet - seneste resultater, Risø (DK), 14 May 2008. Unpublished.

- Larsen, T.J.; Aagaard Madsen, H.; Larsen, G.C., Sammenligning af designmetoder for møller i wake. Temamøde om aeroelasticitet - seneste resultater, Risø (DK), 14 May 2008. Unpublished.

- Aagaard Madsen, H., Videreudvikling af dynamisk wake-meandering (DWM) model. Temamøde om aeroelasticitet - seneste resultater, Risø (DK), 14 May 2008.

- Bak, C.; Aagaard Madsen, H.; Gaunaa, M.; Andersen, P.B.; Døssing, M.; Rasmussen, M.; Hansen, P.; Møller, R.; Fuglsang, P., Vindtunnelforsøg med højfrekvente trykmålinger. Vinddag 2007, Dansk Forskningskonsortium for Vindenergi, Risø (DK), 27 Nov 2007. Unpublished.

- Aagaard Madsen, H., Inflow målinger med pitorør på Siemens 3,6 MW vindmølle. Vinddag 2007, Dansk Forskningskonsortium for Vindenergi, Risø (DK), 27 Nov 2007. Unpublished.

- Sørensen, N.N., Modellering af laminær/turbulent transition. Temamøde om aeroelasticitet - seneste resultater, Risø (DK), 14 May 2008. Unpublished.

- Zahle, F., Flowinteraktion imellem rotor, tårn og nacelle med 3D CFD. Temamøde om aeroelasticitet - seneste resultater, Risø (DK), 14 May 2008. Unpublished.

- Bak, C., Nyt profil i LM's vindtunnel: Høj effektivitet og ruhedsufølsomhed. Temamøde om aeroelasticitet - seneste resultater, Risø (DK), 14 May 2008. Unpublished.

- Aagaard Madsen, H. ,Eksperimentel rotor aerodynamik - Tjæreborg eksperimentet. Temamøde om aeroelasticitet - seneste resultater, Risø (DK), 14 May 2008. Unpublished.

- Sørensen, J.N., Måling og modellering af støj. Temamøde om aeroelasticitet - seneste resultater, Risø (DK), 14 May 2008. Unpublished.

- Sørensen, J.N., Kortlgning af 3-D effekter på roterende vinge. Temamøde om aeroelasticitet - seneste resultater, Risø (DK), 14 May 2008. Unpublished.

- Mikkelsen, R., CFD-modellering af aerodynamisk induktion for en Betz-optimal rotor. Temamøde om aeroelasticitet - seneste resultater, Risø (DK), 14 May 2008. Unpublished.

- Troldborg, N., Simulering og karakterisering af kølvandsturbulens. Temamøde om aeroelasticitet - seneste resultater, Risø (DK), 14 May 2008. Unpublished.

9.5 Lectures

- Sørensen, J.N.; Mikkelsen, R.; Troldborg, N. and Okulov, V.L. (2007) "Modelling of wind turbine wakes: A state of the art", Von Karman Institute Lecture Series, vol. 2007-05, pp. 1-32.